SAPIENZA
UNIVERSITÀ DI ROMA

Facoltà di Ingegneria

Dottorato di Ricerca in

Elettromagnetismo

XXV Ciclo

Linear and non-linear photonic properties and applications of hyperbolic metamaterials

Thesis Advisor:

Prof. Fabrizio Frezza

Dr. Alessandro Ciattoni

Candidate:

Elisa Spinozzi

ANNO ACCADEMICO 2011-2012

Contents

1 Introduction

Achieving a desired electromagnetic functionality implies the capability of manipulating the electromagnetic radiation in a desired manner through elaborating structures and geometries with available materials. The performances of electromagnetic devises are nowadays limited by the restricted range of available media elecromamagnetic properties. Therefore, artificial materials are synthesized at molecular level in order to achieve unconventional electromagnetic features not displayed by standard media.

Artificially structured composites of well-arranged functional inclusions substantially smaller, or at least smaller, than the radiation wavelength are called *metamaterials*. They can display novel and unusual electromagnetic properties that can be theoretically described through the general approach of *effective medium theory*. Specifically, although the size of the inclusions is usually several orders of magnitude greater than the atomic or molecular ones, the composite inhomogeneity scale is still much smaller than the radiation wavelength and their electromagnetic responses can be expressed in terms of *homogenized effective* material parameters [1].

The word *metamaterial* first appeared in literature in 2000 when Smith et al. published their seminal paper on a structured material with simultaneously negative permeability and permittivity at microwave frequencies. They demonstrate that a composite medium exhibits a frequency region in the microwave range with simultaneously negative values of effective permeability $\mu_{eff}(\omega)$ and permittivity $\varepsilon_{eff}(\omega)$. What makes the resulting media special is that the *effective* material parameters

can have values not observed in ordinary materials [2]. Such a medium is called a *negative refractive index medium* or a *left-handed medium*. The first paper on left handed materials dates back to 1960s when Veselago theoretically studied the monochromatic electromagnetic plane wave propagation in a lossless medium with simultaneously negative real permittivity and permeability at a given frequency, and he theoretically showed that in such media the direction of the Poynting vector is antiparallel to the direction of phase velocity, i.e. the vectors $\boldsymbol{E}$, $\boldsymbol{H}$ and the wave vector $\boldsymbol{k}$ form a left-handed triplet [3]. The recent regained interest in this medium occurred after the first experimental demonstration of a Veselago medium by Smith et al. [2, 4]. Inspired by the Pendry's idea about the perfect lens [5], which represents the initial attempt to fill the gap between novel metamaterials and exciting applications, they manufactured such a composite medium operating in the microwave range.

The early works dealing with metamaterials were focused on achieving a negative refractive index and therefore metamaterial has become almost synonymous with left-handed media. Today's metamaterial research has expanded far beyond the interest on negative refraction. Various artificially engineered composites have been devised and manufactured with genuinely novel electromagnetic properties which can not be observed in available materials. Metamaterial structural units can be tailored in shape and size, composition and morphology, thus providing the means for designing a structure with the desired electromagnetic features.

2

Effective medium and homogenization techniques

2.1 Homogeneous response

Maxwell's equations are the basic tool for describing electromagnetic and optical phenomena. The propagation of electromagnetic radiation in any medium is fully described by the macroscopic Maxwell's equations

$$\boldsymbol{\nabla} \cdot \boldsymbol{D} = \rho\,, \qquad \boldsymbol{\nabla} \cdot \boldsymbol{B} = 0\,, \tag{2.1}$$

$$\boldsymbol{\nabla} \times \boldsymbol{E} = -\frac{\partial \boldsymbol{B}}{\partial t}\,, \qquad \boldsymbol{\nabla} \times \boldsymbol{H} = \boldsymbol{j} + \frac{\partial \boldsymbol{D}}{\partial t}\,, \tag{2.2}$$

where the electric charge density ρ and the electric current density $\boldsymbol{j}$ are the sources of electromagnetic radiation, $\boldsymbol{E}$ and $\boldsymbol{H}$ are the macroscopic *electric vector* and the *magnetic vector*, and to include the effect of field-matter interaction, it is necessary to introduce the *electric displacement* $\boldsymbol{D}$ and the *magnetic induction* $\boldsymbol{B}$. The microscopic local fields and their fast variations over small length scale are averaged over a sufficiently large volume to yield the macroscopic field quantities and shows a macroscopic homogeneous response to the applied field. Predicting the field dynamics due to a given distribution of current and charges implies supplementing these equations by the suitable relations describing the effect of the electromagnetic field on material media. These relation are known as constitutive equation and are given by

$$\boldsymbol{D} = \varepsilon_0 \boldsymbol{E} + \boldsymbol{P}\,, \qquad \boldsymbol{B} = \mu_0 \left(\boldsymbol{H} + \boldsymbol{M}\right)\,, \tag{2.3}$$

where $\boldsymbol{P}$ is the *electric polarization* and $\boldsymbol{M}$ is the *magnetic polarization*. The effects, $\boldsymbol{P}$ and $\boldsymbol{M}$, are related to their causes through the *susceptibility function* χ. Considering anisotropic media with spatial and temporal non-local behaviors and non-linear response as well, we can write

$$P_i(\boldsymbol{r},t) = \varepsilon_0 \int d^3\boldsymbol{r}' \int_{-\infty}^{t} dt' \chi_{ij}^{(1)e}(\boldsymbol{r},\boldsymbol{r}',t-t') E_j(\boldsymbol{r}',t') + \\ + \varepsilon_0 \int d^3\boldsymbol{r}' \int_{-\infty}^{t} dt' \int_{-\infty}^{t} dt'' \chi_{ijk}^{(2)e}(\boldsymbol{r},\boldsymbol{r}',t-t',t-t'') E_j(\boldsymbol{r}',t') E_k(\boldsymbol{r}',t'') + \dots$$

$$M_i(\boldsymbol{r},t) = \mu_0 \int d^3\boldsymbol{r}' \int_{-\infty}^{t} dt' \chi_{ij}^{(1)m}(\boldsymbol{r},\boldsymbol{r}',t-t') H_j(\boldsymbol{r}',t') + \\ + \mu_0 \int d^3\boldsymbol{r}' \int_{-\infty}^{t} dt' \int_{-\infty}^{t} dt'' \chi_{ijk}^{(2)m}(\boldsymbol{r},\boldsymbol{r}',t-t',t-t'') H_j(\boldsymbol{r}',t') H_k(\boldsymbol{r}',t'') + \dots$$

For a linear spatially-local response, these equations reduce to

$$P_i^L(\boldsymbol{r},t) = \varepsilon_0 \int_{-\infty}^{t} dt' \chi_{ij}^{(1)e}(t-t') E_j(\boldsymbol{r},t') \,, \\ M_i^L(\boldsymbol{r},t) = \mu_0 \int_{-\infty}^{t} dt' \chi_{ij}^{(1)m}(t-t') H_j(\boldsymbol{r},t') \,,$$

which in the frequency domain becomes [1]

$$\left[P_i^L(\boldsymbol{r})\right]^\omega = \varepsilon_0 \chi_{ij}^e(\omega) E_j^\omega(\boldsymbol{r}) \,, \qquad \left[M_i^L(\boldsymbol{r})\right]^\omega = \mu_0 \chi_{ij}^m(\omega) H_j^\omega(\boldsymbol{r}) \,, \tag{2.4}$$

The macroscopic linear dielectric and magnetic medium response can be described by the the dielectric permittivity tensor $\bar{\bar{\varepsilon}}_r(\omega)$ and magnetic permeability tensor

[1]
$$\left[P_i^L(\boldsymbol{r})\right]^\omega = \int_{-\infty}^{+\infty} dt P_i^L(\boldsymbol{r},t) e^{-i\omega t} = \int_{-\infty}^{+\infty} dt e^{-i\omega t} \int_{-\infty}^{t} dt' \varepsilon_0 \chi_{ij}(t-t') E_j(\boldsymbol{r},t')$$
and, letting the matrix elements of susceptibility tensor $\chi(t-t')$ to vanish for $t' > t$, the second integral can be extended to $+\infty$
$$\left[P_i^L(\boldsymbol{r})\right]^\omega = \int_{-\infty}^{+\infty} dt e^{-i\omega t} \int_{-\infty}^{+\infty} dt' \varepsilon_0 \chi_{ij}(t-t') E_j(\boldsymbol{r},t') = \\ = \varepsilon_0 \int_{-\infty}^{+\infty} dt' e^{-i\omega t'} \left[\int_{-\infty}^{+\infty} dt e^{-i\omega(t-t')} \chi_{ij}(t-t')\right] E_j(\boldsymbol{r},t') = \\ = \varepsilon_0 \chi_{ij}(\omega) \int_{-\infty}^{+\infty} dt' e^{-i\omega t'} E_j(\boldsymbol{r},t') = \varepsilon_0 \chi_{ij}(\omega) E_j^\omega(\boldsymbol{r}) \,,$$
$\left[P_i^L(\boldsymbol{r})\right]^\omega = \varepsilon_0 \chi_{ij}^e(\omega) E_j^\omega(\boldsymbol{r})$, where $E_j^\omega(\boldsymbol{r})$ is the j-th components of complex amplitude of monochromatic plane wave at angular frequency ω.

$\bar{\bar{\mu}}_r(\omega)$, so that

$$\begin{aligned} \left[D_i^L(\boldsymbol{r})\right]^\omega &= \varepsilon_0[\varepsilon_r(\omega)]_{ij}E_j^\omega(\boldsymbol{r})\,, \qquad \Rightarrow \quad [\varepsilon_r(\omega)]_{ij} = \mathbb{1} + [\chi^{(1)e}(\omega)]_{ij}\,. \\ \left[B_i^L(\boldsymbol{r})\right]^\omega &= \mu_0[\mu_r(\omega)]_{ij}H_j^\omega(\boldsymbol{r})\,, \qquad \Rightarrow \quad [\mu_r(\omega)]_{ij} = \mathbb{1} + [\chi^{(1)m}(\omega)]_{ij}\,. \end{aligned} \tag{2.5}$$

2.2 Homogenization techniques

Macroscopic Maxwell equations (2.2) are obtained by averaging the rapidly fluctuating electromagnetic fields at atomic or molecular scales over volumes that contain a large enough number of polarizable or magnetizable atoms/molecules. Within this framework, susceptibilities for bulk materials can be defined. In the case of metamaterials, the structural units of the composites are assumed to be sufficiently larger than the molecular scale and yet much smaller than the radiation wavelength so that they can effectively be described by means of bulk dielectric permittivity and magnetic permeability.

According to shape, size and geometry of the inhomogeneities embedded in the host background, specific and different homogenization theories are available for predicting effective macroscopic permittivity and permeability of the medium. Three main kinds of structured composites are: layered media [6, 7, 8, 9, 10, 11, 12], nanowire [8, 12, 13, 14] and nanosphere composite [1, 15, 16, 17]. In particular, we are mainly concerned here on structures exhibiting exotic properties at optical frequencies, i.e. optical metamaterials not displaying magnetic properties, so that the homogenization theory is here used to obtain the effective dielectric response. This kind of metamaterial can provide truly unique optical properties that can be useful for a number of advanced applications and devices. The optical properties of these structures can be strikingly different than those of natural materials. A number of applications of such unusual materials are discussed in next chapter.

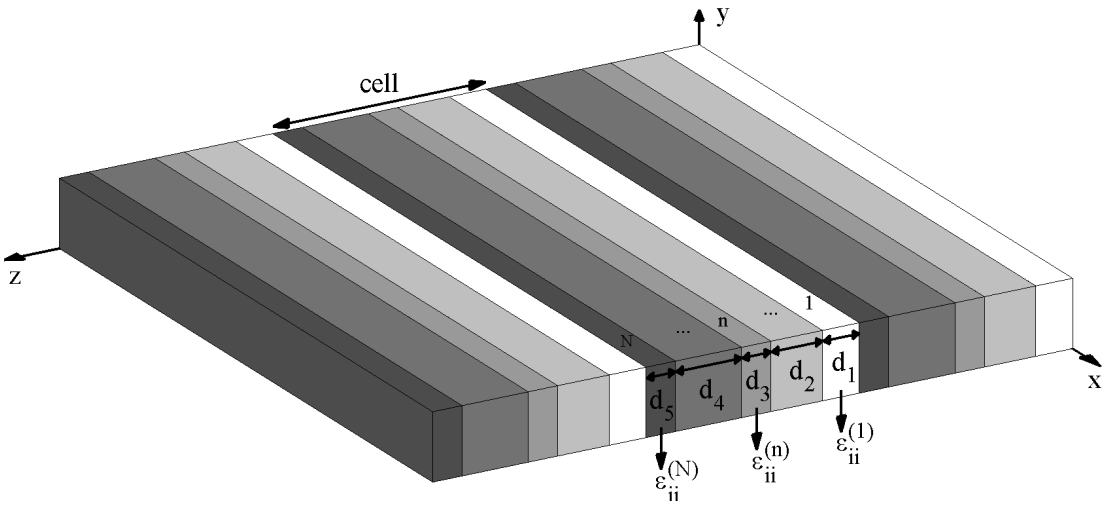

Figure 2.1: Layered media of alternating cells (in this particular case there are 3 cells) each consisting of $N = 5$ layers; d_1, d_n and d_N are the thickness of the first, the n-th (in this case the third) and the N-th (the fifth) layer and, supposing to orient each layer's optical principal axes in the same direction of the reference frame, $\varepsilon_{ii}^{(1)}$, $\varepsilon_{ii}^{(n)}$ and $\varepsilon_{ii}^{(N)}$ are the corresponding values of dielectric permittivity tensor diagonal elements.

2.2.1 Layered media

An example of homogenizable medium is a periodically stratified medium, i.e. a structure consisting of alternating layers of two or more media in the limit that the thicknesses of each layer are much smaller than the wavelength of electromagnetic wave in the effective medium. A stratified medium is a composite whose properties are constant through each plane perpendicular to a fixed direction.

Considering a one-dimensional system of alternating cells (***Fig.2.1***) each consisting of N layers along z axis and let d_n the thicknesses of the n-th leyer, $\varepsilon_{ij}^{(n)}$ the corresponding dielectric permittivity tensor and $\boldsymbol{V}^{(n)}$ the physical macroscopic electromagnetic field vectors ($\boldsymbol{V} = \boldsymbol{E}, \boldsymbol{D}, \boldsymbol{B}, \boldsymbol{H}$). If the field vacuum wavelength is much greater than the spatial period ($\lambda >> d$, d is the cell thickness $d = \sum_{n=1}^{N} d_n$), the considered periodically stratified medium can be homogenized, i.e. its electromagnetic response can be shown to coincide with that of a suitable homogeneous

medium. In order to obtain the overall effective response, note that any component of the local electromagnetic field can be assumed, within each layer, independent on the longitudinal z-coordinate since the layers are extremely small. Although this is a very reasonable physical assumption, it can be rigorously proved exploiting the well known powerful two-scale expansion method [18]. Each of the physical observable (macroscopic) electromagnetic field vectors, say $\boldsymbol{V}$, is obtained by averaging (along the z axis) the layer local fields over the period d, so that

$$\boldsymbol{V} = \left\langle \boldsymbol{V}^{(n)} \right\rangle = \sum_{n=1}^{N} f_n \boldsymbol{V}^{(n)} , \tag{2.6}$$

where $f_n = d_n/d$ is the volume filling fraction of the n-th layer [9]. Within each unit cell (of thickness d), at each plane interface between the n-th and $(n+1)$-th layer, the local fields have to satisfy the electromagnetic boundary conditions (continuity of the tangential component of electric and magnetic fields and continuity of the normal components of the displacement and magnetic induction fields) so the local fields are connected by the relations

$$\begin{aligned} E_x^{(n)} &= E_x^{(n+1)} , & H_x^{(n)} &= H_x^{(n+1)} , \\ E_y^{(n)} &= E_y^{(n+1)} , & H_y^{(n)} &= H_y^{(n+1)} , \\ D_z^{(n)} &= D_z^{(n+1)} , & B_z^{(n)} &= B_z^{(n+1)} . \end{aligned}$$

The linear constitutive relations (2.5) link $\boldsymbol{E}$ and $\boldsymbol{H}$ to the corresponding $\boldsymbol{D}$ and $\boldsymbol{B}$ thorugh the tensors ε_{ij} and μ_{ij} (the subscript r is neglected). From the principle of energy conservation it can be proved that the dielectric permittivity tensor of a non-absorbing crystal is Hermitian and has only six independent elements [19]. Therefore it is always possible chose a coordinate system in which the tensor is diagonal, known as *optical principal coordinate system*. Let's suppose to orient each layer's optical principal axes in the same direction of the reference frame (***Fig.2.1***). Averaging[2] the local fields $D_x^{(n)}$, $D_y^{(n)}$, $E_z^{(n)}$, $B_x^{(n)}$, $B_y^{(n)}$, $H_z^{(n)}$ the effective relative

[2]Considering $D_x^{(n)}$ the x component of electric displacement. The corresponding component of

dielectric permittivity and relative magnetic permeability tensors can be obtained

$$\varepsilon^{(eff)} = \mathrm{diag}\left[\left\langle\varepsilon_x^{(n)}\right\rangle, \left\langle\varepsilon_y^{(n)}\right\rangle, \left\langle\varepsilon_z^{(n)}\right\rangle^{-1}\right], \quad \mu^{(eff)} = \mathrm{diag}\left[\left\langle\mu_x^{(n)}\right\rangle, \left\langle\mu_y^{(n)}\right\rangle, \left\langle\mu_z^{(n)}\right\rangle^{-1}\right],$$

$$\left\langle\varepsilon_x^{(n)}\right\rangle = \sum_{n=1}^{N} f_n \varepsilon_x^{(n)}, \quad \left\langle\varepsilon_y^{(n)}\right\rangle = \sum_{n=1}^{N} f_n \varepsilon_y^{(n)}, \quad \left\langle\varepsilon_z^{(n)}\right\rangle^{-1} = \frac{1}{\sum_{n=1}^{N} \frac{f_n}{\varepsilon_z^{(n)}}}, \tag{2.7}$$

$$\left\langle\mu_x^{(n)}\right\rangle = \sum_{n=1}^{N} f_n \mu_x^{(n)}, \quad \left\langle\mu_y^{(n)}\right\rangle = \sum_{n=1}^{N} f_n \mu_y^{(n)}, \quad \left\langle\mu_z^{(n)}\right\rangle^{-1} = \frac{1}{\sum_{n=1}^{N} \frac{f_n}{\mu_z^{(n)}}}. \tag{2.8}$$

Effective layered medium theory as limit of characteristic matrix method

A coordinate system frequently used to specify the relative orientation between the electromagnetic wave and a planar structure is erected using the *plane of incidence* and its normal direction. Such plane contains the propagation direction and the vector perpendicular to the plane surface separating two media. The component of the electric field belonging to this plane is termed *p-like* (parallel) and the component perpendicular to this plane is termed *s-like* (from *senkrecht*, German for perpendicular). Radiation with an s-like electric field is referred to as *transverse-electric* (TE) wave whilst radiation with a p-like electric field is said to be a *transverse-magnetic* (TM) wave

$$\text{TE}: \quad \begin{cases} \boldsymbol{E}(x,z) = E_y(x,z)\boldsymbol{e}_y \\ \boldsymbol{H}(x,z) = H_x(x,z)\boldsymbol{e}_x + H_z(x,z)\boldsymbol{e}_z \end{cases}$$

---

the macroscopic field $\boldsymbol{D}$ is the average over all n layers $D_x = \left\langle D_x^{(n)}\right\rangle$

$$D_x = \sum_{n=1}^{N} f_n D_x^{(n)} = \varepsilon_0 \sum_{n=1}^{N} f_n \varepsilon_x^{(n)} E_x^{(n)} = \varepsilon_0 \left[\sum_{n=1}^{N} f_n \varepsilon_x^{(n)}\right] E_x = \varepsilon_0 \left\langle\varepsilon_x^{(n)}\right\rangle E_x = \varepsilon_0 \varepsilon_x^{(eff)} E_x,$$

where we use the relation $D_x = \varepsilon_0 \varepsilon_x E_x$ and the continuity of the electric field x component ($E_x^{(n)} = E_x$ over each n-th layer). In the same way, considering E_z and its averaged value

$$E_z = \sum_{n=1}^{N} f_n E_z^{(n)} = \frac{1}{\varepsilon_0} \sum_{n=1}^{N} f_n \frac{D_z^{(n)}}{\varepsilon_z^{(n)}} = \frac{1}{\varepsilon_0} \left[\sum_{n=1}^{N} \frac{f_n}{\varepsilon_z^{(n)}}\right] D_z = \frac{1}{\varepsilon_0} \frac{D_z}{\left\langle\varepsilon_z^{(n)}\right\rangle^{-1}} = \frac{1}{\varepsilon_0} \frac{D_z}{\varepsilon_z^{(eff)}}.$$

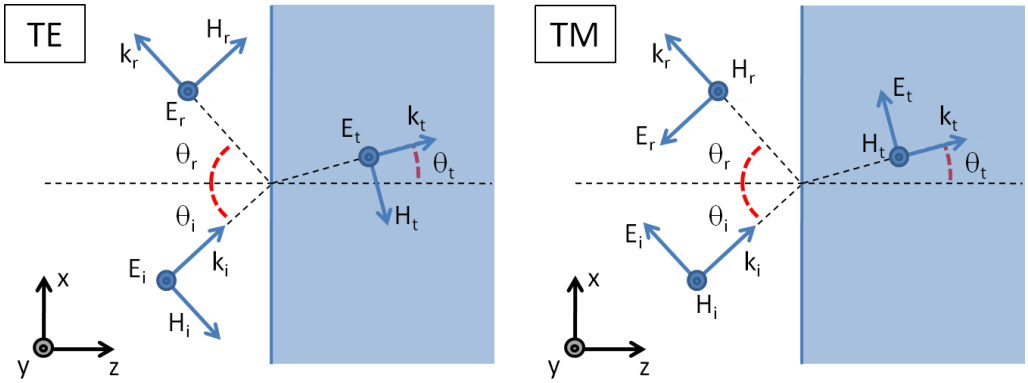

Figure 2.2: Schematic illustration of plane of incidence of Transverse electric (TE, s-polarization) and transverse magnetic (TM, p-polarization) wave.

$$\text{TM}: \quad \begin{cases} \boldsymbol{E}(x,z) = E_x(x,z)\boldsymbol{e}_x + E_z(x,z)\boldsymbol{e}_z \\ \boldsymbol{H}(x,z) = H_y(x,z)\boldsymbol{e}_y \end{cases}$$

where we have assumed the plane of incidence to coincide with the xz-plane (see ***Fig.2.2***).

The effective medium parameters of alternating layers can be calculated from the characteristic matrix method in the limit of very small layers' thickness.

For TM wave in a homogeneous anisotropic medium with dielectric permittivity tensor $\varepsilon = \text{diag}[\varepsilon_x, \varepsilon_y, \varepsilon_z]$, Maxwell's equations reduce to the following three scalar equations (time dependence $e^{-i\omega t}$ being assumed)

$$\begin{cases} \dfrac{\partial E_x}{\partial z} - \dfrac{\partial E_z}{\partial x} = i\omega\mu_0 H_y \\ \dfrac{\partial H_y}{\partial z} = i\omega\varepsilon_0\varepsilon_x E_x \\ \dfrac{\partial H_y}{\partial x} = -i\omega\varepsilon_0\varepsilon_z E_z \end{cases} \tag{2.9}$$

Defining quantities

$$\begin{cases} E_x(x,z) = e^{ik_0 x \sin\vartheta} E_x(z) \\ H_y(x,z) = e^{ik_0 x \sin\vartheta} H_y(z) \\ E_z(x,z) = e^{ik_0 x \sin\vartheta} E_z(z) \end{cases}$$

the equations (2.9) becomes

$$\begin{cases} \dfrac{dE_x}{dz} = i[\omega\mu_0 H_y + k_0 \sin\vartheta E_z] \\ \dfrac{dH_y}{dz} = i\omega\varepsilon_0\varepsilon_x E_x \\ E_z = -\dfrac{k_0 \sin\vartheta}{\omega\varepsilon_0\varepsilon_z} H_y \end{cases} \tag{2.10}$$

Substituting the third equation of (2.10) into the first

$$\frac{dE_x}{dz} = i\left[\omega\mu_0 - \frac{k_0^2 \sin^2\vartheta}{\omega\varepsilon_0\varepsilon_z}\right] H_y \tag{2.11}$$

and differentiating both members

$$\frac{d^2E_x}{dz^2} = i\left[\omega\mu_0 - \frac{k_0^2 \sin^2\vartheta}{\omega\varepsilon_0\varepsilon_z}\right] \frac{dH_y}{dz}\,;$$

using the second equation of (2.10) we get

$$\frac{d^2E_x}{dz^2} = -k_0^2\varepsilon_x\left[1 - \frac{\sin^2\vartheta}{\varepsilon_z}\right] E_x\,,$$

whose solution is

$$E_x(z) = A\cos(k_z z) + iB\sin(k_z z)\,, \tag{2.12}$$

where A and B are constants to determine by the initial conditions, and $k_z = k_0\sqrt{\varepsilon_x(1 - \sin^2\vartheta/\varepsilon_z)}$. Differentiating (2.12) and exploiting (2.11), we can write

$$H_y(z) = \frac{\omega\varepsilon_0\varepsilon_x}{k_z}\left[iA\sin(k_z z) + B\cos(k_z z)\right]\,.$$

The constants A and B are related to the initial conditions: $A = E_x(0)$ and $B = [k_z/(\omega\varepsilon_0\varepsilon_x)]H_y(0)$, therefore we can express the quantities $E_x(z)$ and $H_y(z)$ (the fields on the plane z) in terms of $E_x(0)$ and $H_y(0)$ (the fields on the plane $z = 0$)

$$\begin{cases} E_x(z) = E_x(0)\cos(k_z z) + i\dfrac{k_z}{\omega\varepsilon_0\varepsilon_x} H_y(0)\sin(k_z z) \\ H_y(z) = i\dfrac{\omega\varepsilon_0\varepsilon_x}{k_z} E_x(0)\sin(k_z z) + H_y(0)\cos(k_z z) \end{cases}$$

$$\begin{pmatrix} E_x(z) \\ H_y(z) \end{pmatrix} = \begin{pmatrix} \cos(k_z z) & i\sqrt{\dfrac{\mu_0}{\varepsilon_0}}\dfrac{k_z}{k_0\varepsilon_x}\sin(k_z z) \\ i\sqrt{\dfrac{\varepsilon_0}{\mu_0}}\dfrac{k_0\varepsilon_x}{k_z}\sin(k_z z) & \cos(k_z z) \end{pmatrix} \begin{pmatrix} E_x(0) \\ H_y(0) \end{pmatrix}\,. \tag{2.13}$$

In a stratified medium, the characteristic matrix $M^{(n)}(d_n)$ of n-th layer with thickness d_n relates the Fourier component of the field on the plane $z = z_0$ to the one on the plane $z = z_0 + d_n$ (all within n-th layer) $\boldsymbol{Q}(z_0) = M(z_0 + d)\boldsymbol{Q}(z_0 + d)$ [20, 21], therefore from (2.13) it takes the form

$$M^{(n)}(d_n) = \begin{pmatrix} \cos(k_z^{(n)} d_n) & i\sqrt{\dfrac{\mu_0}{\varepsilon_0}} \dfrac{k_z^{(n)}}{k_0 \varepsilon_x^{(n)}} \sin(k_z^{(n)} d_n) \\ i\sqrt{\dfrac{\varepsilon_0}{\mu_0}} \dfrac{k_0 \varepsilon_x^{(n)}}{k_z^{(n)}} \sin(k_z^{(n)} d_n) & \cos(k_z^{(n)} d_n) \end{pmatrix},$$

where $k_z^{(n)}$ is given by the dispersion relation $k_z^{(n)} = \sqrt{\varepsilon_x^{(n)} \left[k_0^2 - k_x^2 / \varepsilon_z^{(n)} \right]}$ (A.12). The matrix for a single cell of layered medium, alternating one sheet of each material, is the product of characteristic matrices for the N separate layers

$$M_{cell}(d) = M^{(1)}(d_1) M^{(2)}(d_2) M^{(3)}(d_3) \dots M^{(N)}(d_N) .$$

Considering, for simplicity, a bilayer system ($N = 2$):

$$M_{cell}(d) = \begin{pmatrix} \cos(k_z^{(1)} d_1) & \dfrac{i}{p^{(1)}} \sin(k_z^{(1)} d_1) \\ i p^{(1)} \sin(k_z^{(1)} d_1) & \cos(k_z^{(1)} d_1) \end{pmatrix} \begin{pmatrix} \cos(k_z^{(2)} d_2) & \dfrac{i}{p^{(2)}} \sin(k_z^{(2)} d_2) \\ i p^{(2)} \sin(k_z^{(2)} d_2) & \cos(k_z^{(2)} d_2) \end{pmatrix}, \quad (2.14)$$

where $p^{(n)} = \sqrt{\varepsilon_0/\mu_0}\, \varepsilon_x^{(n)} k_0 / k_z^{(n)}$ and by definition

$$M_{cell}(d) = \begin{pmatrix} \cos(k_z^{(cell)} d) & \dfrac{i}{p^{(cell)}} \sin(k_z^{(cell)} d) \\ i p^{(cell)} \sin(k_z^{(cell)} d) & \cos(k_z^{(cell)} d) \end{pmatrix}, \quad (2.15)$$

with $p^{(cell)} = \sqrt{\varepsilon_0/\mu_0}\, \varepsilon_x^{(cell)} k_0 / k_z^{(cell)}$.

In the limit of very small layers thickness the composite behaves as an homogeneous medium so that (2.14) and (2.15) can be set to coincide. Comparing the expressions of $M_{cell}(d)$ eigenvalues in both cases, we get

$$\cos(k_z^{(cell)} d) \pm \sqrt{\cos^2(k_z^{(cell)} d) - 1} = B \pm \sqrt{B^2 - 1} ,$$

where B is the linear coefficient of the characteristic equation for $M_{cell}(d)$ in the first form (as product between $M^{(1)}(d_1)$ and $M^{(2)}(d_2)$)

$$\lambda^2 - 2B\lambda + 1 = 0\,,$$
$$B = \cos(k_z^{(1)}d_1)\cos(k_z^{(2)}d_2) - \gamma_{TM}\sin(k_z^{(1)}d_1)\sin(k_z^{(2)}d_2)\,,$$
$$\gamma_{TM} = \frac{1}{2}\left(\frac{\varepsilon_x^{(1)}k_z^{(2)}}{\varepsilon_x^{(2)}k_z^{(1)}} + \frac{\varepsilon_x^{(2)}k_z^{(1)}}{\varepsilon_x^{(1)}k_z^{(2)}}\right)\,,$$

therefore

$$\cos(k_z^{(cell)}d) = \cos(k_z^{(1)}d_1)\cos(k_z^{(2)}d_2) - \gamma_{TM}\sin(k_z^{(1)}d_1)\sin(k_z^{(2)}d_2)\,. \tag{2.16}$$

The conventional effective layered medium theory can be obtained from (2.16) through the Taylor expansion up to the second order in $|k_z^{(1)}d_1| \ll 1$, $|k_z^{(2)}d_2| \ll 1$ and $|k_z^{(cell)}d| \ll 1$. Labeling the layer filling fractions with $d_1/d = f$ and $d_2/d = 1-f$, Taylor expansion yields

$$\left[k_z^{(cell)}\right]^2 = \left[k_z^{(1)}\right]^2 f\left[f + \frac{\varepsilon_x^{(2)}}{\varepsilon_x^{(1)}}(1-f)\right] + \left[k_z^{(2)}\right]^2(1-f)\left[(1-f) + \frac{\varepsilon_x^{(1)}}{\varepsilon_x^{(2)}}f\right]$$

and using dispersions

$$\left[k_z^{(1)}\right]^2 = \varepsilon_x^{(1)}k_0^2 - \left(\varepsilon_x^{(1)}/\varepsilon_z^{(1)}\right)k_x^2\,, \qquad \left[k_z^{(2)}\right]^2 = \varepsilon_x^{(2)}k_0^2 - \left(\varepsilon_x^{(2)}/\varepsilon_z^{(2)}\right)k_x^2\,,$$

we achieve the effective medium permittivity (2.7) in bilayer case [7]

$$\frac{\left[k_z^{(cell)}\right]^2}{\varepsilon_x^{(1)}f + \varepsilon_x^{(2)}(1-f)} + k_x^2\left[\frac{f}{\varepsilon_z^{(1)}} + \frac{(1-f)}{\varepsilon_z^{(2)}}\right] = k_0^2\,,$$
$$\varepsilon_x^{(eff)} = \varepsilon_x^{(1)}f + \varepsilon_x^{(2)}(1-f)\,, \qquad \varepsilon_z^{(eff)} = \frac{1}{\dfrac{f}{\varepsilon_z^{(1)}} + \dfrac{(1-f)}{\varepsilon_z^{(2)}}}\,. \tag{2.17}$$

2.2.2 Nanosphere media

Maxwell Garnett and Bruggeman effective theory

A nanosphere medium or discrete random composite is a composite in which small particles of radius $r \ll \lambda$ are randomly embedded in a host bulk medium. The

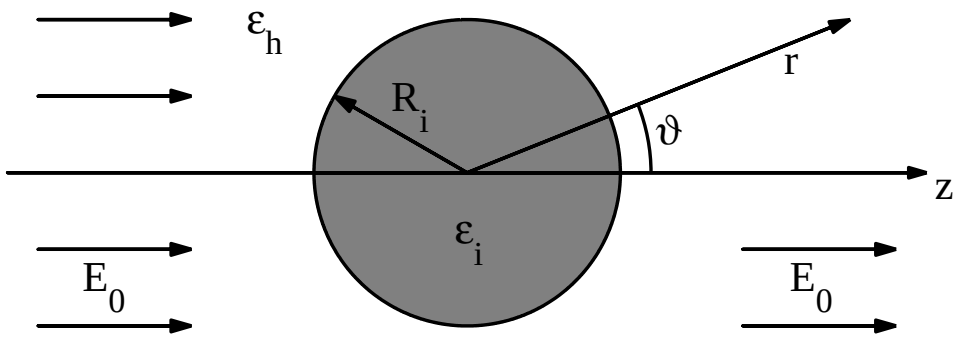

Figure 2.3: A single dielectric sphere of radius R_i with dielectric constant ε_i embedded in a host matrix with dielectric constant ε_h placed in an uniform electric field, which at large distances from the sphere, is directed along the z axis and has magnitude E_0.

most widely used effective medium approaches to homogenize the electromagnetic response of such structured composite are: the Maxwell-Garnett theory (MG) [22] and the Bruggeman effective medium theory (EMT) [23]. Each of these two methods is based upon slightly different assumptions regarding the composite topology and the material properties of each constituent in the mixture, depending on the relative concentration of the inclusions. In the first composite kind, the inclusions particles embedded in the host material are quite dilute and have well-defined smooth shapes. This is usually called the MG geometry. When the two constituent materials intermingle with each other and the two materials play symmetric roles it is difficult to say which is the host and which is the inclusion. This type of topology is commonly referred to as the Bruggeman geometry.

These models can be derived from the polarizability of a particle and from the mean-field theory, also known as the Lorentz-Lorenz equation.

Polarizability of a dielectric sphere

Let's focus on the electrostatic problem of a single dielectric sphere of radius R_i with dielectric constant ε_i embedded in a host matrix with dielectric constant ε_h and placed in an uniform electric field, which at large distances from the sphere

is directed along the z axis. The asymptotic electric field magnitude is E_0, as indicated in ***Fig.2.3***. Both inside and outside the sphere there are no free charges. As a consequence the electrostatic problem reduces to solve the Laplace equation with azimuthal symmetry ($\nabla^2\Phi(r,\vartheta)=0$) with boundary conditions at $r=R_i$. The general solution for such a problem can be obtained from the Laplace equation in spherical coordinates with azimuthal symmetry[3] [24]

$$\begin{cases} \Phi_{in}(r,\vartheta) = \displaystyle\sum_{l=0}^{\infty} \left[A_l r^l + B_l r^{-(l+1)}\right] P_l(\cos\vartheta) & r < R_i \\ \Phi_{out}(r,\vartheta) = \displaystyle\sum_{l=0}^{\infty} \left[C_l r^l + D_l r^{-(l+1)}\right] P_l(\cos\vartheta) & r > R_i \end{cases} \tag{2.18}$$

The coefficients A_l can be determined from the boundary conditions at the surface sphere, i.e. the continuity of the tangential electric field component ($E_\vartheta^{(in)} = E_\vartheta^{(out)}$) and of the perpendicular electric displacement component ($D_r^{(in)} = D_r^{(out)}$, $\varepsilon_0\varepsilon_i E_r^{(in)} = \varepsilon_0\varepsilon_h E_r^{(out)}$):

$$\begin{cases} -\dfrac{1}{r}\dfrac{\partial\Phi_{in}}{\partial\vartheta}\bigg|_{r=R_i} = -\dfrac{1}{r}\dfrac{\partial\Phi_{out}}{\partial\vartheta}\bigg|_{r=R_i} \\ -\varepsilon_0\varepsilon_i\dfrac{\partial\Phi_{in}}{\partial r}\bigg|_{r=R_i} = -\varepsilon_0\varepsilon_h\dfrac{\partial\Phi_{out}}{\partial r}\bigg|_{r=R_i} \end{cases} \tag{2.19}$$

where Φ_{in} and Φ_{out} are the potentials inside and outside the sphere respectively[4].

Inside the sphere the potential must be finite everywhere. Consequently $B_l = 0$ for all l and $D_0 = 0$ for continuity of Φ at $r = R_i$. From the boundary condition

[3] In spherical coordinates (r,ϑ,ϕ), the Laplace equation can be written in the form

$$\frac{1}{r}\frac{\partial^2}{\partial r^2}(r\Phi) + \frac{1}{r^2\sin\vartheta}\left(\sin\vartheta\frac{\partial\Phi}{\partial\vartheta}\right) + \frac{1}{r^2\sin^2\vartheta}\frac{\partial^2\Phi}{\partial\phi^2} = 0$$

and if the potential Φ posses azimuthal symmetry, using the separation of variable method, it can be written as product $\Phi(r,\vartheta) = [U(r)/r]P(\vartheta)$ and substituting this expression in the Laplace equation we find separate equations for the functions $U(r)$ and $P(\vartheta)$

$$\begin{cases} \dfrac{d^2U}{dr^2} - \dfrac{l(l+1)}{r^2}U = 0 \\ \dfrac{1}{\sin\vartheta}\dfrac{d}{d\vartheta}\left(\sin\vartheta\dfrac{dP}{d\vartheta}\right) + l(l+1)P = 0 \end{cases}$$

where the solution of the first is $U(r) = Ar^{l+1} + Br^{-l}$, while the second, that is the Legendre differential equation, has as solutions the Legendre polynomials of order l.

[4] $\boldsymbol{E} = -\boldsymbol{\nabla}\Phi$, the gradient operator in spherical coordinates in $\boldsymbol{\nabla}_{(r,\theta,\phi)} = \left[\dfrac{\partial}{\partial r}, \dfrac{1}{r}\dfrac{\partial}{\partial\theta}, \dfrac{1}{r\sin\vartheta}\dfrac{\partial}{\partial\phi}\right]$.

at infinity (for $r \to \infty$ $\Phi_{out} \to -E_0 z = -E_0 r\cos\vartheta$) we find that the only non vanishing C_l is $C_1 = -E_0$ (and if $C_0 = 0$ as a result we have also $A_0 = 0$ for potential continuity). The other coefficients are determined from the boundary conditions (2.19) at $r = R_i$. Substituting the (2.18) in (2.19), we have

$$\begin{cases} -\dfrac{1}{R_i}\left[\displaystyle\sum_{l=1}^{\infty} A_l R_i^l \frac{dP_l(\cos\vartheta)}{d\vartheta}\right] = -\dfrac{1}{R_i}\left[C_1 R_i \sin\vartheta + \displaystyle\sum_{l=1}^{\infty} D_l R_i^{-(l+1)} \frac{dP_l(\cos\vartheta)}{d\vartheta}\right] \\ -\varepsilon_0\varepsilon_i\left[\displaystyle\sum_{l=1}^{\infty} l A_l R_i^{l-1} P_l(\cos\vartheta)\right] = -\varepsilon_0\varepsilon_h\left[C_1\cos\vartheta - \displaystyle\sum_{l=1}^{\infty}(l+1) D_l R_i^{-(l+2)} P_l(\cos\vartheta)\right] \end{cases}$$

for $l = 1$ we get

$$\begin{cases} A_1 = C_1 + \dfrac{D_1}{R_i^3} \\ A_1 = \dfrac{\varepsilon_h}{\varepsilon_i}\left[C_1 - 2\dfrac{D_1}{R_i^3}\right] \end{cases} \quad \Rightarrow \quad \begin{cases} A_1 = -\dfrac{3\varepsilon_h}{\varepsilon_i + 2\varepsilon_h} E_0 \\ D_1 = \dfrac{\varepsilon_i - \varepsilon_h}{\varepsilon_i + 2\varepsilon_h} E_0 R_i^3 \end{cases}$$

and for $l > 1$ we get

$$\begin{cases} A_l = \dfrac{D_l}{R_i^{2l+1}} \\ A_l = -\dfrac{\varepsilon_h}{\varepsilon_i}\dfrac{l+1}{l}\dfrac{D_l}{R_i^{2l+1}} \end{cases} \quad \Rightarrow \quad A_l = D_l = 0$$

The potential is therefore

$$\begin{cases} \Phi_{in}(r,\vartheta) = -\dfrac{3\varepsilon_h}{\varepsilon_i + 2\varepsilon_h} E_0 r\cos\vartheta \\ \Phi_{out}(r,\vartheta) = -E_0 r\cos\vartheta + \dfrac{\varepsilon_i - \varepsilon_h}{\varepsilon_i + 2\varepsilon_h} E_0 \dfrac{R_i^3}{r^2}\cos\vartheta \end{cases} \tag{2.20}$$

Outside the sphere the electric potential is the superposition of the potential of external field E_0 and the potential of an electric dipole[5] at the origin of the sphere with dipole moment

$$p = 4\pi\varepsilon_0\varepsilon_h \frac{\varepsilon_i - \varepsilon_h}{\varepsilon_i + 2\varepsilon_h} E_0 R_i^3 \,. \tag{2.21}$$

The polarizability of an inclusion embedded in a background medium is related to its response to an external electric field. Due to the external field $\boldsymbol{E}_0$, the inclusion gains a dipole moment $\boldsymbol{p}$ because of the polarization charges lying on its own surface

[5]An electric dipole $\boldsymbol{p} = p\boldsymbol{e}_z$ in a surrounding medium with dielectric permittivity ε_h is the source of a potential $\Phi(r,\vartheta) = \boldsymbol{n}\cdot\boldsymbol{p}/(4\pi\varepsilon_0\varepsilon_h r^2) = p\cos\vartheta/(4\pi\varepsilon_0\varepsilon_h r^2)$.

and the relation between the two quantities is: $\boldsymbol{p} = \alpha \boldsymbol{E}_0$. Therefore from (2.21) we get the polarizability of a single dielectric sphere embedded in a host matrix with dielectric permittivity ε_h

$$\alpha = V_i 3\varepsilon_0 \varepsilon_h \frac{\varepsilon_i - \varepsilon_h}{\varepsilon_i + 2\varepsilon_h},$$

where $V_i = 4\pi R_i^3/3$ is the volume of the spherical inclusion.

Polarizability of a dielectric ellipsoid

The most general smooth particle of regular shape is an ellipsoid. The natural coordinates for formulating the problem of determining the dipole moment of an ellipsoidal particle, with permittivity ε_i embedded in a host medium with permittivity ε_h, induced by a uniform electrostatic field are the ellipsoidal coordinates (ξ, η, ζ) defined by

$$\begin{aligned}
&\frac{x^2}{a^2+\xi} + \frac{y^2}{b^2+\xi} + \frac{z^2}{c^2+\xi} = 1 && -c^2 < \xi < \infty \\
&\frac{x^2}{a^2+\eta} + \frac{y^2}{b^2+\eta} + \frac{z^2}{c^2+\eta} = 1 && -b^2 < \eta < -c^2 \\
&\frac{x^2}{a^2+\zeta} + \frac{y^2}{b^2+\zeta} + \frac{z^2}{c^2+\zeta} = 1 && -a^2 < \eta < -b^2
\end{aligned}$$

where $a > b > c$ are the ellipsoid's semi-axes [25]. The surfaces $\xi =$ constant are confocal ellipsoids, and the particular ellipsoid $\xi = 0$ coincides with the boundary of the particle. The surfaces $\eta =$ constant are hyperboloids of one sheet, and the surfaces $\zeta =$ constant are hyperboloids of two sheets.

As we have seen from the above problem for the spherical particle (2.20), the electrostatic potential inside the particle Φ_{in} is proportional to the external potential Φ_0 and the potential outside Φ_{out} can be written as the superposition of Φ_0 and Φ_p the potential due to the electric dipole moment of the particle ($\Phi_{out} = \Phi_0 + \Phi_p$).

The potential of external field $\Phi_0 = -E_0 z$ in ellipsoidal coordinates is[6]

$$\Phi_0(\xi,\eta,\zeta) = -E_0\sqrt{\frac{(c^2+\xi)(c^2+\eta)(c^2+\zeta)}{(a^2-c^2)(b^2-c^2)}}\,.$$

Laplace's equation in ellipsoidal coordinates is

$$\nabla^2\Phi = (\eta-\zeta)f(\xi)\frac{\partial}{\partial\xi}\left(f(\xi)\frac{\partial\Phi}{\partial\xi}\right) + (\zeta-\xi)f(\eta)\frac{\partial}{\partial\eta}\left(f(\eta)\frac{\partial\Phi}{\partial\eta}\right) + \\ + (\xi-\eta)f(\zeta)\frac{\partial}{\partial\zeta}\left(f(\zeta)\frac{\partial\Phi}{\partial\zeta}\right) = 0\,,$$

where $f(s) = \sqrt{(s+a^2)(s+b^2)(s+c^2)}$. To achieve the solution of the problem, we can exploit the result obtained in the case of scattering by a sphere, so that we postulate that the potentials Φ_{in} and Φ_p are of the form

$$\Phi_{in}(\xi,\eta,\zeta) = C_{in}F_{in}(\xi)\sqrt{(c^2+\eta)(c^2+\zeta)}\,,$$
$$\Phi_p(\xi,\eta,\zeta) = C_pF_p(\xi)\sqrt{(c^2+\eta)(c^2+\zeta)}\,.$$

Substituting this form for Φ in the Laplace's equation in ellipsoidal coordinates, it follows that $F_{in,p}(\xi)$ satisfies the ordinary differential equation

$$F''_{in,p}(\xi) + \frac{f'(\xi)}{f(\xi)}F'_{in,p}(\xi) - \left(\frac{a^2+b^2}{4} + \frac{\xi}{2}\right)F_{in,p}(\xi) = 0$$

and one of the two linearly independent solutions is $F_{in}(\xi) = \sqrt{\xi+c^2}$ (since Φ_{in} is proportional to Φ_0). The second solution $F_p(\xi)$ can be obtained exploiting the variation of parameters method of linear ordinary differential equation and the boundary condition $\lim_{\xi\to\infty} F_2(\xi) = 0$

$$F_2(\xi) = F_1(\xi)\int_\xi^\infty \frac{ds}{F_1^2(s)f(s)}\,.$$

[6]The relation between cartesian coordinates (x,y,z) and ellipsoidal coordinates (ξ,η,ζ) are

$$x^2 = \frac{(a^2+\xi)(a^2+\eta)(a^2+\zeta)}{(b^2-a^2)(c^2-a^2)}\,,$$
$$y^2 = \frac{(b^2+\xi)(b^2+\eta)(b^2+\zeta)}{(a^2-b^2)(c^2-b^2)}\,,$$
$$z^2 = \frac{(c^2+\xi)(c^2+\eta)(c^2+\zeta)}{(a^2-c^2)(b^2-c^2)}\,.$$

Imposing the condition of continuity for Φ and the continuity of the electric displacement normal component at $\xi = 0$, we set the two constant C_{in} and C_{out}

$$\Phi_{in}(0,\eta,\zeta) = \Phi_0(0,\eta,\zeta) + \Phi_p(0,\eta,\zeta)$$

$$\Rightarrow \quad C_{in} = -\frac{E_0}{\sqrt{(a^2-c^2)(b^2-c^2)}} + C_p \int_0^\infty \frac{ds}{(s+c^2)f(s)}\,;$$

$$\varepsilon_i \frac{\partial \Phi_{in}}{\partial \xi} = \varepsilon_h \frac{\partial \Phi_0}{\partial \xi} + \varepsilon_h \frac{\partial \Phi_0}{\partial \xi}$$

$$\Rightarrow \quad \varepsilon_i C_{in} = -\frac{\varepsilon_h E_0}{\sqrt{(a^2-c^2)(b^2-c^2)}} + \varepsilon_h C_p \left[\int_0^\infty \frac{ds}{(s+c^2)f(s)} - \frac{2}{abc}\right];$$

$$C_{in} = \frac{-E_0}{\sqrt{(a^2-c^2)(b^2-c^2)}} \frac{1}{1 + \dfrac{abc}{2}\displaystyle\int_0^\infty \frac{ds}{(s+c^2)f(s)} \frac{\varepsilon_i - \varepsilon_h}{\varepsilon_h}}\,,$$

$$C_p = \frac{-E_0}{\sqrt{(a^2-c^2)(b^2-c^2)}} \frac{\dfrac{abc}{2}\displaystyle\int_\xi^\infty \frac{ds}{(s+c^2)f(s)} \frac{\varepsilon_h - \varepsilon_i}{\varepsilon_h}}{1 + \dfrac{abc}{2}\displaystyle\int_0^\infty \frac{ds}{(s+c^2)f(s)} \frac{\varepsilon_i - \varepsilon_h}{\varepsilon_h}}\,.$$

At distance r from the origin which is much greater than the largest semi-axes a

$$\int_\xi^\infty \frac{ds}{(c^2+s)f(s)} = \int_\xi^\infty \frac{ds}{s^{5/2}} = \frac{2}{3}\xi^{-3/2}\,,$$

therefore the potential Φ_p becomes

$$\Phi_p = \frac{-E_0 \cos\vartheta}{r^2} \frac{\dfrac{abc}{3}\dfrac{\varepsilon_h - \varepsilon_i}{\varepsilon_h}}{1 + \dfrac{abc}{2}\displaystyle\int_0^\infty \frac{ds}{(s+c^2)f(s)} \frac{\varepsilon_i - \varepsilon_h}{\varepsilon_h}}$$

and it shows the electric dipole potential form for a dipole momentum

$$p = V_i \varepsilon_0 \varepsilon_h \frac{\varepsilon_i - \varepsilon_h}{\varepsilon_h + L_z(\varepsilon_i - \varepsilon_h)} E_0\,,$$

where $V_i = 4\pi abc/3$ is the volume of ellipsoidal particle, L_z is the depolarization factor of ellipsoid along z direction, while along j direction ($j = x, y, z$; $a_x = a$, $a_y = b$, $a_z = c$) it is

$$L_j = \frac{abc}{2}\int_0^\infty \frac{ds}{(a_j^2+s)f(s)}\,.$$

The polarizability of a single dielectric ellipsoid particle in an isotropic host is a tensor which in the coordinate system of the ellipsoid axes shows a diagonal form

$$\alpha_{jj} = \varepsilon_0 V_i(\varepsilon_i - \varepsilon_h)[\varepsilon_h + L_j(\varepsilon_i - \varepsilon_h)]^{-1}\varepsilon_h\,. \tag{2.22}$$

Anisotropic host

The electrostatic problem of finding the polarizability of a single spherical particle embedded in an isotropic host matrix is invariant under rotations around the center of sphere. Such a central symmetry can be broken by a different form of the inclusions or by the anisotropic nature of the host. We have seen above that the electrostatic response of an ellipsoid in an isotropic medium (which we have achieved by a suitable change from cartesian to ellispoidal coordinates) has tensorial kind because it depends on the reciprocal orientation between ellipsoidal axes and electric direction. In the same way, one can face the electrostatic problem of a single spherical particle within an anisotropic host matrix. The optical indicatrix of a anisotropic medium, in the optical principal axes, is an ellipsoidal surface and the length of each axis is equal to the principal electric permittivity along considered direction (§Appendix A). The result (2.22) can be exploited by suitably scaling cartesian coordinates as $x \to x\sqrt{\varepsilon_{hx}/\varepsilon_{hj}}$ $y \to y\sqrt{\varepsilon_{hy}/\varepsilon_{hj}}$ and $z \to z\sqrt{\varepsilon_{hz}/\varepsilon_{hj}}$, so that the spherical particle looks ellipsoidal in the new coordinates. In this way, we get the polarizability tensor of a spherical particle embedded in an anisotropic host matrix whose optical principal axes coincide with the axes of the artificial ellipsoidal particle

$$\alpha_{jj} = \varepsilon_0 V_i(\varepsilon_i - \varepsilon_{hj})[\varepsilon_{hj} + L_j(\varepsilon_i - \varepsilon_{hj})]^{-1}\varepsilon_{hj}\,, \tag{2.23}$$

where the depolarization factor L_j is

$$L_j = \frac{1}{2}\int_0^\infty \frac{\varepsilon_{hj}ds}{(1+\varepsilon_{hj}s)\sqrt{(1+\varepsilon_{hx}s)(1+\varepsilon_{hy}s)(1+\varepsilon_{hz}s)}}\,, \tag{2.24}$$

which, in the isotropic limit, it reduces to $L_j = 1/3$.

Multi-component Maxwell Garnett mixing rules

Let consider a homogeneous mixture of N different kinds of spherical particles in an anisotropic host matrix and in a reference frame coinciding with the host optical principal axes (so that the electric permittivity tensor is diagonal). In the Lorentz model, the field experienced by a particle is not the macroscopically averaged field

$\boldsymbol{E}$ but it is $\boldsymbol{E}_L$ the electric local field which can be written as

$$\boldsymbol{E}_L = \boldsymbol{E} + \boldsymbol{E}_S \,, \tag{2.25}$$

where $\boldsymbol{E}$ is the macroscopic field of Maxwell's equations and $\boldsymbol{E}_S$ is the field due to the polarization charges lying on the surface of Lorentz sphere. It can be proved that $\boldsymbol{E}_S$ for a spherical particle in an isotropic host is $\boldsymbol{E}_S = \boldsymbol{P}/(3\varepsilon_0\varepsilon_h)$ and the factor $1/3$ represents the depolarization factor of particle of such shape. Generalizing this result to the anisotropic case, the local Lorentz field is

$$(E_L)_j = E_j + \frac{1}{\varepsilon_0}[\varepsilon_{hj}]^{-1} L_j P_j \,, \tag{2.26}$$

where the depolarization factor L_j is represented by relation (2.24) and P_j is the electric polarization of homogeneous mixture. The macroscopic polarization P_j is defined as the volume electric dipole moment $P_j = \sum_{l=1}^{N} n^{(l)} p_j^{(l)}$, where $n^{(l)}$ is the volume density particles of l-th kind and $p_j^{(l)}$ is j-th dipole moment component and it is related to the polarizability $\alpha_{jj}^{(l)}$ by $p_j^{(l)} = \alpha_{jj}^{(l)}(E_L)_j$. Using the definition of local Lorentz field (2.26) and the commutation rules between the polarizability tensor $\alpha^{(l)}$ and the electric permittivity tensor ε_h

$$P_j = \sum_{l=1}^{N} n^{(l)} p_j^{(l)} = \sum_{l=1}^{N} n^{(l)} \alpha_{jj}^{(l)} (E_L)_j = \sum_{l=1}^{N} n^{(l)} \alpha_{jj}^{(l)} E_j + \frac{1}{\varepsilon_0}[\varepsilon_{hj}]^{-1} \sum_{l=1}^{N} n^{(l)} \alpha_{jj}^{(l)} L_j P_j \,,$$

$$P_j = \left[1 - \frac{1}{\varepsilon_0}[\varepsilon_{hj}]^{-1} \sum_{l=1}^{N} n^{(l)} \alpha_{jj}^{(l)} L_j \right]^{-1} \sum_{l=1}^{N} n^{(l)} \alpha_{jj}^{(l)} E_j \,.$$

Due to particles shape, the effective permittivity of the mixture is anisotropic and the macroscopic electric displacement j-th component

$$D_j = \varepsilon_0 \varepsilon_{jj}^{(eff)} E_j = \varepsilon_0 \varepsilon_{hj} E_j + P_j =$$

$$= \varepsilon_0 \left\{ \varepsilon_{hj} + \frac{1}{\varepsilon_0} \left[1 - \frac{1}{\varepsilon_0}[\varepsilon_{hj}]^{-1} \sum_{l=1}^{N} n^{(l)} \alpha_{jj}^{(l)} L_j \right]^{-1} \sum_{l=1}^{N} n^{(l)} \alpha_{jj}^{(l)} \right\} E_j \tag{2.27}$$

and by the polarizability definition (2.23), the effective Maxwell-Garnett electric permittivity of a homogeneous mixture of N kinds of spherical particles with per-

mittivity $\varepsilon_i^{(l)}$ in an anisotropic host matrix is

$$\varepsilon_{jj}^{(eff)} = \left\{ 1 + \frac{1}{1 - \sum_{l=1}^{N} \frac{f^{(l)}(\varepsilon_i^{(l)} - \varepsilon_{hj})}{\varepsilon_{hj} + L_j(\varepsilon_i^{(l)} - \varepsilon_{hj})} L_j} \sum_{l=1}^{N} \frac{f^{(l)}(\varepsilon_i^{(l)} - \varepsilon_{hj})}{\varepsilon_{hj} + L_j(\varepsilon_i^{(l)} - \varepsilon_{hj})} \right\} \varepsilon_{hj} \,,$$

where $f^{(l)} = n^{(l)} V^{(l)}$ is the filling fraction of l-th kind spherical particles. In particular, if there is only one kind of spherical particles in the host, the effective electric permittivity becomes

$$\varepsilon_{jj}^{(eff)} = \left[1 + \frac{f(\varepsilon_i - \varepsilon_{hj})}{\varepsilon_{hj} + (1-f) L_j(\varepsilon_i - \varepsilon_{hj})} \right] \varepsilon_{hj} \,. \tag{2.28}$$

Multi-component Bruggeman mixing rules

Let us consider spherical particles of different materials ($\varepsilon_i^{(l)}$) that are dispersed with a volume filling factors $f^{(l)} = n^{(l)} V_i^{(l)}$ in an isotropic host matrix with a dielectric constant of ε_h. Using (2.27) the effective electric permittivity is

$$\varepsilon_{eff} = \varepsilon_h + \frac{\sum_{l=1}^{N} \frac{n^{(l)} \alpha^{(l)}}{\varepsilon_0}}{1 - \sum_{l=1}^{N} \frac{n^{(l)} \alpha^{(l)}}{3 \varepsilon_0 \varepsilon_h}} \quad \Rightarrow \quad \frac{\varepsilon_{eff} - \varepsilon_h}{\varepsilon_{eff} + 2\varepsilon_h} = \sum_{l=1}^{N} f^{(l)} \frac{\varepsilon_i^{(l)} - \varepsilon_h}{\varepsilon_i^{(l)} + 2\varepsilon_h} \,.$$

If the inclusions are present in a symmetric manner the distinction between inclusions and hosts vanish and therefore $\varepsilon_h = \varepsilon_{eff}$ and we have

$$\sum_{l=1}^{N} f^{(l)} \frac{\varepsilon_i^{(l)} - \varepsilon_{eff}}{\varepsilon_i^{(l)} + 2\varepsilon_{eff}} = 0 \,,$$

whose solution provides the effective electric permittivity in Bruggeman geometry.

2.2.3 Nanowire media

A nanowire media is a material composed of aligned arrays of metallic nanowires in a dielectric matrix. ***Fig.2.4*** schematically illustrates the structure of metallic

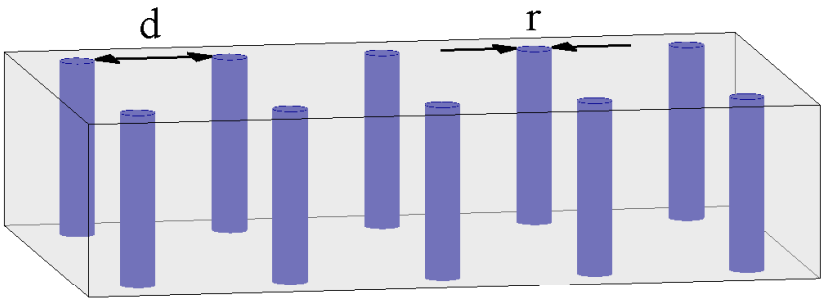

Figure 2.4: A nanowire media, a material composed of aligned arrays of metallic nanowires in a dielectric matrix; r is the wire radius and d the distance between two neighboring wires.

nanowires embedded in a dielectric host[7]. When the geometric parameters, i.e., the wire radius (r) and the distance between two neighboring wires (d), are much smaller than the free space wavelength (λ_0) of the incident electromagnetic wave, the underlying system can be considered as an effective uniaxial medium [14] and the *dynamic Maxwell-Garnett theory* [17, 28] can be utilized to determine the effective dielectric permittivity along the direction perpendicular to wires ($\varepsilon_\perp$), while the effective dielectric permittivity along parallel direction to wires is settled by a simple arithmetic average ($\varepsilon_{||}$), therefore they are given by the following equations [13]:

$$\varepsilon_\perp = \varepsilon_h + \frac{f\varepsilon_h(\varepsilon_{mw} - \varepsilon_h)}{\varepsilon_h + (1-f)L_{eff}(\varepsilon_{mw} - \varepsilon_h)}\,, \tag{2.29}$$

$$\varepsilon_{||} = f\varepsilon_{mw} + (1-f)\varepsilon_h\,, \tag{2.30}$$

where f is the filling ratio of metal, ε_{mw} and ε_h are dielectric permittivity of metal and dielectric respectively and L_{eff} is the effective depolarization factor along the direction perpendicular to nanowires. The so-called dynamical Maxwell-Garnett model is a simple modification of Maxwell-Garnett theory which takes into account both particles size and shape effects. As we have seen above, the polarizability

[7]This structure can be fabricated by electrochemically growing metallic nanowires in a porous alumina template, which is prepared by the anodization method in a self-organized way [26]; such a method has proved to be a low-cost and high-yield technique for fabricating different kinds of nanostructures including nanowires, nanodots and nanotubes [27].

of a single dielectric ellipsoid particle in a host matrix (2.22) is a function of the dielectric permittivity of the particle (ε_i) and host medium (ε_h) and also the size and shape of the particle by the depolarization factor (L_{eff}). In the small particle (or Rayleigh scattering) limit, the complex polarizability of the particle is given by (2.22), when the size of inclusions increase relative to λ_0, the higher order electric multipole terms become important [28]. In 1983, Meier and Wokaun [29] derived an alternate expression for the depolarization factor. Specific for spheres, their model defines an effective depolarization factor L_{eff}, which is related to sphere radius a via

$$L_{eff} = \frac{1}{3} - \frac{1}{3}\left(\frac{2\pi}{\lambda_0}a\right)^2 - \frac{2}{9}\left(\frac{2\pi}{\lambda_0}a\right)^2 i\,, \tag{2.31}$$

where the first term on the right-handed site of (2.31) is the Lorentz depolarizing factor ($L = 1/3$) for spheres. The second term involves dynamic depolarization and accounts for the fact that a particle that is not small relative to the incident wavelength λ_0 will experience different phases of the incident field. The third term accounts for damping of the dipole by radiative losses and results in broadening and strongly decreased magnitude of the resonance enhancement for large particle volumes.

2.3 Experimental validations of effective model

All the homogenization techniques with their own effective medium theories allow to predict approximately the optical behavior of actual composites. There are two general constraints: 1) each constituent is present in the whole in grains large enough that it may be described by its bulk optical properties and 2), at the same time, the typical grain dimensions and spacings must be much smaller than an optical wavelength, so that the composite may be described by effective optical parameters, which are related to the constituent parameters.

Gehr and Boyd [30] have provided a brief review of the optical properties of composite materials, discussing the experimental results through the suitable effective medium theory defined by the composite geometries. An example of a composite is

stained glass, i.e., glass doped with small metal particles. The dimensions of the particles are typically on the order of hundreds of angstroms, which is much smaller than optical wavelengths. It is obvious that such composites have significantly different properties than their constituents. The glass is nonabsorbing throughout the visible spectrum, the metal is highly absorbing and reflective throughout the same range, but the composite displays a resonance absorption peak within the visible, which gives the glass its characteristic coloring. In an effort to explain this phenomenon, Maxwell-Garnett [22] developed one of the earliest effective medium theories and the effective dielectric constant accurately predicted the location of the resonance in the visible part of the spectrum. Under the assumption that the inclusion radius was much smaller than the typical spacing between inclusions, which in turn was much smaller than an optical wavelength, an effective dielectric constant could be determined for the composite. Observing that a metal sphere in the presence of an oscillating electric field emits radiation as if it were an electric dipole, Maxwell-Garnett replaced the spheres in the model by the equivalent point dipoles, i.e., he ignored their finite size. Maxwell-Garnett theory is strictly valid only in the limit where particle dimensions and separation distances are infinitely small relative to the wavelength, but it has the advantage that it can be easily generalized to particles of various shapes. The expression (2.28) for an isotropic host and spherical inclusions

$$\varepsilon^{(eff)} = \frac{\varepsilon_i(1+2f) + 2\varepsilon_h(1-f)}{\varepsilon_i(1-f) + \varepsilon_h(2+f)}\varepsilon_h \,,$$

displays an important feature: for metal inclusion particles, which have a negative real part of the dielectric constant, the real part of the denominator may go to zero, implying the existence of a resonance. Maxwell-Garnett compared this resonance with the observed colors of several metal-doped glasses. For the samples which met his model criteria, the agreement between the theory and experimental observations was very good.

Another important concept in the derivation of effective medium theories is that of local fields; the electric field driving the polarization of an inclusion particle is not the same as the macroscopic electric field appearing in Maxwell's equations.

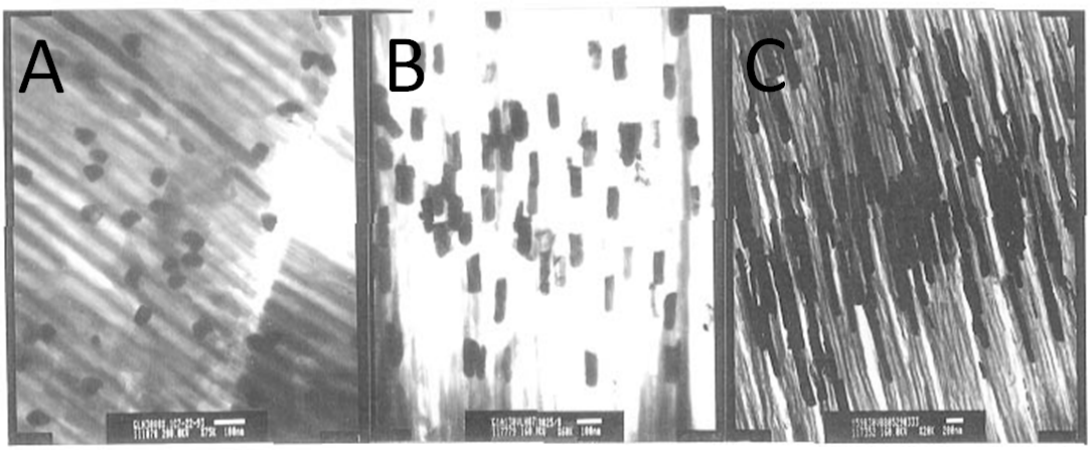

Figure 2.5: Transmission electron micrographs of transverse sections of Au nanoparticle/alumina membrane composites. The membranes had a pore diameter of 52 nm. Defining as Aspect ratio the ratio between particle length and its diameter: (A) Aspect ratio = 1.3; (B) Aspect ratio = 2.7 and (C) Aspect ratio = 7.8.

Instead it is a local field whose value depends on the polarization of the surrounding medium as well as the applied field. This distribution of the field among the constituents explains why the optical constants of the effective medium are not simply the weighted averages of those of the constituents. Local-field effects play a role to be considered in each of the composite geometries.

G. L. Hornyak et al. [31] have been exploring the optical properties of nanoscopic gold particles prepared by electrochemically depositing Au within the pores of alumina membranes. In particular, they are interested in investigating the effect of Au nanoparticle diameter (determined by the pore diameter of the alumina membrane) and length (determined by the quantity of Au deposited within the pores, ***Fig.2.5***) on the position of the plasmon resonance adsorption of the nanoparticle. They have used Maxwell-Garnett effective medium theory as a guide for modeling the optical properties of these Au nanoparticle/alumina membrane composites. However, Maxwell-Garnett theory is rigorously applicable only in the limit of metal nanoparticles with infinitesimally small diameters in comparison with the wavelength of the incident electromagnetic wave. As a result, the position of the plasmon reso-

nance absorption predicted theoretically using Maxwell-Garnett theory was always blue-shifted relative to the position of the experimental absorption band. Therefore they have used the modified form of Maxwell-Garnett theory, called the dynamic Maxwell-Garnett theory (which takes into account both particles size and shape effects by the effective depolarization factor (2.31)), to model the optical properties of such Au nanoparticles (***Fig.2.6***). As the diameter of the Au nanoparticle decreased, the position of the experimental plasmon resonance band (as defined by the wavelength of maximum absorption intensity, λ_{max}) approached the λ_{max} predicted by Maxwell-Garnett theory. They have prepared Au nanoparticles with diameters of 52 nm, 32 nm, 22 nm and 16 nm. They have found, that as the Au nanoparticle diameter decreases, the experimental λ_{max} approaches the Maxell-Garnett-predicted value (***Fig.2.7***). Furthermore, the λ_{max} values for the smallest diameter particles (16 nm) are essentially identical with the values predicted by Maxwell-Garnett theory. Hence, the Maxwell-Garnett-predicted plasmon resonance absorption limit can be used as comparison parameter to evaluate the dimensions in preparing metal nanoparticles.

Other examples of good agreement between theoretical and experimental results are given by E. Wäckelgard [32] and Y. Rao works [33].

In the first paper, the experimental dielectric function of porous alumina in the infrared region is compared with the Maxwell-Garnett model. The effective dielectric function has been calculated using Maxwell-Garnett effective-medium theory for a two-component anisotropic medium consisting of air-filled cylindrical pores perpendicular to the surface in an alumina matrix with optical constants of non-porous evaporated alumina. As shown by ***Fig.2.8***, the theoretical and experimental results are in good agreement. In this paper the Maxwell-Garnett effective theory shows that the redshift of the longitudinal optical phonon (LO mode) absorption for p-polarized light can be explained by the presence of pores in the alumina sample.

In the second one, nanostructure polymer-ceramic composite with high dielectric constant has been developed for embedded capacitor application. This polymer-ceramic system consists of ceramic particle randomly placed within the polymeric

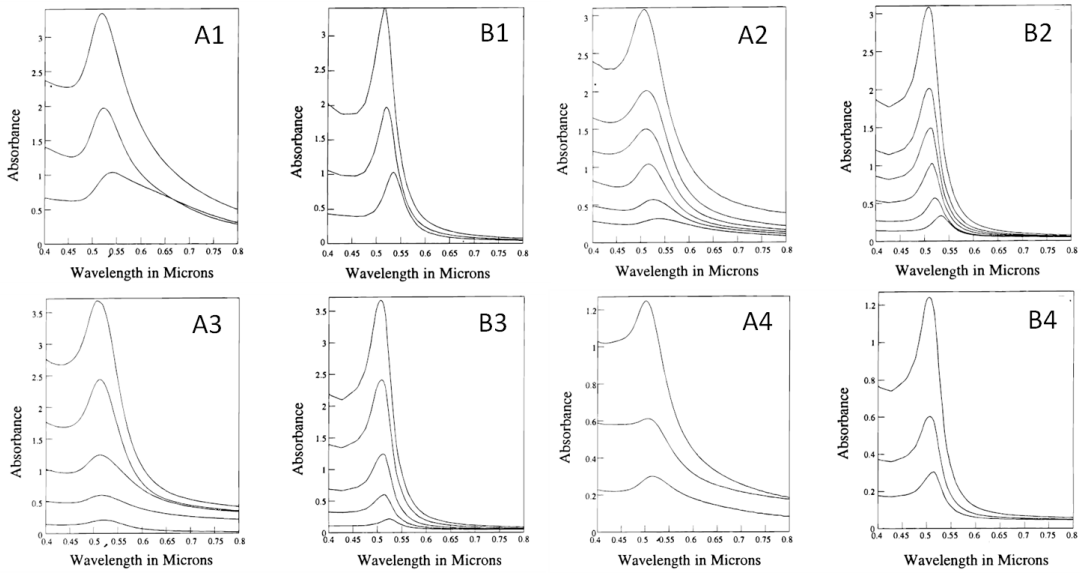

Figure 2.6: Experimental (A) and dynamic Maxwell-Garnett simulated (B) absorption spectra for membranes containing 52 nm (1), 32 nm (2), 22 nm (3) and 16 nm (4) diameter Au nanoparticles. For every diameter curves for particles with different aspect ratio are shown. The uppermost curve is fr the highest aspect ratio nanoparticle and the lowermost curve is for the lowest aspect ratio nanoparticle. [31]

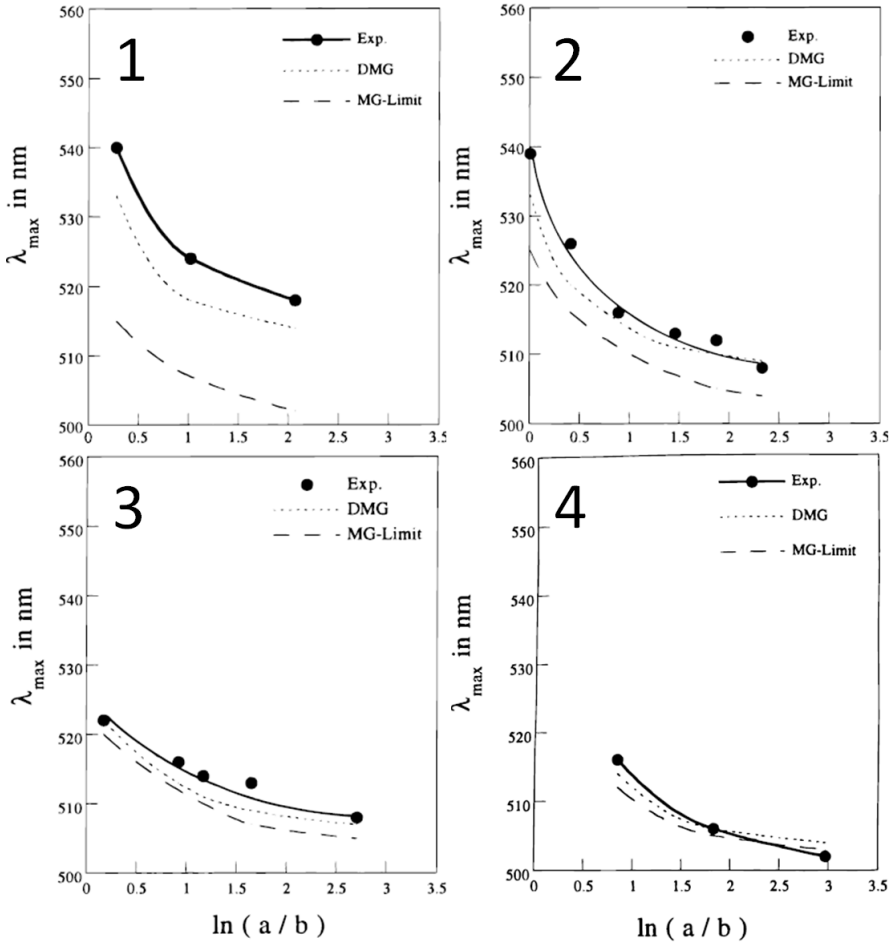

Figure 2.7: Plot of λ_{max} for experimental and simulated absorption spectra vs natural logarithm of the aspect ratio of the Au nanoparticle. The aspect ratio is defined as a/b, where a is the length and b is the diameter of the nanoparticle. These data are for 52 nm (1), 32 nm (2), 22 nm (3) and 16 nm (4) diameter nanoparticles. The experimental data are in bold (with data points). The dynamic Maxwell-Garnett simulated results are the dotted curve, while the Maxwell-Garnett simulated results are the dashed curve [31].

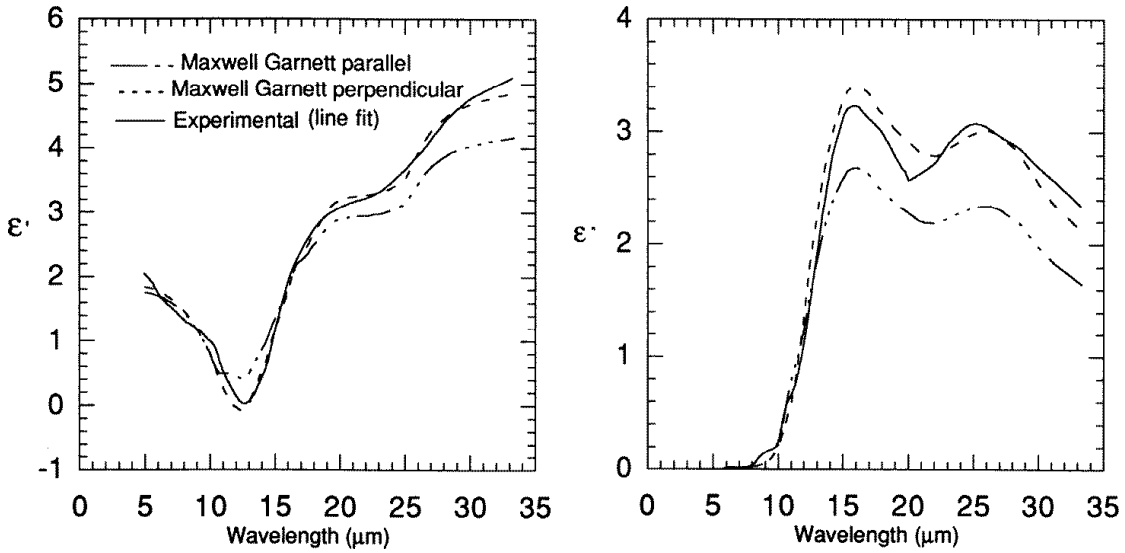

Figure 2.8: The effective dielectric function (the real part on the left and the imaginary part on the right), obtained using Maxwell-Garnett effective-medium theory, is compared with the experimental dielectric function. The pores in alumina sample are regarded as cylinders perpendicular to the surface. The figure shows the components of the theoretical dielectric function parallel and perpendicular to the surface. The experimental and calculated dielectric functions demonstrate that there is good agreement, especially with $\varepsilon_{\perp}^{(eff)}$ [32].

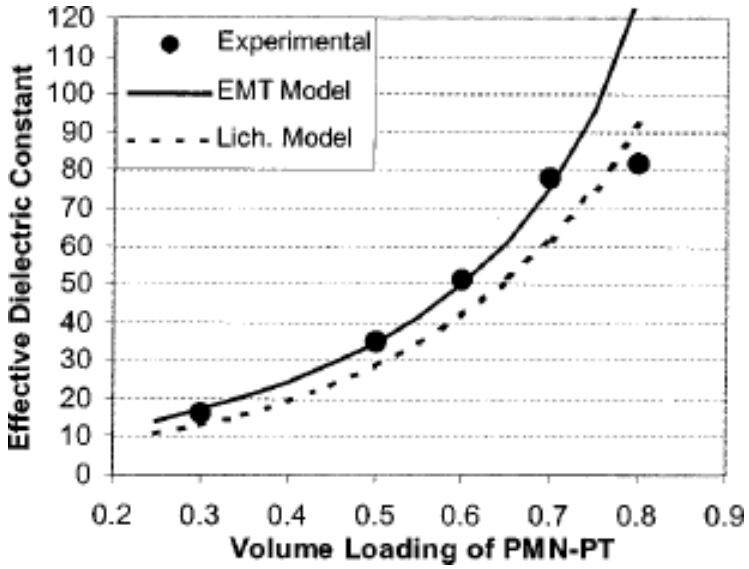

Figure 2.9: Maxwell-Garnett effective medium model prediction (solid curve), modified Lichtenecker prediction (dash curve) and experimental results (dots) of the effective dielectric constant of polymer-ceramic composite [33].

epoxy resin. This work tried to use Marwell-Garnett effective medium theory to set up a numerical model that can precisely predict the dielectric constant of polymer-ceramic nanocomposite. The ***Fig.2.9*** shows the comparison between the experimental results of effective dielectric constant and two numerical model prediction: the effective medium theory and the modified Lichtenecker model[8] and it is evident that the agreement between theoretical model and experimental results is much better for the Maxwell-Garnett model than modified Lichtenecker model.

[8]One of the most commonly used equation to study the dielectric behavior of composite systems or randomly dispersed mixtures is the Lichtenecker logarithmic law and it is written for a two-component system as $\log \varepsilon^{(eff)} = f_1 \log \varepsilon_1 + f_2 \log \varepsilon_2$ (f_i is the volume occupied by material i and ε_i is the dielectric constant of corresponding material). The modified-form of Lichtenecker equation is $\log \varepsilon^{(eff)} = \log \varepsilon_1 + f_2(1-k)\log(\varepsilon_2/\varepsilon_1)$, where k is a fitting constant.

3 Metamaterial families and applications

3.1 Negative index materials

The dielectric permittivity ε and magnetic permeability μ are the fundamental characteristic quantities which fully determine the propagation of electromagnetic waves in matter. The optical properties of a transparent material are often more conveniently described by a different parameter, the refractive index n, given by $n = \sqrt{\varepsilon\mu}$. All known transparent materials have a positive index since ε and μ are both positive. The allowed range of material response does not preclude us from considering a medium for which both ε and μ are negative. Many metals, silver and gold for example, have negative ε at wavelengths in the visible spectrum. In ***Fig.3.1*** the material dielectric response at one of its resonances is depicted. Generally, a spring-mass oscillator is used to picture the medium as a set of harmonically bound charges. When the frequency is lower than the resonance frequency ω_0, the function $\Re[\varepsilon(\omega)]$ (or $\Re[\mu(\omega)]$) is increasing and positive so that the response (P for electric resonances and M for magnetic ones) is parallel to the charge displacement. On the other side of the resonance peak, the function can take a negative value, so that the response is anti-parallel to the driving force.

More than 35 years ago Victor Veselago pondered the properties of a peculiar medium [3] with both ε and μ simultaneously real and negative. Since the product $\varepsilon\mu$ is positive, the square root accordingly gives a real refractive index. Yet, there is an ambiguity when choosing the correct sign of n since mathematically there are two

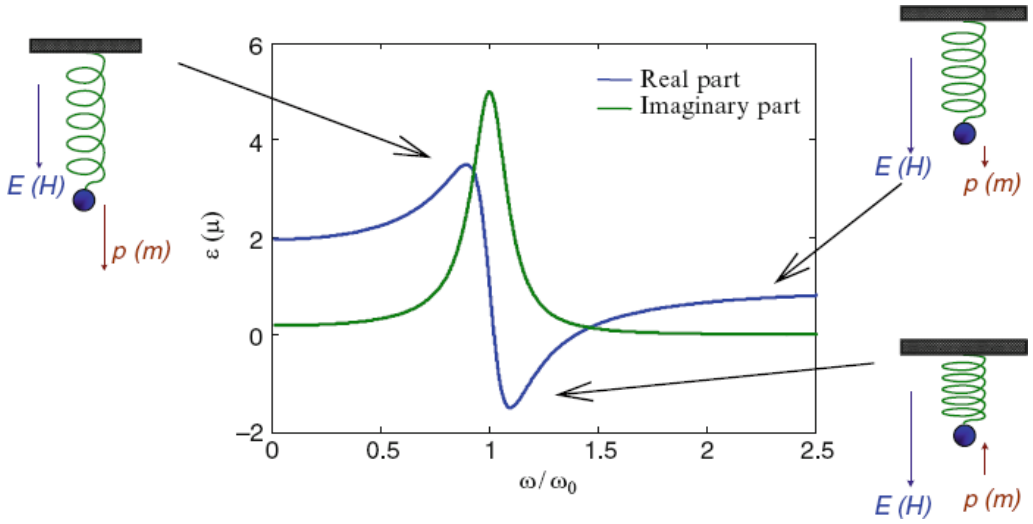

Figure 3.1: The electromagnetic responses around a resonance. The three spring-mass oscillators are used as a mechanic analogue [1].

possible solutions: $n = \pm\sqrt{\varepsilon\mu}$. The correct sign has to be assigned in such a way for satisfying the causality condition. For any realistic passive medium, both ε and μ have a positive imaginary part (even though they may be quite small compared with corresponding real parts). Considering a medium with $\varepsilon = -\varepsilon' + i\varepsilon''$ and $\mu = -\mu' + i\mu''$, where ε', ε'', μ' and μ'' are positive, we have

$$n = \pm\sqrt{(-\varepsilon' + i\varepsilon'')(-\mu' + i\mu'')} = \pm\sqrt{\varepsilon'\mu' - \varepsilon''\mu'' - i(\varepsilon''\mu' + \varepsilon'\mu'')}\,,$$

$$n = \pm\sqrt{|n|}[\cos(\vartheta/2) + i\sin(\vartheta/2)]\,,$$

$$|n| = (\varepsilon'\mu')^2 + (\varepsilon''\mu'')^2 + (\varepsilon''\mu')^2 + (\varepsilon'\mu'')^2\,,$$

$$\cos\vartheta = \frac{\varepsilon'\mu' - \varepsilon''\mu''}{|n|} \qquad \sin\vartheta = -\frac{\varepsilon''\mu' + \varepsilon'\mu''}{|n|}\,,$$

so that $\sin\vartheta < 0$, whilst $\cos\vartheta$ can be either positive or negative

$$\text{if } \varepsilon'\mu' - \varepsilon''\mu'' > 0 \quad \Rightarrow \quad \cos\vartheta > 0 \;\Rightarrow \quad -\frac{\pi}{2} < \vartheta < 0 \quad \Rightarrow \quad -\frac{\pi}{4} < \frac{\vartheta}{2} < 0$$

$$\text{if } \varepsilon'\mu' - \varepsilon''\mu'' < 0 \quad \Rightarrow \quad \cos\vartheta < 0 \;\Rightarrow \quad -\pi < \vartheta < -\frac{\pi}{2} \quad \Rightarrow \quad -\frac{\pi}{2} < \frac{\vartheta}{2} < -\frac{\pi}{4}$$

and in both cases

$$\cos(\vartheta/2) > 0 \quad \wedge \quad \sin(\vartheta/2) < 0 \quad \Rightarrow \quad n = \pm\sqrt{|n|}[\cos(\vartheta/2) - i|\sin(\vartheta/2)|]\,.$$

The imaginary part of n has to be positive for any passive material. Therefore in both cases, the minus sign has to be chosen when the real parts of both ε and μ are negative and the term used to identify such an unconventional material is *negative index material*.

As stated above, the first systematic study of the general properties of a hypothetical medium with a negative refractive index is due to Veselago. He analyzed the propagation features of electromagnetic waves interacting with such a medium and pointed out that when both ε and μ are simultaneously negative, the negative square root must be chosen in the refractive index equation. Since the phase velocity of the radiation is proportional to the real part of the refractive index, waves propagating in negative index materials have the flow of energy antiparallel to the phase velocity. For a plane wave $e^{i(nkz-\omega t)}$ propagating in the z direction with free-space wave-vector $\boldsymbol{k}$ and angular frequency ω in a negative index material, the phase-fronts travel in the opposite direction to their corresponding counterparts in standard materials. A discussion of the relations among the vectors $\boldsymbol{E}$, $\boldsymbol{H}$ and $\boldsymbol{k}$ clarifies such observation. For a plane wave, Maxwell's curl equations (2.2) give the following relations for the three vectors:

$$\begin{cases} \boldsymbol{k} \times \boldsymbol{E} = \omega \mu_0 \mu \boldsymbol{H} \\ \boldsymbol{k} \times \boldsymbol{H} = -\omega \varepsilon_0 \varepsilon \boldsymbol{E} \end{cases}$$

Thus for a common material with positive ε and μ, the vectors $\boldsymbol{E}$, $\boldsymbol{H}$ and $\boldsymbol{k}$ form a right-handed triplet and $\boldsymbol{k}$ is parallel to the Poynting vector $\boldsymbol{S} = \boldsymbol{E} \times \boldsymbol{H}$. In a negative index material where both ε and μ are negative, from the above equations it is clear that the vectors $\boldsymbol{E}$, $\boldsymbol{H}$ and $\boldsymbol{k}$ form a left-handed triplet. Note that now the wave-vector $\boldsymbol{k}$ is anti-parallel to the Poynting vector. This is the reason why negative index material are sometimes called *left-handed materials*, term introduced by Veselago. Left-handed materials are probably the most prominent class among all the other metamaterial ones. In fact, during the early years of metamaterial research, the idea of a negative index of refraction was emphasized so much to the point of regarding the term metamaterial as synonymous of negative index material or left-handed material.

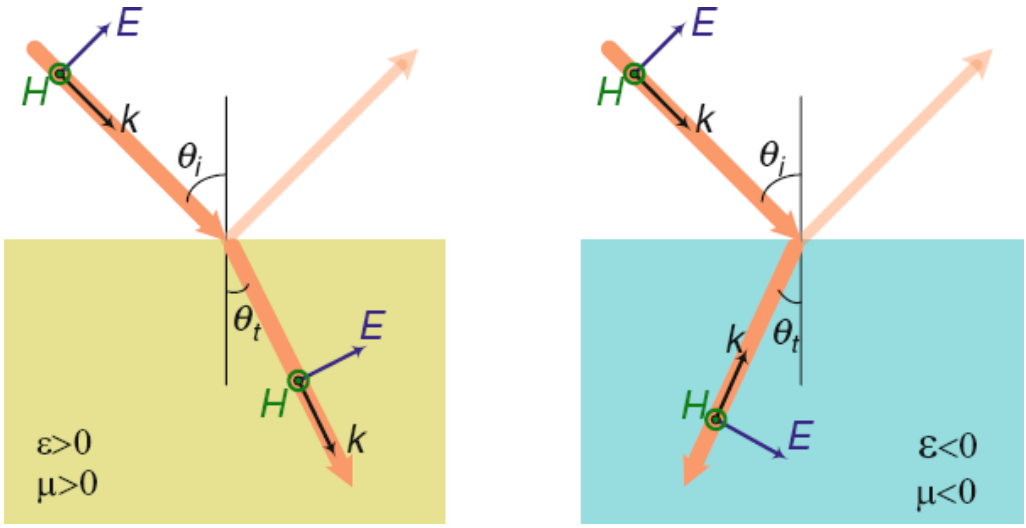

Figure 3.2: The refraction of a light beam when passed through the boundary of air and a Positive index material (*left*) or a negative index material (*right*) [1].

One of most remarkable phenomenon occurring in negative refractive index materials is *negative refraction*. Snell's law relates the refraction angle to the incident one of light traveling across the interface between two media of different refractive indices: $n_1 \sin \vartheta_i = n_2 \sin \vartheta_t$. If we extend this law to account for negative refraction, when a light beam passes through the boundary between a positive index material and a negative index material, the refraction angle ϑ_t is negative. Therefore, the refracted beam bends along the same side of the interface normal as the incident beam (***Fig.3.2***).

In 2001, the first the experimental verification of negative refraction was performed through a Snell's law experiment on a metamaterial designed to have a negative index of refraction at microwave frequencies [4]. The famous two-dimensional negative index material made by a group at the University of California San Diego is shown in ***Fig.3.3a***. The material consists of a two-dimensional array of repeated unit cells of copper wires and split ring resonators on interlocking strips of standard circuit board material. To determine the refractive index, they measured the deflection of a beam of microwave radiation as it passed through the prism-shaped sample. In this refraction experiment (in ***Fig.3.3b*** is shown the diagram of experimental setup), the prism-shaped samples were placed between two circular aluminum

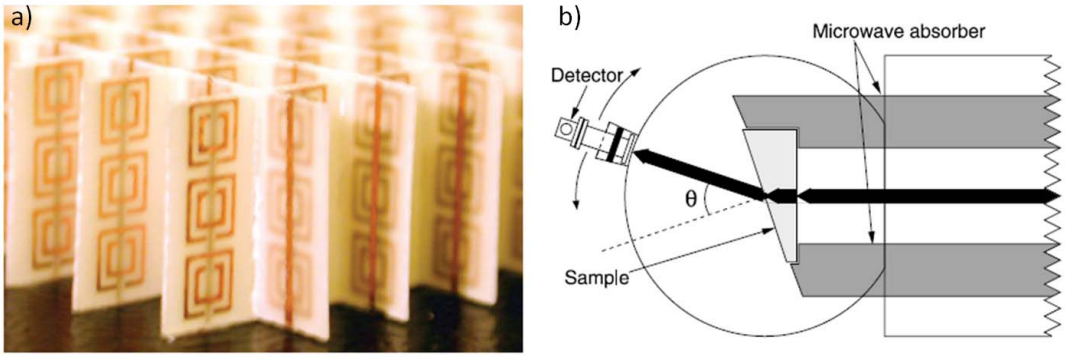

Figure 3.3: a) Photograph of the left-handed metamaterial sample. The sample consists of square copper split ring resonators and copper wire strips deposited on opposite sides lithographically on standard circuit board. The height of the structure is 1 cm. b) Diagram of experimental setup. The sample and the microwave absorber were placed between top and bottom parallel, circular aluminum plates spaced 1.2 cm apart. The radius of the circular plates was 15 cm. The black arrows represent the microwave beam as would be refracted by a positive index sample. The detector was rotated around the circumference of the circle in 1.5° steps, and the transmitted power spectrum was measured as a function of angle, from the interface normal. The detector was a waveguide to coaxial adapter attached to a standard X-band waveguide, whose opening was 2.3 cm in the plane of the circular plates. ϑ as shown is positive in this figure [4].

plates. The top plate had a pivot in the center, about which an attached X-band (from 8 to 12 GHz or from 2.5 to 3.7 cm) microwave waveguide could be rotated to measure transmitted power at arbitrary refraction angles. The incident face of the prism was illuminated with a beam of microwaves whose electric field was polarized such that it was uniform and perpendicular to the metal plates and parallel to the wires shown in ***Fig.3.3a*** (transverse magnetic polarization). Any refraction from the first surface would be caused by components of the incident beam containing angles of incidence away from the normal. The outcoming waves were guided by two flat sheets of aluminum whose spacing matched that of the circular plates (1.2 cm) and they were laterally confined by sheets of absorber placed 9.3 cm apart. After propagating through the sample, the microwave beam encounters the second surface of the prism, the refraction interface (which was at an angle of 18.43° with respect to the normal of the incident surface), and it is refracted into a direction determined by Snell's law. To measure the exit angle, the waveguide/power meter assembly has rotated in 1.5° steps and the transmitted power spectrum over the entire X-band range at each step has recorded. Experiments were performed with a prism-shaped left-handed metamaterial sample, as well as with a similarly shaped Teflon sample as a control. As can be seen in ***Fig.3.4***, at 10.5 GHz, the microwaves were refracted to positive angles as expected for the Teflon sample and to the opposite side (i.e., negative ϑ side) of the normal for the left-handed sample. The Teflon data show refraction as would be predicted for $n_{Teflon} = 1.4 \pm 0.1$, whereas for the left-handed metamaterial, the measured exit angle of ϑ_{air} =-61° implies that $n_{LHM} = -2.7 \pm 0.1$. Although the metamaterial consists of discrete scattering elements, it may be approximated as an effective medium for wavelengths that are larger than the unit cell size (the left-handed metamaterial used in these experiments had a unit cell dimension of 5 mm, a factor of 6 smaller than the X-band center wavelength of 3 cm) and the negative refractive index experimentally verified is the combining effect of the electrical response of the wires with negative effective permittivity $\varepsilon_{eff}(\omega)$ and the magnetic one of the split ring resonators with negative effective permeability $\mu_{eff}(\omega)$.

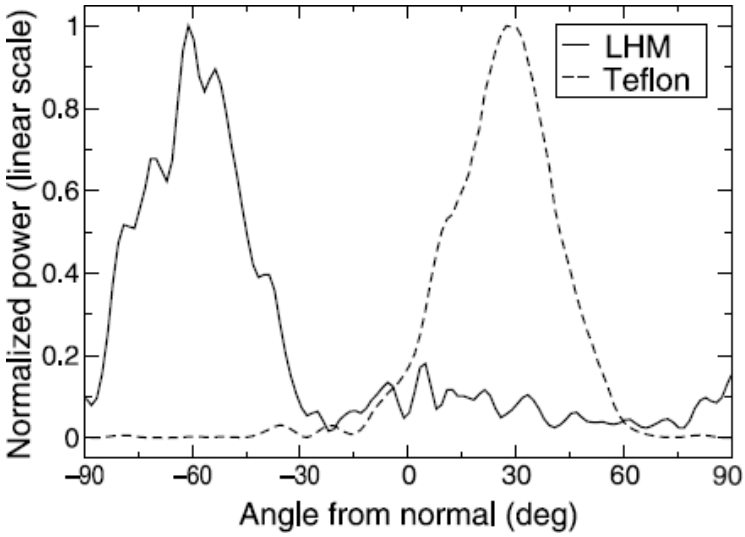

Figure 3.4: Transmitted power at 10.5 GHz as a function of refraction angle for both a Teflon sample (dashed curve) and a left-handed metamaterial sample (solid curve). The two curves were normalized such that the magnitude of both peaks is unity. For the Teflon sample, the refracted power peak was measured to be 27°, corresponding to a positive index of refraction of 1.4 ± 0.1. For the left-handed metamaterial sample, the peak was at -61°, from which we deduce the index of refraction to be -2.7 ± 0.1 [4].

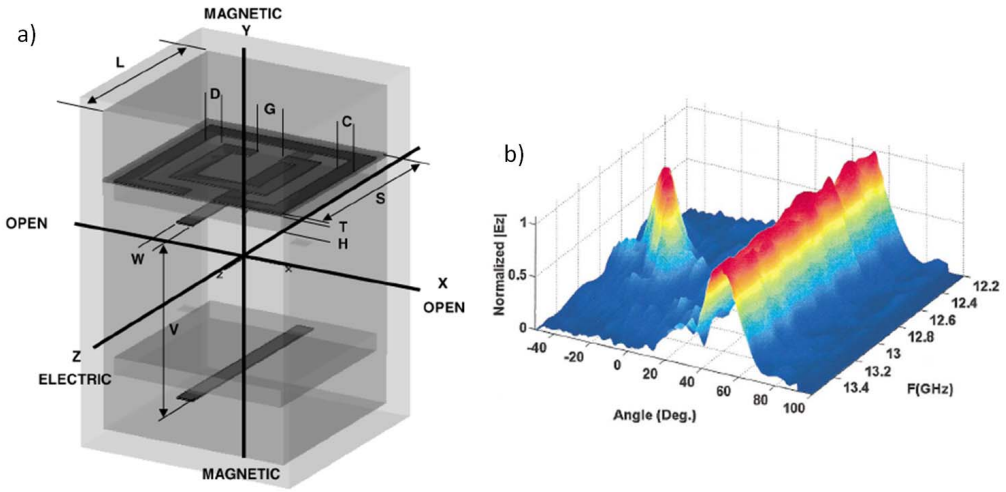

Figure 3.5: a) Unit cell of the 901 high wire density structure used in the numerical simulations. The direction of propagation of the electromagnetic field is along the x axis, the electric field is oriented along the z axis, and the magnetic field is along the y axis. b) Surface plot of measured transmissivity for the Teflon and 901 high wire density negative index material wedge. Note that the electric field refracted by the Teflon wedge peaks at a positive refractive angle of 48.2° (corresponding to an index of refraction of 1.4) and is independent of frequency. The electric field refracted by the negative index material wedge peaks at negative angles that are a function of the frequency. The two peaks are not normalized by the same factor. The non-normalized value of the peak electric field of the negative index material sample is about 20% of the Teflon peak [34].

Two years later, in 2003, Parazzoli et al. [34] used a similar structure to manufacture a three-dimensional cube (***Fig.3.5a***) operating in free space, and measurements confirming the negative index of refraction of the structure were performed at a distance much larger than the wavelength (***Fig.3.5b***).

Although the first obtained negative index material has electric permittivity and magnetic permeability simultaneously negative in the microwave range, scaling negative refraction up to the optical range is very important for both the theoretical significance and for the application value that such materials could provide. While the direct scale down of the experimentally verified systems is possible only to the

THz region, most of practical applications of these unique materials are in the optical and infrared part of the spectrum. The electromagnetic response of metals in the optical range is vastly different than at lower frequencies, where ε is extremely large and metals behave as nearly perfect conductors. This distinction prohibits the design of optical negative index materials using the same structures as their microwave counterparts. The challenges in optical negative index material research lay not only in design and fabrication, but also in experimental characterization. The fabrication limits concerns the sample thickness dimensions, which must be subwavelength and this limitation has prohibited experimentalists from directly observing the negative bending of a beam of light from a wedge-like structure, as was done in microwave negative index material experiments.

To achieve a negative index material, it is essential to tune the resonance property of the artificial material in such a way that the frequencies for the negative electric response and those for the negative magnetic response occur in an overlapping spectral range. As we have seen above, a possible approach to achieve a negative refractive index in a passive medium is to design a material where the permittivity $\varepsilon = \varepsilon' + i\varepsilon''$ and the permeability $\mu = \mu' + i\mu''$ satisfy the requirement: $\varepsilon'\mu'' + \varepsilon''\mu' < 0$. However, due to the natural inertness of magnetic permeability at optical frequencies, it is a practical challenge to obtain an effective permeability very different from 1, especially at very high frequencies such as the frequency of visible light. The above relation strictly implies that $n' < 0$ cannot occur in a magnetically inactive medium with $\mu = 1 + 0i$. Fortunately a negative index of refraction can be achieved in a magnetically lossy medium with a negative $\varepsilon' < 0$ along with $\mu'' > 0$. In this case the inequality may still be fulfilled, and therefore a negative real part of the refractive index n' can be obtained. The first optical metamaterial with a negative index of refraction was experimentally demonstrated in 2005 by a research group at Purdue University [35]. Both experiments and simulations on their metal-dielectric composite (a double-periodic array of pairs of parallel gold nanorods ***Fig.3.6a***), demonstrate that a negative refractive index $n' = -0.3$ is achieved at the optical wavelengths close to 1.5 µm ***Fig.3.6d***.

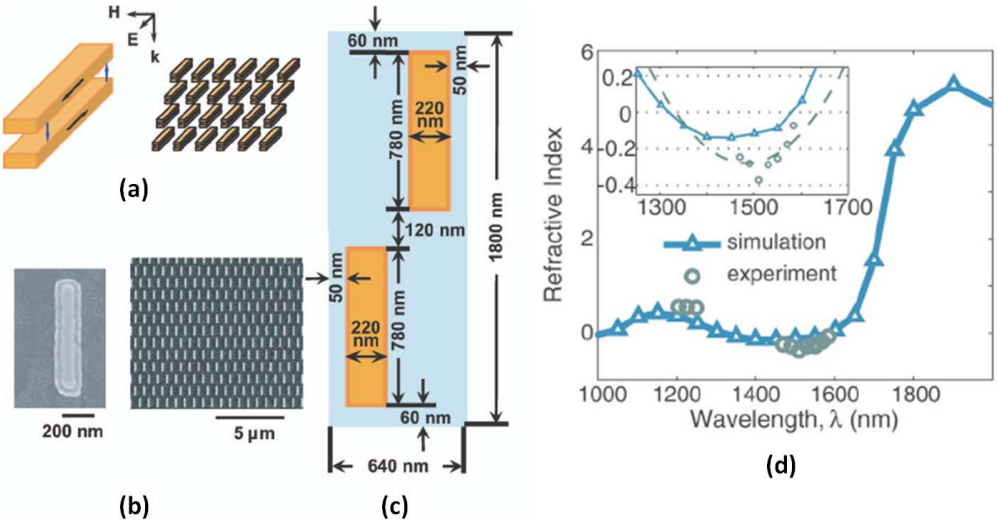

Figure 3.6: (a) Schematic for the array of nanorod pairs; normally incident light with the electric field polarized along the rods and the magnetic field perpendicular to the pair. (b) Field-emission scanning electron microscope images of a portion of the sample and a closer view of a single pair of nanorods. (c) Elementary cell of metal-dielectric composite, the fabrication procedure resulted in a trapezoidal shape of the rods, the dimensions of the bottom rods are 780 nm x 220 nm while the top rods are smaller 670 nm x 120 nm and each rods is sandwich structure, Ti(5 nm)/Au(50 nm)/Ti(5 nm)/SiO2(50 nm)/Ti(5 nm)/Au(50 nm). (d) Real part of the refractive index retrieved from simulations (triangles) and experiments (circles). The inset is a magnified view of the region of negative refraction; the dashed curve shows the quadratic least-squares fit for the experimental data [35].

3.1.1 Applications of negative refractive index: perfect lens

Materials with negative refractive index have attracted significant attention after Pendry predicted that neagtive refractive index material can act as a *superlens* allowing imaging resolution that is limited not by the wavelength but rather by material quality [5]. Negative refraction by a slab of material bends a ray of light back toward the axis and for this reason a planar slab of negative refractive index material with sufficient thickness can act as a lens, because it has a focusing effect at the point where the refracted rays meet the axis. As depicted in ***Fig.3.7c***, light rays coming from an object are negatively refracted at the incident surface of the negative index slab, and the negative refraction of rays is repeated again at the second boundary. Consequently, the negative refractive index slab creates an image within the slab and a second non-inverted image in the free space after the output interface. Compared to a conventional convex lens (***Fig.3.7a,b***), the negative refractive index lens works in a different way, it does not have any axis or curvature, nor does it focus parallel rays or magnify small objects. All of these features were pointed out by Veselago [3]. The exotic properties of such a slab lens were first analyzed by Pendry, who recognized that a slab with refractive index $n = -1$ exhibits an entirely new type of focusing phenomenon: if it is placed in vacuum it allows the imaging of objects with sub-wavelength precision [36].

A conventional lens with the best possible resolution requires a wide aperture. Each ray emanating from an object, as shown in ***Fig.3.7a***, has wave vector components along the axis of the lens, $k_z = k_0 \cos\vartheta$, and perpendicular to the axis, $k_x = k_0 \sin\vartheta$, where k_0 is the wavenumber and ϑ is the angle of the ray with respect to the axis. The axial projection k_z is responsible for transporting the light from object to image; k_x represents a Fourier component of the image. Due to the Abbe diffraction limit, conventional lens based on positive-index material with curved surface are not able to resolve objects smaller than approximatively half of illuminating wavelength. The best k_x that can be achieved is $k_x = k_0$, and hence the resolution limit is $\Delta \approx \pi/k_0 = \lambda/2$ where λ[1] is the wavelength. Therefore,

[1]More precise analysis shows that the diffraction limit or Abbe's limit for a conventional lens is

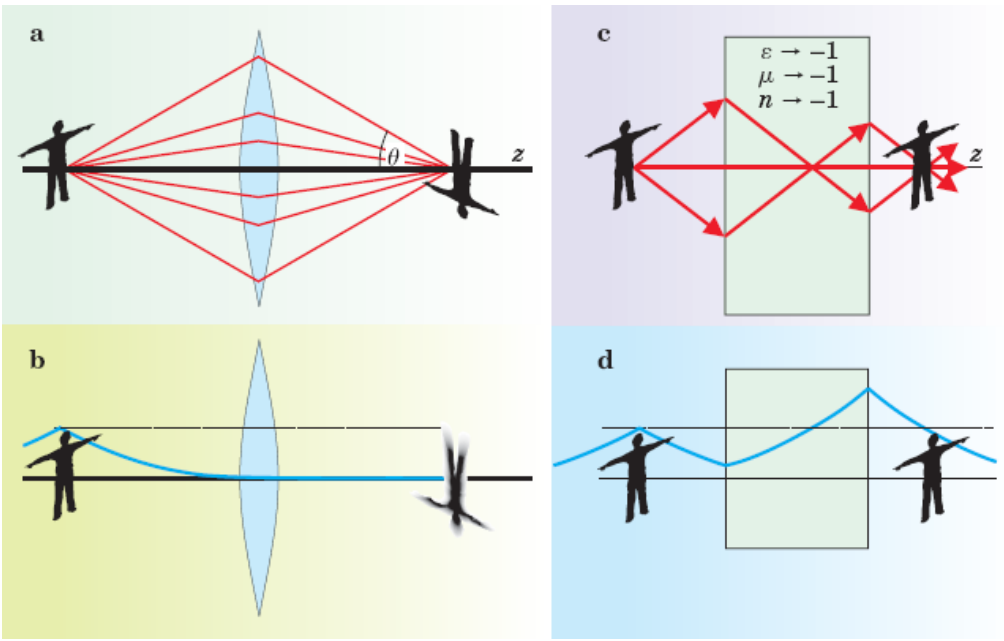

Figure 3.7: The limitation of conventional lens and the idea of the negative refractive index slab lens. a) a conventional lens only collects the propagating waves and for good resolution it needs a wide aperture to refract rays at large angles ϑ, but even so, they are limited in resolution by the wavelength used; b) the loss of the evanescent waves in conventional imaging system, the missing Fourier components of the image are contained in the near field, which decays exponentially (blue curve) and makes negligible contribution to the image; c) the focusing ability of a negative refractive index slab; d) the growth of evanescent waves in the negative refractive index slab and the restoration of both the propagating and evanescent waves. Such a negative lens thus removes the wavelength limitation. However, the resonant nature of the amplification places severe demands on materials, in particular they must be very low loss [36].

conventional imaging systems cannot provide sub-wavelenght resolution and this restriction is a huge problem in many areas of optics. In contrast to the image, the object has no limit to its electromagnetic details, but unfortunately not all of that information makes it across the lens to the image. The problem lies with the wave vector's z-component, which we can write as $k_z = \sqrt{k_0^2 - k_x^2}$. Evidently, for large values of k_x, corresponding to fine details in the object, k_z is imaginary and the waves decay exponentially as $e^{-n\sqrt{k_x^2 - k_0^2}z}$, as shown in ***Fig.3.7b***. Such waves, usually called *evanescent wave* are confined to the vicinity of the object and do not have any contribution to the image obtained by standard lenses. For that reason, they are commonly referred to as the "near field" and the propagating rays as the "far field". In order to beat the diffraction limit and obtain images with subwavelength features, it needs to be able to collect the evanescent waves before they fade away. If we could amplify the near fields, we could in principle recoup their contribution and a planar slab of negative material achieves this feature. ***Fig.3.7c*** shows rays contributing to the image formed by a negative slab. Just as for a conventional lens, the rays only contribute to details greater than about half a wavelength in diameter. In contrast, the behavior of the near field is remarkably different, ***Fig.3.7d***. The negative medium thus amplifies the wave and compensates for the decay that occurred in an equal thickness of vacuum. It is important to note that the amplification of evanescent waves in negative index material does not violate energy conservation, because evanescent waves carry no energy. In an ideal, lossless negative index refraction slab, the Poynting vector of evanescent waves is zero, so no energy transport is involved during the growth of evanescent modes in such slabs. Nevertheless, the conditions for the *perfect lens* are rather severe, and the far-field *perfect lens* may only have theoretical significance. Rigorous analysis shows that any realistic losses that are inevitable in today's resonance-based designs of negative refractive index materials can eliminate the desired effect of flawless imaging. Podolskiy et al. show that the resolution of a left handed material based lens is strongly suppressed even

$\lambda/(2n\sin\alpha)$ where n is the refractive index of the medium in which the imaging system is immersed, and α represents the semi-aperture angle of the lens.

for small absorption, which is inevitable in all modern resonance-based negative refractive index material designs [37]. It was recently shown that in lossless media any deviation of ε from -1 strongly suppresses the super-resolution (super-resolution is defined as resolution beyond the conventional diffraction limit for far-field imaging [38]). However, also the lossless medium itself represents the ideal case, which can never be realized. The presence of any nonzero absorption (described by positive imaginary parts of dielectric permittivity ε'' and magnetic permeability μ'') leads to strong suppression of transmitted waves with large k_x. All the negative refractive index materials based on resonance properties of plasmonic metamaterials are highly dissipative, anisotropic, and lossy. That is the major reason why so far there has been no far-field demonstration of super-resolution using a planar negative refractive index slab.

3.2 Hyperbolic or indefinite medium

The double-resonance scheme discussed above represent the standard approach for realizing negative refractive index metamaterials, but the simultaneous tuning of electrical and magnetic resonances causes large resonance losses and technical difficulties in design and fabrication. An alternative way to obtain negative refraction is a *nonmagnetic* and *nonresonant* approach based on exploiting the properties of strongly anisotropic dielectric materials. Instead of engineering subwavelength units with desired ε and μ values, the starting point for anisotropy based negative refraction is the exploration of the possible relationships between the wavevector $\boldsymbol{k}$ and the Poynting vector $\boldsymbol{S}$ in nonmagnetic, homogenous media.

We consider a planar interface, parallel to the xy plane of coordinate system, with the boundarie at $z = 0$, which separate the air on the left from a material on the right. The medium is nonmagnetic ($\mu = 1$) and has an anisotropic uniaxial dielectric response described by the dielectric tensor ε, with $\varepsilon_x = \varepsilon_y = \varepsilon_{||}$ (parallel to the separation interface) and $\varepsilon_z = \varepsilon_{\perp}$ (perpendicular to the separation interface), so the optical axis is along the z direction. Similarly to uniaxial crystals, the sys-

tem may support the propagation of two different kinds of electromagnetic waves (§Appendix A). The waves of the first kind have their electric field vector in the xy plane. The propagation of such waves depends only on $\varepsilon_{||}$, and is not affected by medium anisotropy. These waves are also known as *ordinary waves*. The waves of the second kind (known as *extraordinary waves*) have their electric field in the xz plane. Correspondingly their electromagnetic properties are affected by both $\varepsilon_{||}$ and $\varepsilon_{\perp}$. The ordinary and extraordinary waves are fundamentally distinct as they have different dispersion relations[2] and refraction properties. It is possible to characterized the extraordinary wave in a uniaxial crystal by the dispersion relation (A.8)

$$\frac{k_x^2}{\varepsilon_{\perp}} + \frac{k_y^2}{\varepsilon_{\perp}} + \frac{k_z^2}{\varepsilon_{||}} = k_0^2 \tag{3.1}$$

and the isofrequency surface can be used to understand one key consequence of material anisotropy: the deviation of the Poynting vector $\boldsymbol{S}$ from the direction of the wave vector $\boldsymbol{k}$ [39]. The direction of the Poynting vector is identical to the direction of the group velocity vector $\boldsymbol{v}_g = \boldsymbol{\nabla}_{\boldsymbol{k}}\omega(\boldsymbol{k})$, this implies that $\boldsymbol{S}$ is normal to the isofrequency surfaces given by (3.1). Assuming that the light propagates within the xz plane, the wavevector $\boldsymbol{k}$ is represented by a vector from the origin of the plane $k_x k_z$ to a given point on the isofrequency curve, and the angle of the Poynting vector $\boldsymbol{S}$ is normal to the tangent of the curve at the point. In an anisotropic medium the wave vector curve become ellipsoidal and the angle between $\boldsymbol{k}$ and $\boldsymbol{S}$ is non-zero ***Fig.3.8b*** (the isotropic case is the limit anisotropic case with $\varepsilon_x = \varepsilon_z$, the wave vector curve is circular and the vectors $\boldsymbol{k}$ and $\boldsymbol{S}$ are collinear ***Fig.3.8a***). Finally, for a material with dielectric permittivity ε_x and ε_z opposite in sign the dispersion relation becomes hyperbolic (***Fig.3.8c,d***). The materials whose the permittivity tensor elements considered along the principal axis are not the same sign are known as *hyperbolic* or *indefinite medium* [40]. In particular for a material with negative transverse dielectric permittivity $\varepsilon_x < 0$ and positive in-plane permittivity $\varepsilon_z > 0$ the curvature of the hyperbola is such that the signs of $\boldsymbol{k}_z$ and $\boldsymbol{S}_z$ are opposite,

[2]For the ordinary waves the dispersion relation is $k_x^2 + k_y^2 + k_z^2 = k_0^2\varepsilon_{||}$, for the extraordinary waves the dispersion relation is $(k_x^2 + k_y^2)/\varepsilon_{\perp} + k_z^2/\varepsilon_{||} = k_0^2$ (§Appendix A).

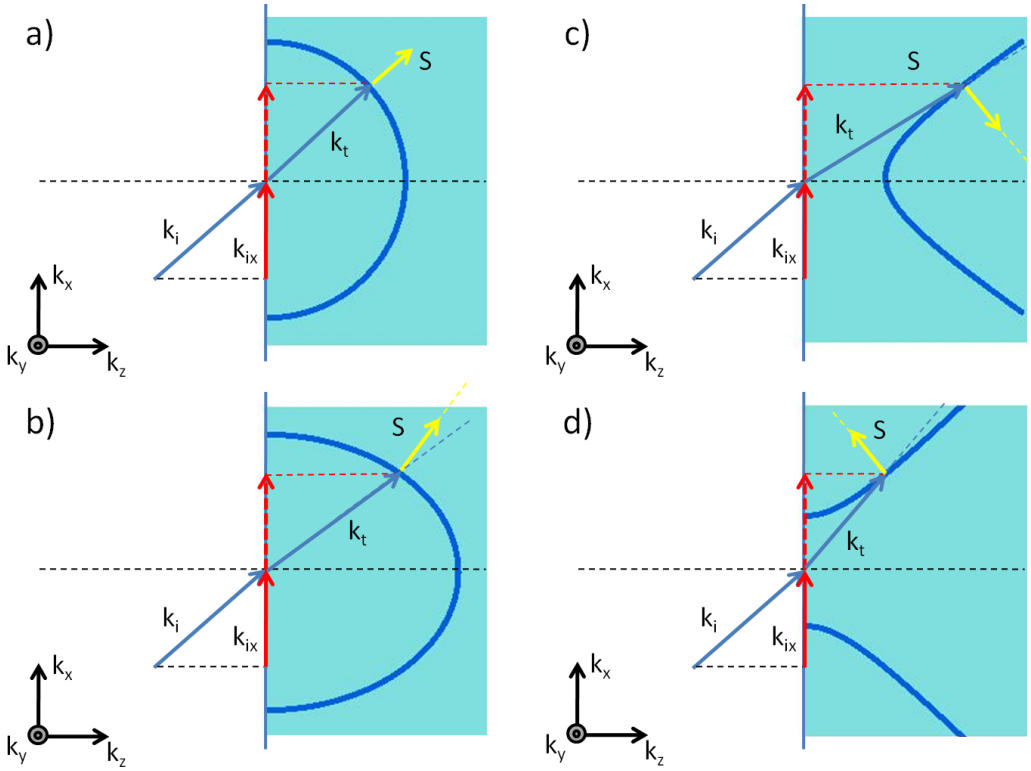

Figure 3.8: Tangential wave vector component conservation for a transverse magnetic wave propagation in a) an isotropic crystal with $\varepsilon_x = \varepsilon_z$; b) in an anisotropic crystal with $\varepsilon_x > \varepsilon_z$; c) in a hyperbolic crystal width $\varepsilon_x > 0$ and $\varepsilon_z < 0$ [12]; d) in a hyperbolic crystal width $\varepsilon_x < 0$ and $\varepsilon_z > 0$ [39].

as shown in ***Fig.3.8d***. This opposite directionality between $\boldsymbol{k}_z$ and $\boldsymbol{S}_z$ leads to a negative effective index of refraction.

Most of all indefinite media are artificially engineered metamaterials, which require fine fabrication technology to produce structures with strong anisotropy. The condition of extreme anisotropy, where the principal permittivities have different signs, can be attained by resorting to suitable metal-dielectric nano-composites with a geometrical structure exhibiting at least one privileged direction. Exploiting the effective medium approach, it is possible to design the composite to show indefinite permittivity in a spectral range whose wavelengths are much greater than the nano-constituents size. Two relevant examples of such structured media are nanowire composites [13, 14, 41] (typically silver nanowires embedded in an allumina membrane) and layered media [7, 10, 42, 43] (obtained by alternating metal and dielectric

layers) whose privileged directions are, evidently, the nanowire and the stacking direction, respectively. Recently, it has been proposed that indefinite permittivity can even be observed in anisotropic natural materials as, for example, graphite [44] and strong anisotropic uniaxial crystals of α-Al_2O_3 [45] which are shown to be indefinite in the ultraviolet (due to the hybrid electronic transitions) and the infrared region (due to the strong anisotropy of polar lattice vibrations), respectively.

In their work [44], Sun et al. report the experimental verification of an all angle negative refraction in the deep-ultraviolet frequency region in monocrystalline graphite. Graphite is a semimetal with a uniaxial-layered crystalline structure, which allows for extremely strong anisotropy between the directions perpendicular and parallel to the atomic plane. The dielectric tensor are characterized by two independent dielectric functions, including the ordinary dielectric function $\varepsilon_o(\omega)$, which describes light polarized along the carbon-layer planes, and the extraordinary dielectric function $\varepsilon_e(\omega)$, which describes light polarized perpendicular to the carbon-layer planes. The ε_o and ε_e spectra in the range of 240-400 nm obtained by a spectroscopic ellipsometer (J. A. Woollam) are shown in ***Fig.3.9b***. In the ultraviolet region below 282 nm, the real parts of ε_o is negative, whereas the real part of ε_e is positive, providing the indefinite permittivity of graphite. As illustrated in ***Fig.3.10a***, if the crystal is oriented with its optic axis parallel to the sample surface and perpendicular to the plane of incidence, the TM incident light, with magnetic field polarized in the atomic plane of the graphite, can be treated as ordinary light. In this case, the permittivity of the material is isotropic for the electric-field and according to Maxwell's equations, the dispersion relationship for TM waves is given by $k_x^2/\varepsilon_e + k_y^2/\varepsilon_e = k_0^2$. If the crystal is oriented as shown in ***Fig.3.10d***, the optic axis is parallel to both the sample surface and the plane of incidence, the incident light is extraordinary light and is modulated by the anisotropic dielectric constants of the crystal. The dispersion relation can then write as $k_x^2/\varepsilon_e + k_y^2/\varepsilon_o = k_0^2$. As shown in ***Fig.3.10b,e*** through experimental ellissometry results and in ***Fig.3.10c,f*** by a schematic illustration of isofrequency curves, in the first case incident wave experiences a normal refraction, while in the second one an uniaxial anisotropic material

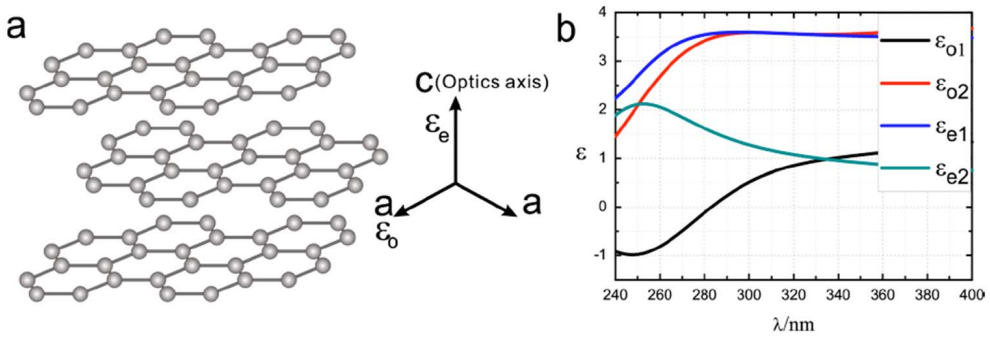

Figure 3.9: a) The atomic structure of graphite, where the c-axis (optical axis) is perpendicular to the carbon-layer planes. b) The spectral dependence of the real ε_{o1} and ε_{e1} and imaginary ε_{o2} and ε_{e2} parts of the dielectric constants for different orientations in monocrystalline graphite sample [44].

with $\varepsilon_e > 0$ and $\varepsilon_o < 0$ exhibit negative refractive behavior for a transverse magnetic wave propagating along the x-axis for all incident angles. The indefinite permittivity is attributed to extremely strong anisotropy in the crystal structure and the hybrid electronic transitions.

Wang et al. propose a kind of indefinite media at infrared frequency without artificial structures [45]. As an example, the dielectric dispersions of α-Al_2O_3 single crystal with different polarizations of electric field are measured, the regions of indefinite permittivity are demonstrated. Natural existing indefinite properties of the media are based on strong anisotropy in polar lattice vibrations in different directions, parallel or perpendicular to the crystal axis. According to the classical theory of lattice dynamics, the relative permittivity of polar crystals will exhibit one or more dielectric resonances near the transverse optical frequencies due to the excitation of transverse optical phonons. For a more complicated crystal structure, the dielectric dispersion is modeled by the sum of independent damped harmonic oscillators as follows

$$\varepsilon(\omega) = \varepsilon_\infty + \sum_i \frac{\Delta\varepsilon_i \omega_{Ti}^2}{\omega_{Ti}^2 - \omega^2 + i\gamma_i \omega_{Ti} \omega},$$

where ε_∞ is the highfrequency permittivity and ω_{Ti}, $\Delta\varepsilon_i$ and γ_i are the oscillator parameters, i.e. frequency, oscillator strength and damping coefficient of the ith

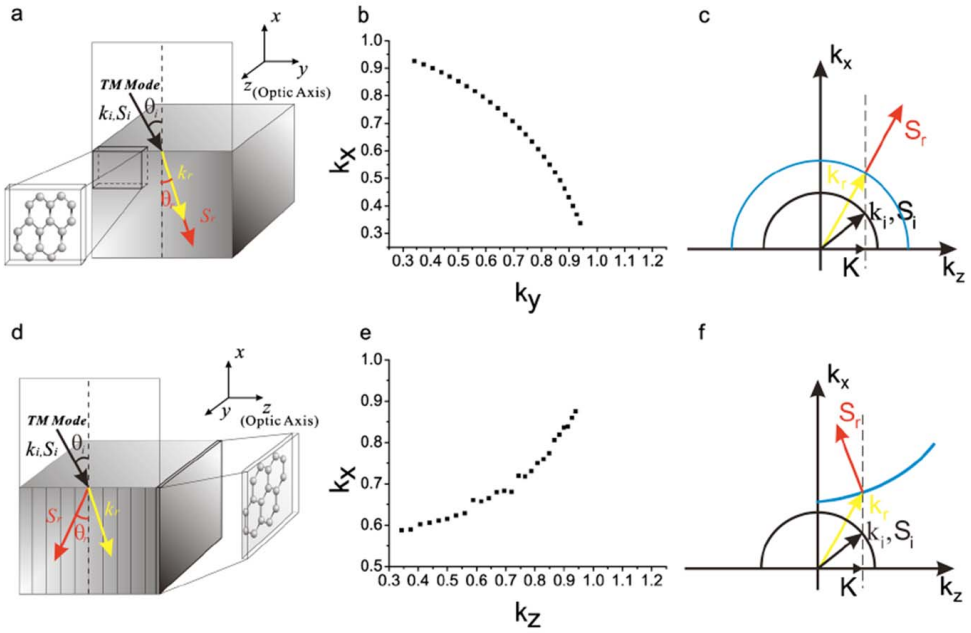

Figure 3.10: The orientation of single crystalline graphite and the scheme of refraction as it occurs in graphite. The direction perpendicular to the carbon atomic plane is the optic axis z-axis. a) The single crystal of graphite is oriented such that the optic axis is parallel to the sample surface and is also perpendicular to the plane of incidence. A TM mode wave, with magnetic field polarized in the atomic plane of the graphite, is incident on the sample with an incident angle of ϑ_i and then refracted at an angle of ϑ_r. b) The dispersion isofrequency curves mapped using ellipsometry at this orientation. c) Schematic illustration of the normal refraction of ordinary light at the interface between the free space (circular black curve) and the uniaxial media (circular blue curve). The refracted wave vector $\boldsymbol{k}_r$ and Poynting vector $\boldsymbol{S}_r$ is determined by Maxwell's equations. d) The single crystal of graphite is oriented such that the optic axis is in the plane of the sample surface and in the plane of incidence. e) The dispersion isofrequency curves mapped using ellipsometry at this orientation. f) The negative refraction of extraordinary light at the interface between the free space (circular black curve) and the uniaxial media (hyperbolic blue curve) [44].

transverse vibration mode. When the crystal structure presents an uniaxial symmetry such as tetragonal or hexagonal system, the permittivity of the crystal will be a form of tensor with two independent parts, one is corresponding to the electric field $\boldsymbol{E}$ parallel to the optical axis c and the other is perpendicular to the c axis. Because of the parameters of the lattice are different in the two directions, the lattice vibration frequencies for the same vibration mode are different. In this case there will be several regions in which the crystal exhibits dielectric tensor with contrary sign parts, resulting in an indefinite permittivity with a strong anisotropy. They take α-Al_2O_3 single crystal as an example, retrieve the permittivity of the crystal and show an all-angle negative refraction at infrared frequency. Using the oscillator model and the relationship between the permittivity and the reflectivity R for normal incidence $R = |[\sqrt{\varepsilon(\omega)} - 1]/[\sqrt{\varepsilon(\omega)} + 1]|^2$ when considering the crystals are nonmagnetic ($\mu = 1$), they can get the fitted reflectivity and the retrieved relative permittivity. The measured and fitted polarized reflectivity spectra are shown in ***Fig.3.11*** (left) and the oscillator parameters are listed in each figure accordingly. Using the fitted oscillator parameters, the two component $\varepsilon_{||}$ and $\varepsilon_{\perp}$ of the permittivity can be deduced and the results are presented in ***Fig.3.11*** (right). The spectral intervals, where the crystal exhibits contrary signs between $\varepsilon_{||}$ and $\varepsilon_{\perp}$, are indicated by the shaded regions. In the frequency regions 400-440 cm^{-1} and 480-515 cm^{-1}, $\varepsilon_{||} < 0 < \varepsilon_{\perp}$, while in the frequency regions 565-580 cm^{-1} and 885-910 cm^{-1}, $\varepsilon_{\perp} < 0 < \varepsilon_{||}$.

3.2.1 Applications of hyperbolic media

Within the rapidly growing field of metamaterials, hyperbolic or indefinite or extremely anisotropic metamaterials characterized by principal permittivities having different signs, are attracting a considerable research interest mainly for the novel potentialities they provide for achieving efficient optical steering and manipulation. The hyperbolic dispersion relation characterizing extraordinary plane waves through indefinite or hyperbolic media is the main physical ingredient leading to unusual optical effects. In 2001, for the first time, Lindell et al. [46] have shown

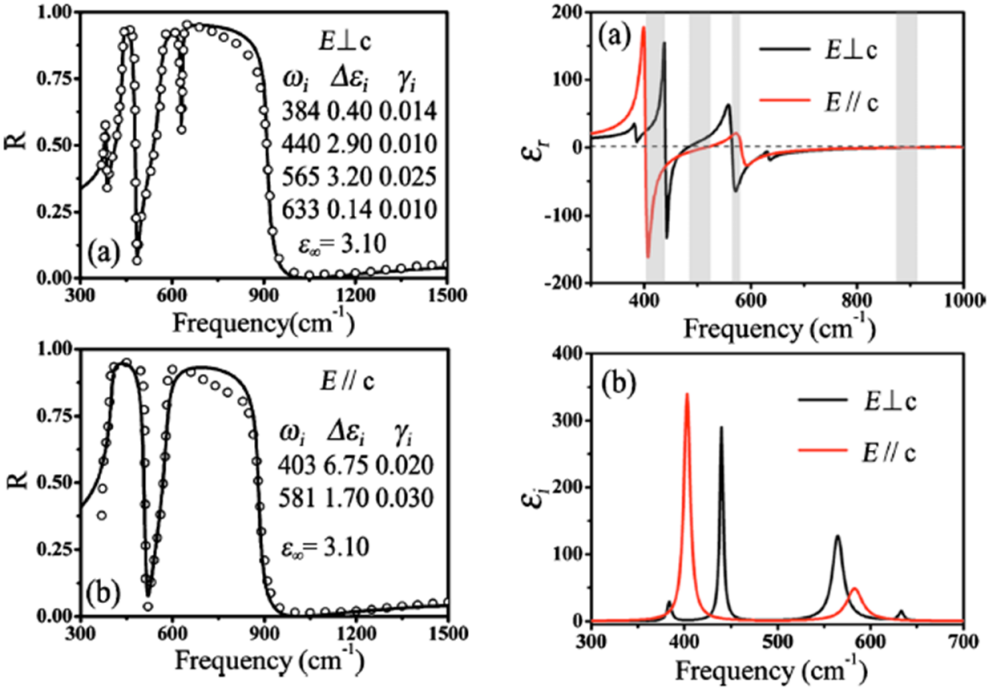

Figure 3.11: Left: Reflectivity of α-Al_2O_3 single crystal for a) $\boldsymbol{E} \perp c$ axis and b) $\boldsymbol{E}||c$ axis. The points are the experimental values and the lines are calculated from the oscillator model. Right: Dielectric dispersion curves of α-Al_2O_3 single crystal a) real part; b) imaginary part retrieved from the fitted reflectivity [45].

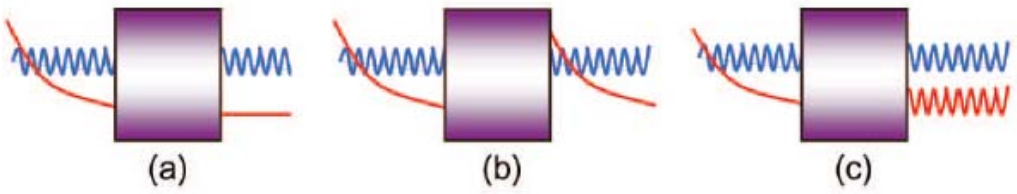

Figure 3.12: a) A conventional imaging system transforms propagating waves, but does not operate on the decaying evanescent waves; these waves can only be detected in the near field. b) *Superlens* amplifies the evanescent waves but does not change their decaying character. c) An ideal device would convert evanescent waves to propagating waves for ease of detection and processing; these waves should not mix with the propagating waves emanating from the object.

that the property of negative refraction is not confined to materials with negative definite ε and μ tensors, but can be expected to occur in certain classes of uniaxially anisotropic media which is due to the fact that the hyperbola curvature is opposite to that of the circumference of standard media. The ability of such media of converting vacuum evanescent waves into homogeneous propagating waves [47] (as a consequence of the lack of evanescent waves along the hyperbola major axis) allows developing the idea of *hyperlens* [11, 48, 49, 50].

Resolution of conventional optics is generally constrained by the diffraction limit, which prevents imaging of subwavelength features. Such fine details are encoded in rapid spatial variations of electromagnetic fields at the object's surface. However, these fields decay exponentially with distance and are thus only detectable in the near field (***Fig.3.12a***). Outside the near field, the loss of high spatial frequency information carried by the decaying evanescent waves precludes reconstructing the image of an object with resolution better than approximately $\lambda/2$. It is highly desirable for many applications (e.g. biological microscopy) to use a system which would produce a direct optical far field image that includes subwavelength features. It is for this reason that the recently proposed *superlens* [5], a device capable of subwavelength resolution that relies on materials with negative index of refraction, received much attention. The originally proposed superlens would not only focus the propa-

gating waves, but would also amplify the evanescent waves in such a way that both the propagating and evanescent fields would contribute to an image in the far field, resulting in resolution far below the diffraction limit (***Fig.3.12b***). However, subsequent studies demonstrated that due to the resonant nature of the enhancement of evanescent waves the subwavelength resolving power of most superlens implementations is severely curtailed by material losses [37]. Furthermore, although a superlens amplifies evanescent modes and thus in principle enables their detection, the evanescent waves cannot be processed or brought to focus by conventional optics. An ideal imaging device would avoid this problem: it would not only capture evanescent fields to retrieve subwavelength information, but would also allow for their processing with standard optical components. This could be accomplished by transferring the information carried by evanescent fields into a portion of the propagating spectrum (***Fig.3.12c***). Following the conversion, these propagating waves would be detected and processed in the far field by methods similar to those of conventional imaging. Lee et al. [48] describe an experimental realization of a new sub-diffraction-limit imaging method called *hyperlens imaging*. They experimentally demonstrate 150 nm [51] and 130 nm [48] resolution (which is beyond the diffraction limit) using a magnifying optical hyperlens consisting of a curved periodic stack of Ag (35 nm) and Al_2O_3 (35 nm) deposited on a half-cylindrical cavity fabricated on a quartz substrate (***Fig.3.13a***). The dispersion of electromagnetic wave in cylindrical coordinates is represented by

$$\frac{k_r^2}{\varepsilon_\vartheta} + \frac{k_\vartheta^2}{\varepsilon_r} = k_0^2 \,,$$

where k_r and k_ϑ are wavevectors, ε_r and ε_ϑ are permittivities in radial and tangential direction respectively. ***Fig.3.13b*** shows isofrequency contours in k-space in which isotropic medium has circular dispersion (red). The accessible range of k_ϑ, which determines the imaging resolution, is limited to the radius of the circle, $r = \sqrt{\varepsilon} = n$, where n is the refractive index[3]. However, it was shown that a material with anisotropic electrical responses in two orthogonal tensor components can

[3]Higher index materials are used in immersion microscopy for this reason, but there's limited availability in nature, commonly used immersion oil gives n only around 1.5.

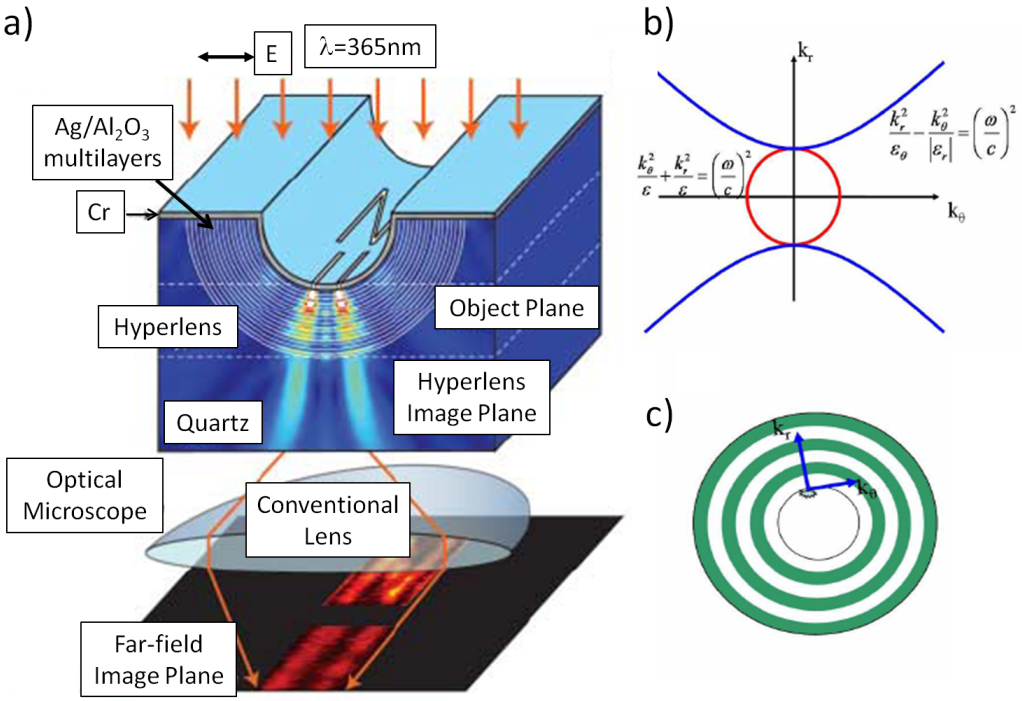

Figure 3.13: Magnifying optical hyperlens. a) Schematic of hyperlens and numerical simulation of imaging of sub-diffraction-limited objects [51]. b) Red circle: dispersion isofrequency curve of light in isotropic medium in cylindrical coordinate. Blue curve: hyperbolic dispersion in an anisotropic medium when $\varepsilon_r < 0$ and $\varepsilon_\vartheta > 0$. (b) One suggested cylindrical hyperlens structure. Multi-concentric layers of alternating metal and dielectric layers make anisotropic metamaterial [48].

indeed support the propagation of electromagnetic waves with large wave vectors. In particular, if $\varepsilon_r < 0$ and $\varepsilon_\vartheta > 0$, hyperbolic isofrequency contour is achieved (blue) and waves with larger k_ϑ that are commonly evanescent become propagating. Such a medium can be realized using the metamaterial concept. ***Fig.3.13c*** shows one exampled structure which consists of thin alternating layers of a metal and a dielectric. When a small object is placed at the center of such a *cylindrical hyperlens*, the object scatters the light and generates a wide band of k_ϑ. The fine feature information of an object is then brought to far field magnified which can be imaged directly by conventional optics.

For the experiment, Silver Ag ($\varepsilon_m = 2.4012 + 0.2488i$) and Aluminum Oxide Al_2O_3 ($\varepsilon_d = 3.217$) were used and the effective permittivity (2.17) of the designed

metamaterial was calculated using

$$\varepsilon_\vartheta = f\varepsilon_m + (1-f)\varepsilon_d\,, \qquad \varepsilon_r = \frac{\varepsilon_m\varepsilon_d}{(1-f)\varepsilon_m + f\varepsilon_d}\,,$$

where f is the filling ratio of the metal. At 365 nm working wavelength with $f = 0.5$, hyperbolic dispersion is obtained. The fabrication process of the hyperlens is shown in ***Fig.3.14a***. A thin Cr layer (150 nm) was deposited on a quartz wafer (150 µm thick). Then, a 50 nm wide etch slit was made and the half-cylindrical groove was defined through isotropic wet etching of quartz. A diameter of approximately 1.6 µm was achieved. Since multiple Ag and Al_2O_3 thin films were to be deposited. Than Cr layer was removed. Starting from the Ag layer, Al_2O_3 and Ag films were deposited alternatively, the thickness of each layer was set to 35 nm and a 50 nm of Cr film was deposited on top of the 16th layer (Al_2O_3). ***Fig.3.14b*** shows the schematic of our hyperlens imaging setup. The object was illuminated by a mercury lamp with a band pass filter centered at wavelength of 365 nm and bandwidth of 10 nm. ***Fig.3.14c*** is a top-view scanning electron microscope (SEM) picture of a line pair object with center-to-center distance of 130 nm and line width of 50 nm. They were placed off the center to show that an object can be placed anywhere in the groove to be imaged with good resolution and negligible position-dependant distortions. The smallest distance (Δ) that can be resolved by the transmission mode imaging setup is estimated to be about 260 nm from a simple equation: $\Delta = \lambda/NA$ where, $\lambda = 365$ nm, and numerical aperture $NA = 1.4$. Nevertheless, the 130 nm distance object is clearly resolved through the hyperlens as shown in ***Fig.3.14d***. The center-to-center distance of the enlarged image is about 300 nm which represents the magnification of the hyperlens.

Extreme anisotropy also fundamentally affects the excitation of waves, impinging from vacuum, into an indefinite medium to the point that, by suitably changing the mutual geometric orientation between the hyperbola and the metamaterial interface, novel interesting effects as cancellation of reflection and transmission can be predicted [52]. Consequently, optical devices exploiting indefinite media have been proposed as, for instance, polarization beam splitters [53] and angular filters [54] which are based on the fact that transverse magnetic and transverse electric waves

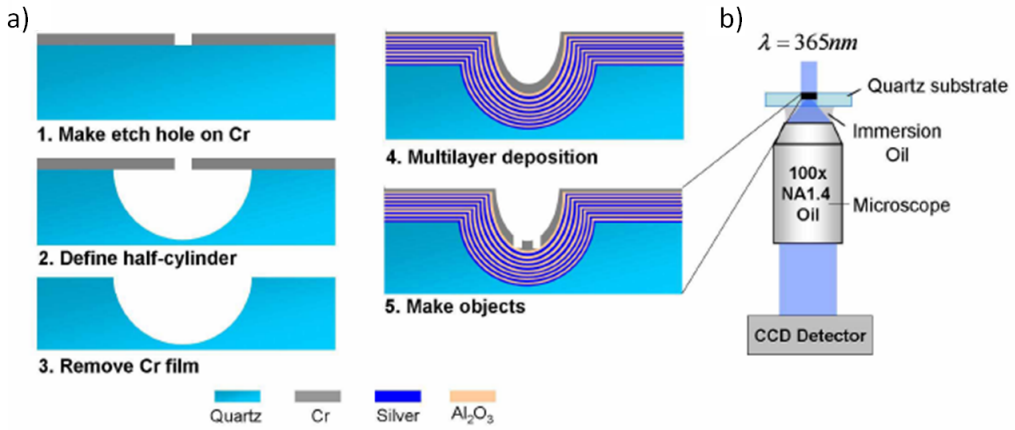

Figure 3.14: (a) Hyperlens sample fabrication process flow. Through the etch hole on a Cr film (1), isotropic wet etching makes cylindrical groove in quartz (2). After Cr film is removed (3), multilayer hyperlens structure is fabricated using alternate deposition of Ag and Al_2O_3 (4). A Cr film caps the hyperlens structure for object fabrication (5). (b) Imaging setup. Completed hyperlens/object sample is placed under objective with incident light at 365 nm, conventional far field microscope with 100X oil immersion objective and UV sensitive CCD detector was used for direct far field imaging [48].

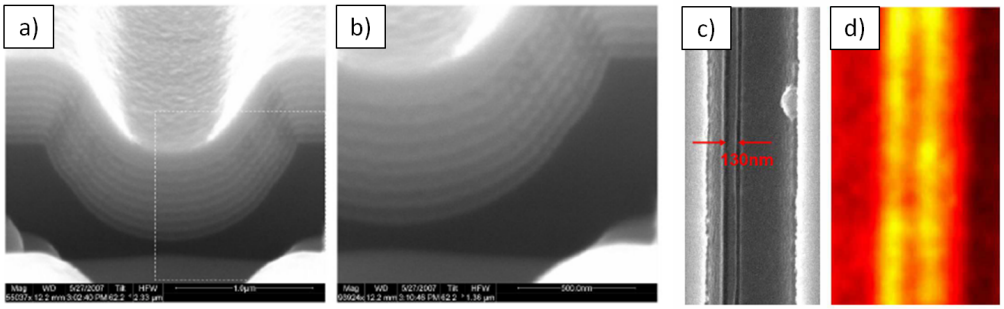

Figure 3.15: a) A SEM picture of the cross section of a hyperlens structure. 16 Ag/Al_2O_3 layers are clearly shown, bright and dark layers are Ag and Al_2O_3 respectively. The top thick and bright layer is Chromium. b) Zoom-in picture of white square in (a). c) Hyeperlens imaging results. SEM image of 130 nm line pair object on Cr film. Dark region is the hyperlens and the bright region is the flat surface. d) Image captured by optical microscope through hyperlensing shows 130 nm gap is clearly resolved [48].

are characterized by different dispersive features (hyperbolic and standard behavior, respectively).

3.3 Epsilon-near-zero metamaterial

The advent of metamaterials and the flexibility in choosing the value of the permittivity or permeability opened many new possibilities in different fields of physics and engineering. Besides the much celebrated realization of a double negative medium [2] and related prospective applications [5], materials with effective ε and effective μ or effective refraction index near zero have also become the subject of investigation. Such materials may be found naturally at infrared and optical frequencies, when noble metals, some semiconductors, or plasmonic and polar dielectrics such as SiC are near their plasma frequency. Also, ε-near-zero materials may be properly synthesized as metamaterials with a very small real part of the dielectric permittivity at the desired frequency, by embedding suitable inclusions in a host medium [55]. Their unique properties enable exotic light behavior and they can enhance linear or nonlinear properties of the metamaterial at ϵ-near-zero frequency.

For the linear optical properties of this metamaterial class, Alekseyev et al [54] have predicted that a highly anisotropic uniaxial ε-near-zero metamaterial, in which real part of electric permittivity along the optical axis is equal to zero, behaves in a dramatic different way when p- or s-polarized light interacts with this material. The analysis of transmission of p- and s-polarized light through a slab of such material demonstrate that this difference may lead to a unique class of highly selective angular filter and polarizer. The theoretical prediction have been confirmed experimentally in an array of silver nanowires grown in an anodic alumina membrane (***Fig.3.16***), which exhibits vastly different transmission characteristics for the two polarizations. Using Maxwell-Garnett approximation (2.29) and (2.30) it is possible to evaluate dielectric tensor for an array of cylindrical silver nanorods in alumina matrix, in particular with 8.25% volume filling fraction of silver inclusion and using pubished

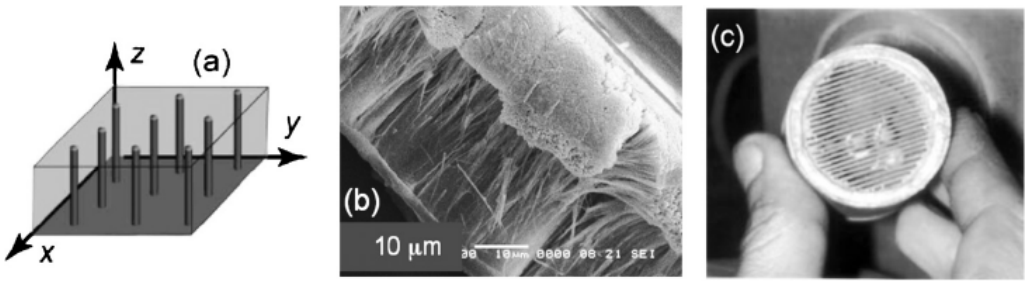

Figure 3.16: (a) Schematic of an array of nanowires in a dielectric host [14]. (b) Scanning electron microscope picture of an array of silver nanowires grown in an anodic alumina membrane-side view of the etched membrane's wall showing loose and bent nanowires; bar 10 µm. (c) Bose's transmitting antenna covered by the polarizing wire grid [56].

dielectric permittivity of silver [57] and alumina [58], the out-of-plane dielectric tensor component $\varepsilon_\perp$ (dielectric component in the direction perpendicular to the wire) approaches zero at $\lambda = 873\,\text{nm}$, where $\varepsilon_\perp = -0.0057 + 0.03i$. At this wavelength, the p-polarized intensity transfer function (A.13) exhibits a sharp transmission peak centered around $k_x = 0$ (angular width of $\sim 1.2°$), while s-polarized (A.11) transmittance is nearly independent of the incidence angle and k_x (***Fig.3.17a***). The mesurements (***Fig.3.17b***) of sample transmittance in $p-$ and $s-$polarizations are in a qualitative agreement with theoretical prediction. This suggests that this metamaterial in wavelength range where dielectric permittivity is singular can be used as an angular filter and polarizer.

On the other hand, the investigation of metamaterial nonlinear properties is particularly important in that it can lead to overcoming one of the fundamental limits of nonlinear optics: the fact that most of the optical materials have a relatively weak nonlinear response. The full exploitation of the nonlinear response is possible only if the nonlinear polarization is not a small perturbation to the linear part of the electric displacement field, and generally this is achieved through nonlinearity enhancement or by means of resonant processes or photorefractive processes where the large nonlinearities come at the cost of a large time response. However, as shown in [9], the interplay between the linear part of the electric displacement field and the

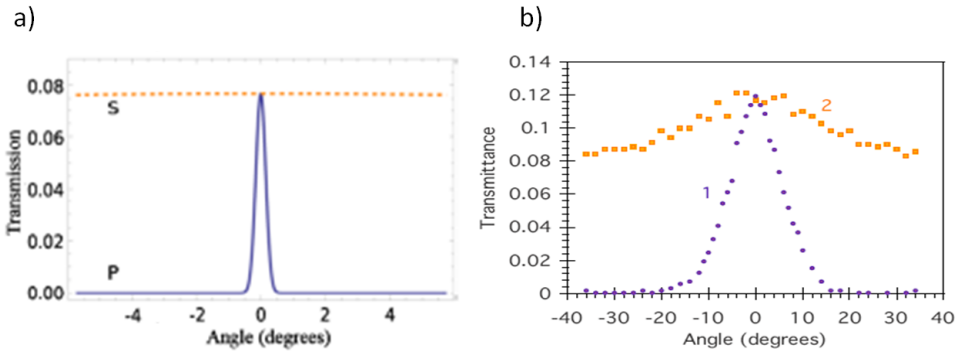

Figure 3.17: It is shown: (a) Transmittance functions for p-polarization (solid) and s-polarization (dashed) in the singular uniaxial regime ($\varepsilon_\perp \approx 0$). (b) Experimentally measured angular transmittance profiles in p-polarization (trace 1) and s-polarization (trace 2) [54].

nonlinear polarization can be made efficient even by following the opposite route, i.e., by reducing the linear polarization. They therefore devise a nonlinear medium with a very small linear dielectric constant since it is a natural setting for the observation of the electromagnetic regime where the nonlinear response does not play the role of a mere perturbation. In that paper, a periodic layered composite whose slabs are filled either with linear media with arbitrary permittivity and permeability or by standard isotropic focusing or defocusing Kerr media is considered. Exploiting a suitable extension of the well-known technique generally used for describing the homogenization of linear layered composites, it is shown that the homogenized medium is characterized by effective constitutive relations formally coinciding with those of a standard Kerr medium whose parameters can assume values not available in standard materials. Exploiting such a parameter availability, they focus on the situation where the linear relative dielectric permittivity is very small, thus allowing the observation of the *extreme nonlinear regime* where the nonlinear polarization is comparable with or even greater than the linear part of the overall dielectric response.

4 Hyperbolic optical switch

In this chapter we considered a liquid crystal/silver nanoparticles mixture and we show that, by suitably choosing the volume filling fraction of the particles, the anisotropic effective medium theory predicts the existence of a spectral range where the permittivity tensor is indefinite. It is theoretically discussed the first example of indefinite optical metamaterial which is obtained by dispersing metal nanoparticles within an anisotropic matrix which is tunable since, due to the presence of the liquid crystal, an external electric field is able to affect its optical response. These achievements allow to consider an active optical device obtained by sandwiching a 300 nm thick slab of the tunable indefinite medium between two 70 nm thick silica layers and operating in the presence of an externally applied electric field. Exploiting the effective medium theory, it is shown that, for optical wavelengths at which the effective medium is indefinite, the slab is completely opaque if the electric field is orthogonal to its interfaces whereas it gradually becomes transparent if it is tilted. Such a behavior is physically due to the fact that the orientation of the hyperbola characterizing the dispersion relation of extraordinary waves through the indefinite medium follows the direction of the applied electric field and therefore, when the hyperbola asymptote is close to be normal to the device interfaces, a switch between evanescent and propagating waves within the medium is achieved thus yielding the switching effect. In order to prove that the considered medium does actually exhibit indefinite permittivity and that the device performs the predicted optical switch functionality, full-wave (FDTD) simulations have been performed and the device

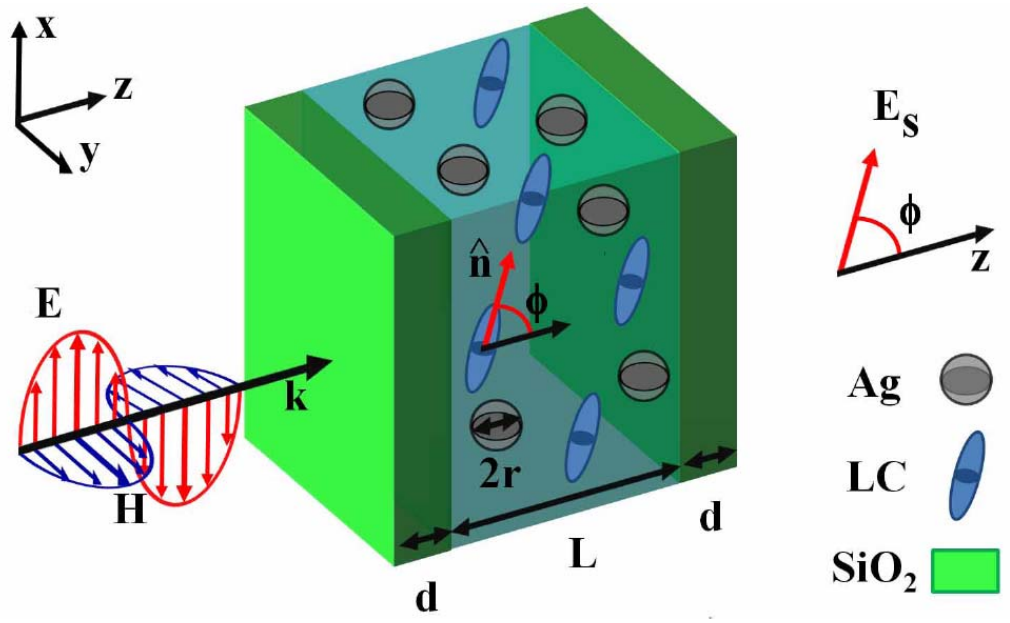

Figure 4.1: Setup geometry. The liquid crystal (LC) fills the slab of thickness L, it is sandwiched between two silica layers of thickness d and it hosts silver nanoparticles (Ag) of radius r. The externally applied electric field $\boldsymbol{E}_S$, inclined at an angle ϕ with the z-axis, aligns the liquid crystal molecules in the direction of the unit vector $\boldsymbol{n}$ (parallel to the electric field). The vacuum electromagnetic plane wave is made to impinge orthogonally onto the device interface.

transmissivity has been evaluated as a function of the wavelength and the applied electric field direction. A spectral region where the device performs the switch exists and it is very close to that predicted by the effective medium theory and, most importantly, that, at a specific wavelength, the actual device transmissivity can be switched between 0.02 and 0.4 through the externally applied electric field. It should be stressed that such a variation of the transmissivity could not be achieved through conventional liquid crystal electro-optical switches of the same thickness $L = 300\,\text{nm}$ since such length is too small, at optical frequencies, to produce the required modal phase difference.

4.1 Liquid crystal silver nanoparticles mixture as a tunable indefinite medium

Consider a slab of thickness L with its interfaces orthogonal to the z-axis, filled with a nematic liquid crystal and sandwiched between to silica layers (see ***Fig.4.1***). If the surface region of the liquid crystal is weakly anchored to the silica walls (condition that can be achieved through suitable surface [59] and/or bulk [60] preparation methods) and if the initial homeotropic director of the liquid crystal molecules are along the z axis, an externally applied electric field $\boldsymbol{E}_S$, lying in the xz plane and forming an angle ϕ with the z-axis, is able to align the liquid crystal homeotropic director along the unit vector $\boldsymbol{n} = \sin\phi \boldsymbol{e}_x + \cos\phi \boldsymbol{e}_z$. As a consequence the liquid crystal optically behaves as a uniaxially anisotropic crystal (with optical axis along the direction $\boldsymbol{n}$) and its permittivity tensor is $\varepsilon^{(LC)} = R\mathrm{diag}\left[\varepsilon_o^{(LC)}, \varepsilon_o^{(LC)}, \varepsilon_e^{(LC)}\right] R^{-1}$ where $\varepsilon_o^{(LC)}$ and $\varepsilon_e^{(LC)}$ are the ordinary and extraordinary permittivities, respectively and R is the y-axis rotation matrix

$$\varepsilon^{(LC)} = \begin{pmatrix} \varepsilon_o^{(LC)}\cos^2\phi + \varepsilon_e^{(LC)}\sin^2\phi & 0 & (\varepsilon_e^{(LC)} - \varepsilon_o^{(LC)})\sin\phi\cos\phi \\ 0 & \varepsilon_o^{(LC)} & 0 \\ (\varepsilon_e^{(LC)} - \varepsilon_o^{(LC)})\sin\phi\cos\phi & 0 & \varepsilon_o^{(LC)}\sin^2\phi + \varepsilon_e^{(LC)}\cos^2\phi \end{pmatrix}$$

The slab hosts silver nanoparticles of radius $r = 10\,\mathrm{nm}$ which are dispersed within the liquid crystal with the volume filling fraction f. If both the the radiation wavelength λ and the slab thickness L are much greater than the nanoparticles radius ($\lambda \gg r$ and $L \gg r$), the overall optical response of the slab can be described by means of the effective medium approach discussed in section §2.2.2. According to this approach, since silver nanoparticles are optically isotropic with scalar permittivity $\varepsilon^{(Ag)}$, the overall effective permittivity tensor is

$$\varepsilon^{(eff)} = R\mathrm{diag}\left[\varepsilon_o^{(eff)}, \varepsilon_o^{(eff)}, \varepsilon_e^{(eff)}\right] R^{-1}$$

so that the homogeneous effective medium is a uniaxial crystal with optical axis along the direction $\boldsymbol{n}$ and its ordinary ($j = o$) and extraordinary ($j = e$) effective

permittivities are (2.28)

$$\varepsilon_j^{(eff)} = \left\{ 1 + \frac{f\left[\varepsilon^{(Ag)} - \varepsilon_j^{(LC)}\right]}{\varepsilon_j^{(LC)} + (1-f)N_j\left[\varepsilon^{(Ag)} - \varepsilon_j^{(LC)}\right]} \right\} \varepsilon_j^{(LC)} . \tag{4.1}$$

where the depolarization factors N_j are (2.24)

$$N_j = \frac{1}{2}\int_0^\infty \frac{\varepsilon_j^{(LC)} ds}{\left[1+\varepsilon_j^{(LC)} s\right]\sqrt{\left[1+\varepsilon_o^{(LC)} s\right]^2\left[1+\varepsilon_e^{(LC)} s\right]}} . \tag{4.2}$$

The permittivities of equation (4.1) are the anisotropic generalization of the standard Maxwell Garnett mixing rule (to which equation (4.1) reduces in the isotropic limit where $N_j = 1/3$), the depolarization factors (4.2) accounting for the effect of the anisotropy. Note that, in analogy to the isotropic situation, the nanoparticles radius does not appear in equation (4.1) so that the mixture design have to be performed by tuning the volume filling fraction f.

In order to discuss a feasible example of mixture, it is chosen SG-1 as nematic liquid crystal [61] due to its high birefringence and its ordinary and extraordinary permittivities are reported in ***Fig.4.2a*** as functions of the vacuum wavelength λ in the spectral range between 410 and 430 nm. For the silver permittivity the Drude model has been used

$$\varepsilon^{(Ag)} = \varepsilon_\infty - \frac{\omega_p^2}{\omega^2 + i\Gamma\omega} ,$$

with $\varepsilon_\infty = 4.56$, $\omega_p = 1.38 \times 10^{16}\,\mathrm{s}^{-1}$ and $\Gamma = 0.1 \times 10^{15}\,\mathrm{s}^{-1}$ [58] and the real and imaginary parts of $\varepsilon^{(Ag)}$ are plotted in ***Fig.4.2b*** for λ between 410 and 430 nm. Note that the used scattering rate Γ is an order of magnitude higher than that of bulk silver in order to accounting for the surface scattering (size effect) occurring within the considered nanometric sized particles. After setting $f = 0.05$ for the nanoparticles volume filling fraction, the principal permittivities of the effective medium has been evaluated by (4.1) and their real and imaginary parts are plotted in ***Fig.4.3***. Note that for wavelengths between $\lambda_1 = 418$ nm and $\lambda_2 = 427.5$ nm, $\Re\left(\varepsilon_e^{(eff)}\right) > 0$ and $\Re\left(\varepsilon_o^{(eff)}\right) < 0$ so that the effective medium has indefinite permittivity. Combining this result with the fact that the direction of the optic

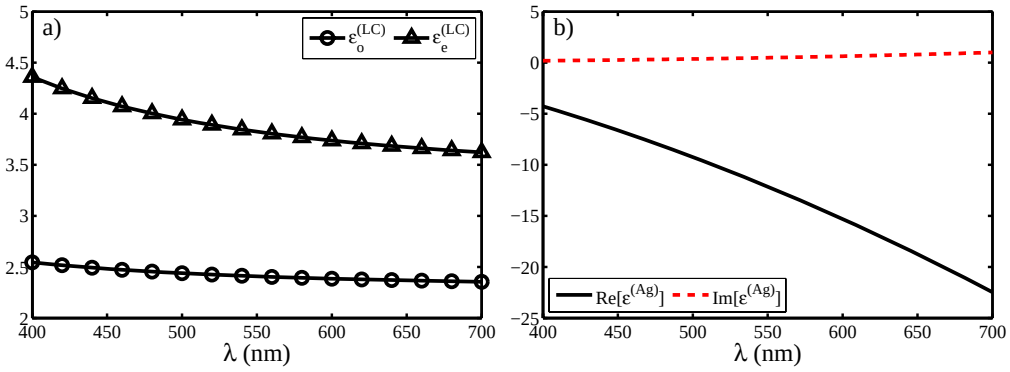

Figure 4.2: Dielectric permittivities as a function of the vacuum wavelength λ. (a) Ordinary and extraordinary permittivities of the liquid crystal. (b) Real and imaginary parts of the silver permittivity.

axis can be varied through the externally applied electric field, we conclude that the proposed liquid crystal/silver nanoparticles mixture behaves, within the limits of validity of the effective medium theory, as a tunable hyperbolic medium.

The above described design of the anisotropic effective medium has been performed for the specific value $f = 0.05$ of the nanoparticles volume filling fraction. In order to complete the analysis and to elucidate the dependence of the whole phenomenology on the parameter f we have evaluated the wavelengths $\lambda_1(f)$ and $\lambda_2(f)$ characterizing the spectral region $\lambda_1(f) < \lambda < \lambda_2(f)$ where the medium is indefinite for $0.02 < f < 0.1$ and plotted them in ***Fig.4.4a***. Note that, for f values close to 5% a tolerance $\Delta f = 0.005$ for the volume filling fraction produces the uncertainties $\Delta\lambda_1 = 1.4\,\text{nm}$ and $\Delta\lambda_2 = 1.7\,\text{nm}$, thus proving that the mixture design is not critical.

4.2 Optical switch

The intriguing optical properties of hyperbolic media combined with the tunability, allow the above described liquid crystal/nanoparticles mixture to be used for conceiving optical devices. As an example, consider the setup of ***Fig.4.1*** where the liquid crystal slab with dispersed nanoparticles has thickness $L = 300\,\text{nm}$ and it is

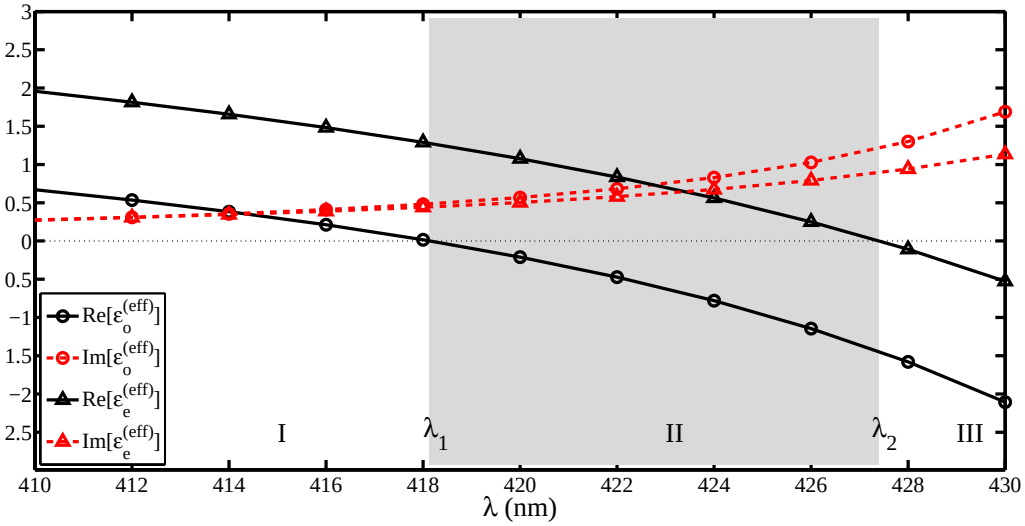

Figure 4.3: Real and imaginary parts of the ordinary and extraordinary permittivities of the homogeneous effective medium. The shaded region ($\lambda_1 < \lambda < \lambda_2$, where $\lambda_1 = 418\,\text{nm}$ and $\lambda_2 = 427.5\,\text{nm}$) corresponds to the spectral range where the effective permittivity tensor is indefinite.

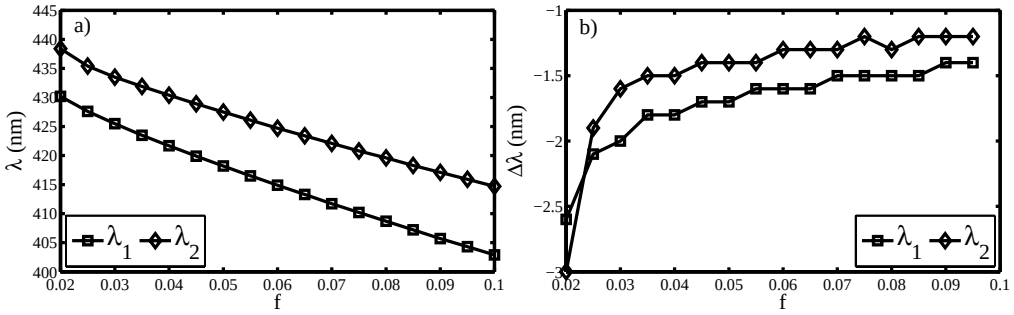

Figure 4.4: (a) Dependence of the wavelengths $\lambda_1(f)$ and $\lambda_2(f)$, characterizing the spectral region $\lambda_1(f) < \lambda < \lambda_2(f)$ where the medium is indefinite, on the nanoparticle volume filling fraction f for $0.02 < f < 0.1$. (b) The uncertainty on the wavelength variation for a volume filling fraction tolerance of $\Delta f = 0.005$.

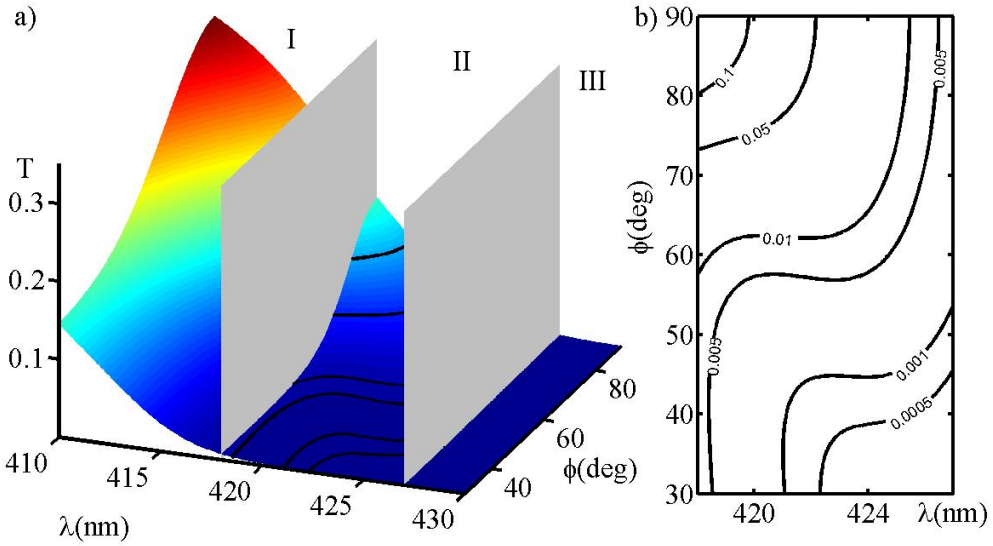

Figure 4.5: (a) Plot of the transmissivity of the device reported in ***Fig.4.1*** (evaluated using the effective medium model for the liquid crystal/nanoparticels mixture) as a function of the vacuum wavelength of the incident radiation and the angle ϕ. (b) Level plot of the transmissivity of panel (a) restricted to region II where the effective medium has indefinite permittivity.

sandwiched between two $d = 70\,\text{nm}$ thick silica layers (of permittivity $\varepsilon^{(S)} = 2.088$). If a monochromatic plane wave is made to impinge orthogonally, from vacuum, onto the device interface (as sketched in ***Fig.4.1***), it is evident that we are considering an active device since its optical transmissivity can be altered by varying the direction of the externally applied electric field $\boldsymbol{E}_S$. Using the effective medium approach discussed in §4.1 to evaluate the dielectric permittivity tensor elements of liquid crystal/nanoparticles mixture, the device transmissivity to an impinging orthogonally electromagnetic plane wave (§Appendix A, (A.13) or (A.11), for normal incidence they are the same equation) is easily evaluated and it is reported in ***Fig.4.5a***, as a function of both the vacuum wavelength λ and the angle ϕ defining the direction of the applied electric field. For clarity purposes, in ***Fig.4.5a*** we have reported two transparent gray planes corresponding to the two wavelengths 418 and 427.5 nm between which the effective medium predicts that the mixture is hyperbolic. The most striking feature of ***Fig.4.5a*** is the existence of three relevant spectral regions,

I) $\lambda < 418\,\text{nm}$, II) $418\,\text{nm} < \lambda < 427.5\,\text{nm}$ and III) $\lambda > 427.5\,\text{nm}$, where the transmissivity is characterized by qualitatively different behaviors. Specifically within regions I and III, the slab is almost transparent and completely opaque, respectively whereas, within region II the transmissivity strongly depends on ϕ to the point that $T \simeq 0$ for $\phi \simeq 0$ and, for increasing ϕ, it gradually increases eventually reaching its maximum (dependent on λ) for $\phi = \pi/2$ (see ***Fig.4.5b*** where the level plot of the transmissivity of region II is plotted). Therefore, within region II, the considered structure can be regarded as a very thin optical switch which, being driven by the external electric field, is able to completely stop or allow the transmission of the light flow. Physically, such an overall behavior is readily grasped by noting that within region I and III (see ***Fig.4.3c***) the effective medium behaves as a uniaxial crystal and an anisotropic conductor, respectively and therefore, within the same two regions, the plane wave impinging from vacuum excites homogeneous and evanescent waves, respectively. On the other hand, within region II the effective medium is indefinite so that, depending on the value of ϕ, the normally impinging plane wave incoming from vacuum is able to excite either homogeneous or evanescent waves. In order to clarify this crucial point, we start from the dispersion relation of extraordinary plane waves

$$\frac{k_x'^2}{\varepsilon_e^{(eff)}} + \frac{k_z'^2}{\varepsilon_o^{(eff)}} = k_0^2\,, \tag{4.3}$$

where k_x' and k_z' are the components of the wave vector along the principal axis of the uniaxial crystal and $k_0 = 2\pi/\lambda$. Since the plane wave from vacuum normally impinges onto the device interface (see ***Fig.4.1***), conservation of momentum requires that the wave vector of waves excited within the anisotropic slab is $\boldsymbol{K} = K\boldsymbol{e}_z$, i.e. it is along the z-axis. Therefore the wavevector components along the principal axis are $k_x' = -K\sin\phi$ and $k_z' = K\cos\phi$ which, inserted into (4.3) yield

$$K(\phi) = k_0\sqrt{\frac{\varepsilon_o^{(eff)}\varepsilon_e^{(eff)}}{\varepsilon_o^{(eff)}\sin^2\phi + \varepsilon_e^{(eff)}\cos^2\phi}}\,, \tag{4.4}$$

from which the impact of the angle ϕ on the excited waves is particularly evident. Even though we are not neglecting absorption (see the imaginary parts of the permittivity in ***Fig.4.3***), it is convenient here to regard the principal permittivities as

real quantities with $\varepsilon_o^{(eff)} < 0$ and $\varepsilon_e^{(eff)} > 0$. Therefore, from (4.4), we readily obtain that $K(0)$ is imaginary (evanescent waves) whereas $K(\pi/2)$ is real (homogeneous waves), the switch between the two kinds of waves occurring at the angle $\phi = \arctan\sqrt{-\varepsilon_e^{(eff)}/\varepsilon_o^{(eff)}}$. This explains the dependence of T on ϕ within region II of ***Fig.4.5*** where, as discussed above, a realistic situation is reported in which absorption is not neglected (the only effects of absorption being the smoothing of the dependence of T on ϕ and the lowering of values of T).

The just described mechanism is pictorially sketched in ***Fig.4.6*** where we have reported the transmissivity $T(\phi)$ for $\lambda = 420\,\text{nm}$ extracted from ***Fig.4.5a***. In the insets A) and B) of ***Fig.4.6*** we have plotted the hyperbolas of (4.3) in the two relevant situations (A) $\phi = 20°$ and (B) $\phi = 80°$ (regarding the permittivities as real quantities). The direction of the applied electric field is able to physically rotate the medium hyperbola and, as a consequence, in the two situations $\phi = 20°$ and $\phi = 80°$ the hyperbola does not intersect and intersects the z-axis, respectively, thus correspondingly allowing the normally impinging vacuum wave to excite evanescent and homogeneous waves. The switch between the two kinds of waves occurs when the hyperbola asymptote is nearly normal to the slab interface and this occurs for ϕ close to $\arctan\sqrt{-\varepsilon_e^{(eff)}/\varepsilon_o^{(eff)}}$.

4.3 Full wave simulations

In order to check the homogenization of the liquid crystal/nanoparticles mixture and the device switching functionality, we have performed 3D full-wave simulations by means of a finite-element solver, using the numerical values of the parameters (constituent permittivities, nanoparticles radius and volume filling fraction, layers thicknesses, etc.) considered so far. In ***Fig.4.7*****a** we have plotted the resulting transmissivity T as a function of the vacuum wavelength λ and the angle ϕ. It is worth noting that, even though the surface of ***Fig.4.7*****a** does not strictly coincide with that of ***Fig.4.5*****a**, it is however evident that the actual structure is almost transparent and practically opaque for wavelengths λ smaller than 430 nm and greater than

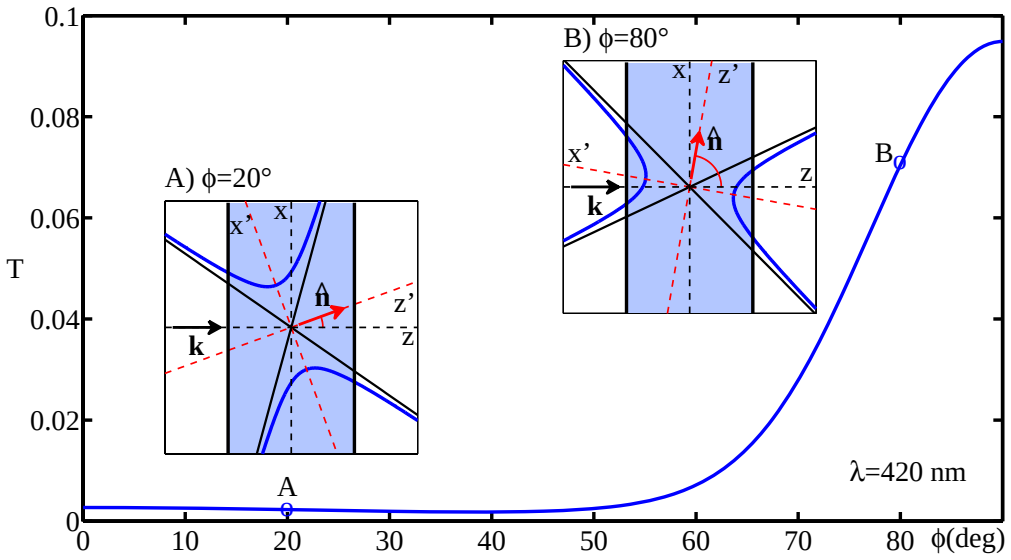

Figure 4.6: Transmissivity $T(f)$ for $\lambda = 420\,\text{nm}$ extracted from ***Fig.4.5a***. In the insets, the extraordinary waves hyperbolas of 4.3 are plotted in the two relevant situations (A) $\phi = 20°$ and (B) $\phi = 80°$ (regarding the permittivities as real quantities).

445 nm, respectively. In addition, in the spectral range between 430 and 445 nm the transmissivity strongly depends on the angle ϕ and, at a given λ, $T(\phi)$ is a monotonically increasing function of ϕ (see ***Fig.4.7b***). As a consequence, even though the spectral ranges are slightly different from those predicted by the effective medium approach, the sample behavior changes, for increasing radiation wavelengths, from that of a dielectric uniaxial crystal to that of an anisotropic conductor with an intermediate spectral region where the medium is hyperbolic. In ***Fig.4.7b*** we have plotted the transmissivity of the structure as a function of ϕ for three relevant wavelengths and the switching functionality is particularly evident. Moreover, since the transmissivity spans the range between 0.02 and 0.4 for $\lambda = 425\,\text{nm}$, we conclude that the performance of the actual switching device is better than that predicted by the effective medium theory (whose transmissivity range is between 0 and 0.15).

The discrepancies between the predictions of the homogenized effective medium theory and those of the full-wave simulations are a consequence of the fact that, for the chosen slab thickness $L = 300\,\text{nm}$, the edge effect due to the nanoparticles

close to the slab interface can not be strictly neglected. The derivation of the Maxwell-Garnett mixing rule (whose anisotropic extension has been used in this paper) is based on the evaluation of the polarizability of an isolated nanoparticle experiencing an external field which is uniform within its volume. For particle belonging to the mixture bulk, these requirements are fulfilled if the nanoparticle size is much smaller than the wavelength and if the nanoparticles volume filling fraction is very small. However, for nanoparticles close to the sample interface the above polarizability evaluation is wrong since it does not take into account the additional field existing within the nanoparticle volume which is due to surface polarization charges (i.e. to the discontinuity of the electromagnetic material properties at the interface) [62]. Since the corrections to the permittivity scale as $(r/z)^3$ (z being the distance from the interface) the nanoparticles responsible for the edge effect are those whose distance from the interface is smaller than 40 or 50 nm (four or five times the radius $r = 10\,\mathrm{nm}$), so that we conclude that roughly a fourth of the considered slab volume can not be described through the Maxwell-Garnett approach.

4.4 Conclusions

We have proposed a novel way for synthesizing indefinite media by dispersing metal nanoparticle within a highly birefringent liquid crystal. In addition to its simplicity and feasibility, the proposed mixture is also tunable since an externally applied electric field is able to change the overall effective permittivity tensor. Tunability of an indefinite medium is a very important property since, as we have shown, the ability of altering the orientation of the extraordinary wave hyperbola allows one to literally choose whether the electromagnetic field within the medium (as due to a give external excitation) has to be composed of propagating homogeneous or an evanescent waves. We have exploited such a property characterizing tunable indefinite media to design a nanometric thick optical switch and investigated its functionality both through the effective medium approach and through full wave simulations. The effective medium approach has the sufficient simplicity to highlight the basic

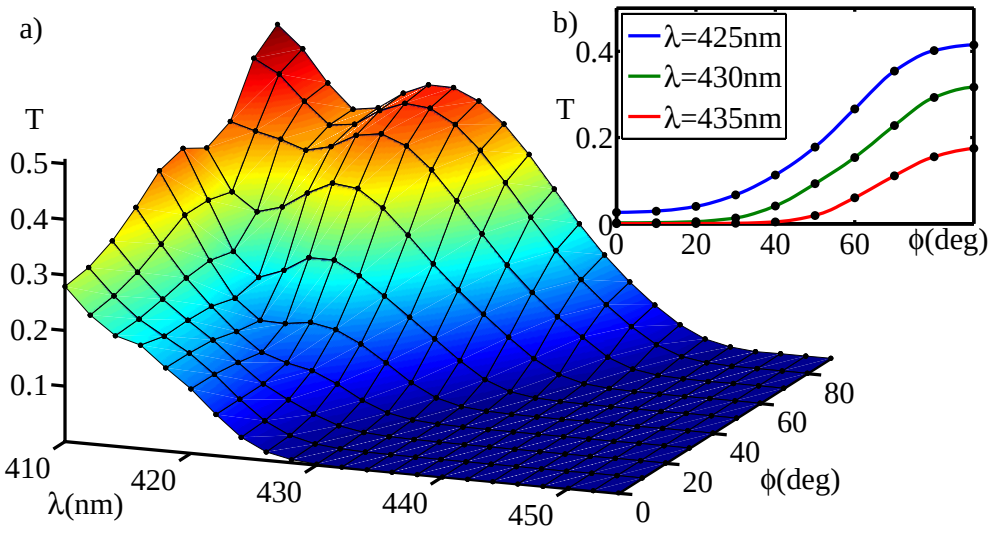

Figure 4.7: (a) Plot of the transmissivity of the device reported in ***Fig.4.1*** (evaluated using the effective medium model for the liquid crystal/nanoparticels mixture) as a function of the vacuum wavelength of the incident radiation and the angle ϕ. (b) Level plot of the transmissivity of panel (a) restricted to region II where the effective medium has indefinite permittivity.

physical mechanisms supporting the device functionality. On the other hand, full wave simulations yield results which are slightly different from those predicted by the effective medium approach and the discrepancy are related to the very small device thickness we decided to consider. However, from the point of view of the device functionality, the results of the full wave simulations are even better than those of the effective medium approach.

5 Subwavelength etalons

In this chapter, it is discussed the problem of restoring resonances in deep subwavelength structures by resorting to indefinite or hyperbolic metamaterials. If the thickness of a plane-parallel plate of solid transparent material is much smaller than the wavelength of operating external radiation, no standing wave is supported by such etalon since resonances can occur if the thickness is equal to a multiple of half wavelength of the incident plane wave. We suggest a genuinely novel and striking mechanism for achieving the target of forcing a subwavelength system to resonate. A subwavelength system can support standing waves and can hence resonate if the medium exhibits a plane wave dispersion relation which is unbounded in the wavevectors space. We prove that the hyperbolic dispersion of plane waves exhibited by indefinite media allows the vacuum radiation to couple with medium plane waves with longitudinal wavenumbers large enough to yield standing waves within the subwavelength slab thickness. Our findings can form the basis of a novel way for shrinking optical devices down to the deep subwavelength scale and we discuss some unusual and innovative applications of this system in the next chapter.

5.1 Fabry-Perot etalon

The Fabry-Perot etalon, or interferometer, can be considered as the best example of an optical resonator. It consists of a plane-parallel plate of thickness L and refractive index n that is immersed in a medium of index n'. Generally, an etalon

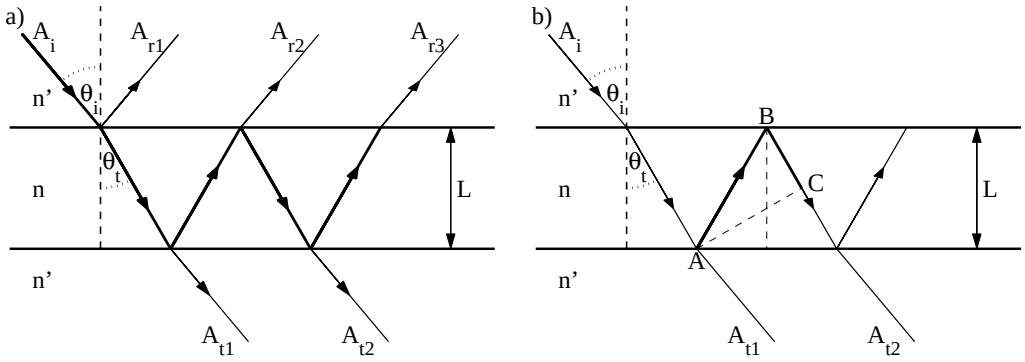

Figure 5.1: a) Multiple-reflection model for analyzing the Fabry-Perot etalon. b) Path difference between successive reflections inside the Fabry-Perot etalon, their path difference Δl is given by $\Delta l = AB + BC = L/\cos\vartheta_t + L\cos(2\vartheta_t)/\cos\vartheta_t = 2L\cos\vartheta_t$ [63].

can be obtained by spacing two partially reflecting mirrors at a distance L apart so that $n = n' = 1$. Another common form of etalon is produced by grinding two plane-parallel (or curved) faces on a transparent solid and then evaporating a metallic or dielectric layer (or layers) on the surfaces. The term etalon is often reserved for a plane-parallel plate of solid transparent material with reflecting surfaces on both sides, while interferometers (or cavities) are reserved for structures that consist of two parallel mirrors with an empty space in between.

Let a plane wave be incident on the lossless isotropic etalon at an angle ϑ_i to the normal, as shown in ***Fig.5.1a***. We can treat the problem of transmission (and reflection) of the plane wave through the etalon by considering the infinite number of partial waves produced by multiple reflections at the two end surfaces. The phase delay between two partial waves, which is attributable to one additional round trip, is given, according to ***Fig.5.1b***, by

$$\delta = \frac{2\pi}{\lambda} 2nL\cos\vartheta_t\,,$$

where λ is the vacuum wavelength of the incident wave and ϑ_t is the transmitted angle (or internal angle of incidence). If the complex amplitude of the incident wave is taken as A_i then the partial reflection amplitudes, A_{r1}, A_{r2}, and so forth, are

given by

$$A_{r1} = rA_i\,, \qquad A_{r2} = tt'r'A_ie^{-i\delta}\,, \qquad A_{r3} = tt'r'^3A_ie^{-2i\delta}\,, \qquad \ldots$$

where r is the amplitude reflection coefficient of the interface (ratio of reflected to incident amplitude), t is the amplitude transmission coefficient for waves incident from n' toward n, and r' and t' are the corresponding quantities for waves traveling from n toward n'. The complex amplitude of the (total) reflected wave is $A_r = A_{r1} + A_{r2} + A_{r3} + \ldots$, or

$$A_r = \left[r + tt'r'e^{-i\delta}\left(1 + r'^2e^{-i\delta} + r'^4e^{-2i\delta} + \ldots\right)\right]A_i\,. \tag{5.1}$$

For the transmitted wave, the amplitudes of the partial waves are

$$A_{t1} = tt'A_ie^{i\delta/2}\,, \qquad A_{t2} = tt'r'^2e^{-i\delta}A_ie^{i\delta/2}\,, \qquad A_{t3} = tt'r'^4e^{-2i\delta}A_ie^{i\delta/2}\,, \qquad \ldots$$

where the phase factor $e^{-i\delta/2}$ corresponds to a single traversal of the plate and is common to all terms. Adding up the A_{tj} terms, we obtain

$$A_t = tt'\left[1 + r'^2e^{-i\delta} + r'^4e^{-2i\delta} + \ldots\right]A_ie^{-i\delta/2}\,, \tag{5.2}$$

for the complex amplitude of the total transmitted wave. We notice that the terms within the parentheses in (5.1) and in (5.2) form an infinite geometric series; adding them, we get

$$A_r = \frac{r - rr'^2e^{-i\delta} + tt'r'e^{-i\delta}}{1 - r'^2e^{-i\delta}}A_i\,, \qquad A_t = \frac{tt'e^{-i\delta/2}}{1 - r'^2e^{-i\delta}}A_i\,.$$

Using the fact that $r' = -r$ for the dielectric interface, the conservation-of-energy $r^2 + tt' = R + T = 1$ we arrive to

$$A_r = \frac{\left(1 - e^{-i\delta}\right)\sqrt{R}}{1 - Re^{-i\delta}}A_i\,, \qquad A_t = \frac{Te^{-i\delta/2}}{1 - Re^{-i\delta}}A_i\,, \tag{5.3}$$

with R and T are, respectively, the fraction of the intensity reflected and transmitted at each interface and will be referred to in the following discussion as the etalon's reflectance and transmittance.

If the incident intensity is taken as $A_i A_i^*$, we obtain from (5.3) the following expression for the fraction of the incident intensity that is reflected by the etalon

$$R_e = \frac{I_r}{I_i} = \frac{A_r A_r^*}{A_i A_i^*} = \frac{2R\left(1-\cos\delta\right)}{1-2R\cos\delta+R^2} = \frac{4R\sin^2\left(\delta/2\right)}{\left(1-R\right)^2+4R\sin^2\left(\delta/2\right)}$$

and for the transmitted fraction

$$T_e = \frac{I_t}{I_i} = \frac{A_t A_t^*}{A_i A_i^*} = \frac{T^2}{\left(1-R\right)^2+4R\sin^2\left(\delta/2\right)} = \frac{\left(1-R\right)^2}{\left(1-R\right)^2+4R\sin^2\left(\delta/2\right)},$$

which, by defining as $F = 4R/(1-R)^2$, becomes

$$T_e = \frac{1}{1+F\sin^2\left(\delta/2\right)}. \tag{5.4}$$

According to (5.4) the transmission is unity whenever $\delta = 2m\pi$ with m any integer.

$$\delta = \frac{2\pi}{\lambda}2nL\cos\vartheta_t = 2m\pi \quad \Rightarrow \quad \lambda_m = 2L\frac{\sqrt{n^2-n'^2\sin^2\vartheta_i}}{m},$$

for a fixed L and ϑ_i the above equation defines the unitary transmission (resonance) wavelength of the etalon. From an other point of view, for a fixed n, n' and incidence angle ϑ_i the etalon's standing waves occurs if the etalon's thickness L is equal to a multiple of half wavelength of the incident plane wave

$$L = \frac{m}{\sqrt{n^2-n'^2\sin^2\vartheta_i}}\frac{\lambda}{2}. \tag{5.5}$$

The expression for etalon's transmittance (5.4), know as Airy expression, holds if the considered materials (n and n') are isotropic and no loss mechanisms are present; otherwise the correct expression is (A.11) for TE impinging plane wave and (A.13) for a TM one.

5.2 Optical resonances restoring

We analyze the existence of the etalon's standing waves for a TE and a TM field geometry on a plane-parallel plate of transparent lossless uniaxial material ($\varepsilon = \mathrm{diag}\left[\varepsilon_x, \varepsilon_x, \varepsilon_z\right]$, absorption can be neglected and the permittivities are real) when the resonator's thickness is standard (L is generally much larger than the wavelength

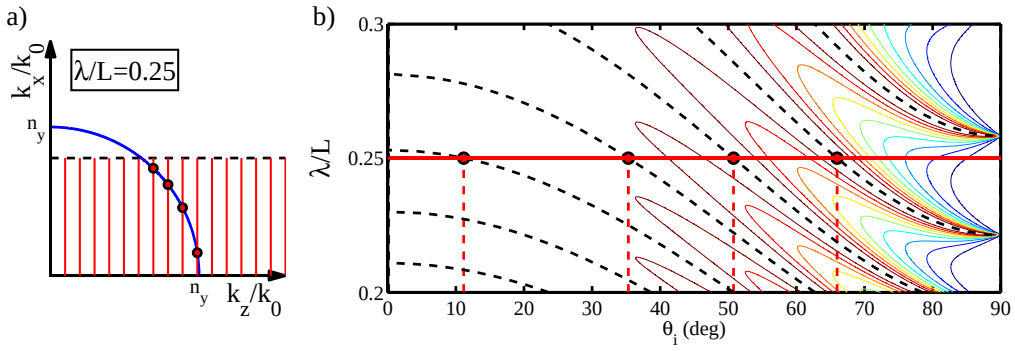

Figure 5.2: TE plane wave on a lossless uniaxial material with $n_y^2 = \varepsilon_y = 1.6$ in a standard case $\lambda/L = 0.25$: a) Ordinary dispersion relation (blue curve) $k_x^2/\varepsilon_y + k_z^2/\varepsilon_y = k_0^2$ with the wave vectors $k_z/k_0 = m\lambda/(2L)$ (vertical red lines) and relative intersections (circles) corresponding to the available slab standing waves. b) Contour of etalon's transmittance, black dashed curves are the unitary level curves which intersect the horizontal line $\lambda/L = 0.25$ whenever the resonance condition is satisfied and the red circles identify the corresponding incident angle for the external TE wave.

of the interacting radiation, standard case $\lambda \ll L$) and when it is subwavelength (subwavelength case $\lambda \gg L$). For each condition we consider, where possible, the hyperbolic (permittivities with opposite sign) and near-zero (permittivities with amplitude smaller than one) cases.

Fig.5.2a shows the ordinary dispersion relation (blue curve) for an impinging TE plane wave with wave vector in xz plane ($k_x^2/\varepsilon_y + k_z^2/\varepsilon_y = k_0^2$) on a lossless uniaxial material with real positive and larger than one permittivity ($\varepsilon_y = 1.6$) in a standard case ($\lambda/L \ll 1$). In the etalon's transmittance (5.4) for a TE plane wave we have

$$F = \frac{1}{4}\left(N_{TE} - \frac{1}{N_{TE}}\right)^2, \qquad \frac{\delta}{2} = k_z L\,,$$
$$N_{TE} = \frac{k_0 \cos\vartheta_i}{k_z}, \qquad k_z = k_0\sqrt{\varepsilon_y - \sin^2\vartheta_i}$$

and it is unit whenever the normalized wave vector $k_z/k_0 = m\lambda/(2L)$ (depicted in ***Fig.5.2a*** through red vertical lines for a fixed ratio of $\lambda/L = 0.25$). The mutual intersections between vertical lines and ordinary wave dispersion correspond to available slab standing wave (circles). If the resonance condition $k_z/k_0 = m\lambda/(2L)$

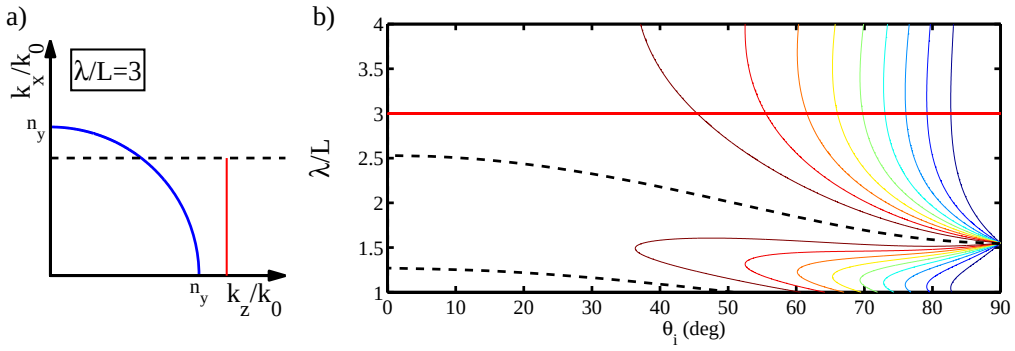

Figure 5.3: TE plane wave on a lossless uniaxial material with $n_y^2 = \varepsilon_y = 1.6$ in a subwavelength case $\lambda/L = 3$: a) Ordinary dispersion relation (blue curve) $k_x^2/\varepsilon_y + k_z^2/\varepsilon_y = k_0^2$ with the wave vectors $k_z/k_0 = m\lambda/(2L)$ (vertical red lines); since there are not intersections (circles), vacuum radiation does not couple with slab standing waves. b) Contour of etalon's transmittance, the unitary level curves (black dashed curves) do not intersect the horizontal line $\lambda/L = 3$ and the resonance condition is not satisfied for any incident angle.

holds, the impinging wave couples to one of the slab standing waves and this occurs for the incident angles

$$\vartheta_i^{(m)} = \arcsin\sqrt{\varepsilon_y - \left(m\frac{\lambda}{2L}\right)^2}\,.$$

They correspond to the intersections of the unitary transmittance contour (black dashed curves) with the considered value of ratio λ/L (horizontal line) and they are emphasized in ***Fig.5.2b*** by red circles. Analyzing the same situation in a subwavelength case (***Fig.5.3*** $\lambda/L = 3$), it is evident that the 4 different resonance incident angles (corresponding to $m = [7, 10]$), picked out in standard case, don't exist and any standing wave is supported by this kind of etalon, because the first resonant wave vector k_z is out of the allowed range ($\sqrt{\varepsilon_y - 1} < k_z/k_0 < \sqrt{\varepsilon_y}$).

Fig.5.4a shows the extraordinary dispersion relation (blue curve) for an impinging TM plane wave with wave vector in xz plane ($k_x^2/\varepsilon_z + k_z^2/\varepsilon_x = k_0^2$) on a lossless uniaxial material with real positive and larger than one permittivity ($\varepsilon_x = 1.6$ and $\varepsilon_z = 1.3$) in a standard case. In the etalon's transmittance (5.4) for a TM plane

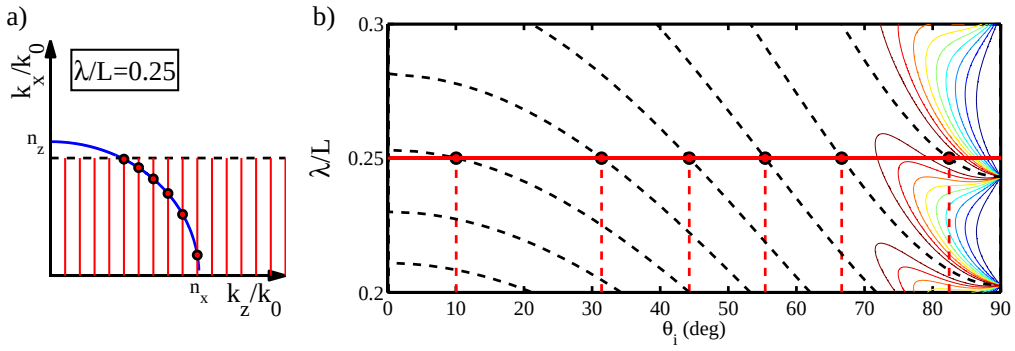

Figure 5.4: TM plane wave on a lossless uniaxial material with $n_x^2 = \varepsilon_x = 1.6$ and $n_z^2 = \varepsilon_z = 1.3$ in a standard case $\lambda/L = 0.25$: a) Extraordinary dispersion relation (blue curve) $k_x^2/\varepsilon_z + k_z^2/\varepsilon_x = k_0^2$ with the wave vectors $k_z/k_0 = m\lambda/(2L)$ (vertical red lines) and relative intersections (circles) corresponding to the available slab standing waves. b) Contour of etalon's transmittance, black dashed curves are the unitary level curves which intersect the horizontal line $\lambda/L = 0.25$ whenever the resonance condition is satisfied and the red circles identify the corresponding incident angle for the external TM wave.

wave we have

$$F = \frac{1}{4}\left(N_{TM} - \frac{1}{N_{TM}}\right)^2, \qquad \frac{\delta}{2} = k_z L\,,$$

$$N_{TM} = \frac{\varepsilon_x k_0 \cos\vartheta_i}{k_z}\,, \qquad k_z = k_0\sqrt{\varepsilon_x\left(1 - \frac{\sin^2\vartheta_i}{\varepsilon_z}\right)}$$

and we have coupling between an external plane wave and slab standing waves if the integer m is such that $\sqrt{\varepsilon_x(\varepsilon_z - 1)/\varepsilon_z} < k_z/k_0 < \sqrt{\varepsilon_x}$. For the considered permittivities and λ/L, there exist 6 incident angles which satisfy the resonance condition ($m = [5, 10]$). The extraordinary waves experience the effects of the anisotropic behavior of the material and of its possible hyperbolic nature. ***Fig. 5.5*** and ***Fig. 5.6*** report the considered scenario if one permittivity of the etalon's dielectric tensor is negative. If $\varepsilon_x < 0$ and $\varepsilon_z > 0$ the dispersion curve is an hyperbola with vertices on k_x axis and for permittivities with module larger than one any resonance is supported by etalon (***Fig. 5.5***). Instead, if $\varepsilon_x > 0$ and $\varepsilon_z < 0$ the dispersion curve is an hyperbola with vertices on k_z axis and a range of k_z allowing resonance exists ($\sqrt{\varepsilon_x} < k_z/k_0 < \sqrt{\varepsilon_x(1 + |\varepsilon_z|)/|\varepsilon_z|}$, ***Fig. 5.6***).

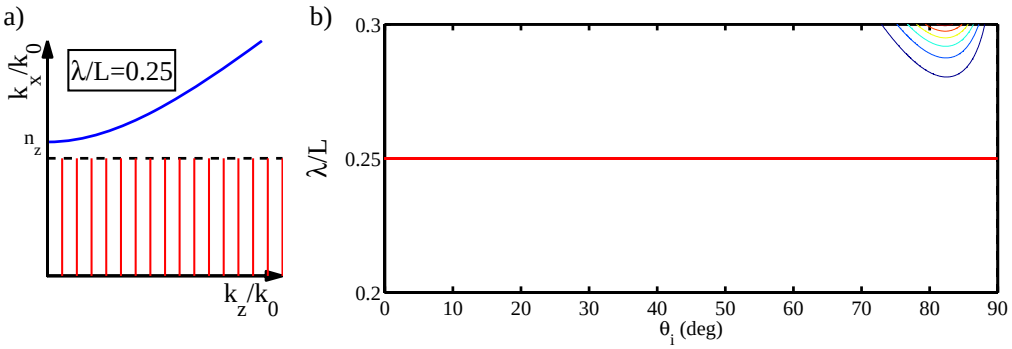

Figure 5.5: TM plane wave within a lossless uniaxial material with $\varepsilon_x = -1.6$ and $n_z^2 = \varepsilon_z = 1.3$ in a standard case $\lambda/L = 0.25$: a) Extraordinary hyperbolic dispersion relation (blue curve) $k_x^2/\varepsilon_z - k_z^2/|\varepsilon_x| = k_0^2$ with the wave vectors $k_z/k_0 = m\lambda/(2L)$ (vertical red lines); since there are not intersections (circles), vacuum radiation does not couple with slab standing waves. b) Contour of etalon's transmittance, the unitary level curves (black dashed curves) do not intersect the horizontal line $\lambda/L = 0.25$ and the resonance condition is not satisfied for any incident angle.

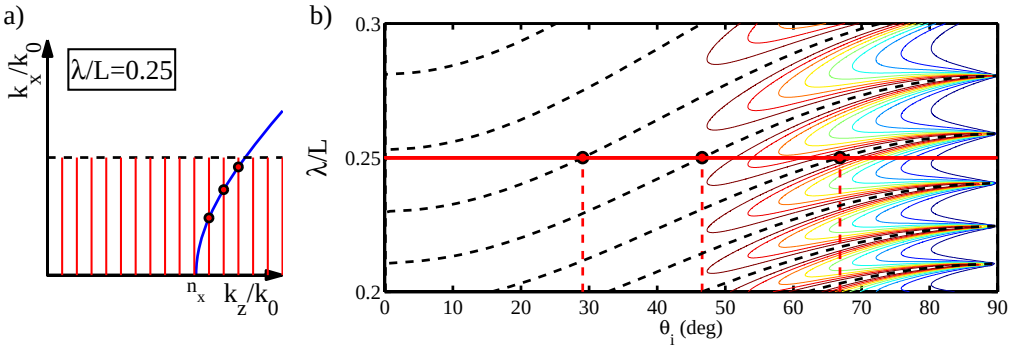

Figure 5.6: TM plane wave within a lossless uniaxial material with $n_x^2 = \varepsilon_x = 1.6$ and $\varepsilon_z = -1.3$ in a standard case $\lambda/L = 0.25$: a) Extraordinary hyperbolic dispersion relation (blue curve) $-k_x^2/|\varepsilon_z| + k_z^2/\varepsilon_x = k_0^2$ with the wave vectors $k_z/k_0 = m\lambda/(2L)$ (vertical red lines) and relative intersections (circles) corresponding to the available slab standing waves. b) Contour of etalon's transmittance, black dashed curves are the unitary level curves which intersect the horizontal line $\lambda/L = 0.25$ whenever the resonance condition is satisfied and the red circles identify the corresponding incident angle for the external TM wave.

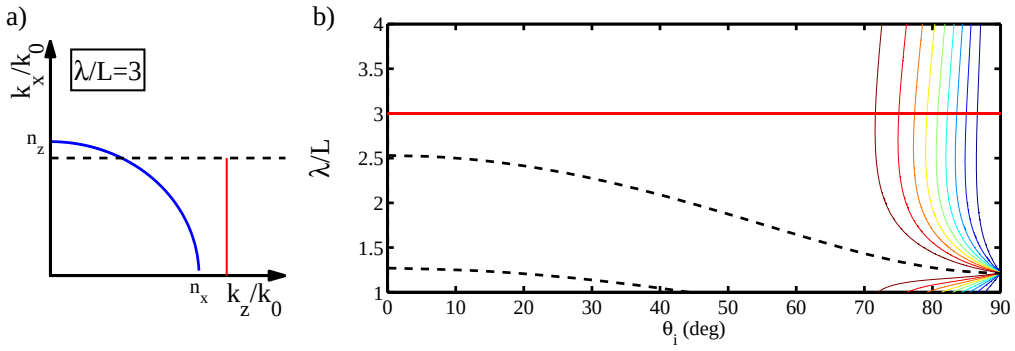

Figure 5.7: TM plane wave on a lossless uniaxial material with $n_x^2 = \varepsilon_x = 1.6$ and $n_z^2 = \varepsilon_z = 1.3$ in a subwavelenght case $\lambda/L = 3$: a) Extraordinary hyperbolic dispersion relation (blue curve) $k_x^2/\varepsilon_z + k_z^2/\varepsilon_x = k_0^2$ with the wave vectors $k_z/k_0 = m\lambda/(2L)$ (vertical red lines); since there are not intersections (circles), vacuum radiation does not couple with slab standing waves. b) Contour of etalon's transmittance, the unitary level curves (black dashed curves) do not intersect the horizontal line $\lambda/L = 3$ and the resonance condition is not satisfied for any incident angle.

As for TE waves, if etalon's L dimension is lower than the vacuum radiation wavelength, also for TM waves resonances are forbidden, since the etalon's standing waves occurs if the etalon's thickness L is equal to a multiple of half wavelength of incident plane wave (5.5). In particular, if the permittivities ε_x and ε_z are both positive (***Fig.5.7***)

$$m\frac{\lambda}{2}\frac{1}{\sqrt{\varepsilon_x}} < L < m\frac{\lambda}{2}\sqrt{\frac{\varepsilon_z}{\varepsilon_x(\varepsilon_z - 1)}},$$

if $\varepsilon_z < 0$ (***Fig.5.9***)

$$m\frac{\lambda}{2}\sqrt{\frac{|\varepsilon_z|}{\varepsilon_x(|\varepsilon_z| + 1)}} < L < m\frac{\lambda}{2}\frac{1}{\sqrt{\varepsilon_x}},$$

while if $\varepsilon_x < 0$ the hyperbolic dispersion curve is always out of the range allowed by conservation of k_x (***Fig.5.8***) and this bounds for L are hardly compatible with the subwavelength condition. Nevertheless, observing the shape of TM hyperbolic dispersion curves (***Fig.5.8*** and ***Fig.5.9***) it is possible to exploit their unboundedness to restore etalon resonances.

In order for the hyperbolic extraordinary dispersion curves to belong to the wavevector region where the transverse momentum conservation is possible, the

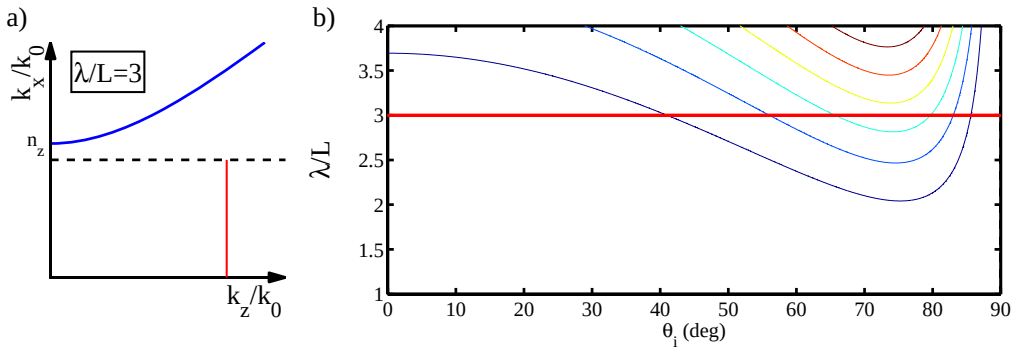

Figure 5.8: TM plane wave on a lossless uniaxial material with $\varepsilon_x = -1.6$ and $n_z^2 = \varepsilon_z = 1.3$ in a subwavelenght case $\lambda/L = 3$: a) Extraordinary hyperbolic dispersion relation (blue curve) $k_x^2/\varepsilon_z - k_z^2/|\varepsilon_x| = k_0^2$ with the wave vectors $k_z/k_0 = m\lambda/(2L)$ (vertical red lines); since there are not intersections (circles), vacuum radiation does not couple with slab standing waves. b) Contour of etalon's transmittance, the unitary level curves (black dashed curves) do not intersect the horizontal line $\lambda/L = 3$ and the resonance condition is not satisfied for any incident angle.

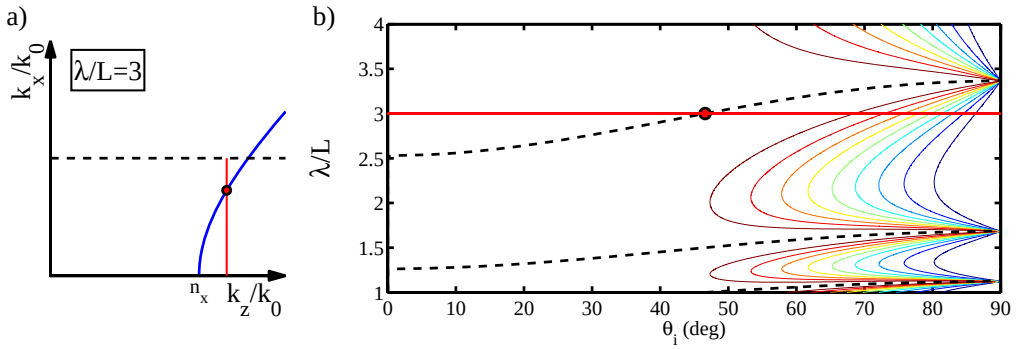

Figure 5.9: TM plane wave on a lossless uniaxial material with $n_x^2 = \varepsilon_x = 1.6$ and $\varepsilon_z = -1.3$ in a subwavelenght case $\lambda/L = 3$: a) Extraordinary hyperbolic dispersion relation (blue curve) $-k_x^2/|\varepsilon_z| + k_z^2/\varepsilon_x = k_0^2$ with the wave vectors $k_z/k_0 = m\lambda/(2L)$ (vertical red lines); there is only one intersection (circles) corresponding to $m = 1$. b) Contour of etalon's transmittance, the unitary level curves (black dashed curves) intersect the horizontal line $\lambda/L = 3$ only one time and the resonance condition is satisfied for one incident angle.

etalon material permittivities are required to have amplitudes smaller than one. Accordingly, either one can move the vertex of the hyperbola $k_x^2/\varepsilon_z - k_z^2/|\varepsilon_x| = k_0^2$ closer to the origin and increase its aperture (***Fig.5.8a***) or it is possible to reduce the angular aperture of the hyperbola $-k_x^2/|\varepsilon_z| + k_z^2/\varepsilon_x = k_0^2$ (***Fig.5.9a***). In ***Fig.5.10a*** and ***Fig.5.10b*** it is shown an example of restoring resonances in subwavelength structures by resorting hyperbolic metamaterials with $|\varepsilon_x| = 0.9$ and $|\varepsilon_z| = 0.01$. The unbounded hyperbolic dispersion of extraordinary plane waves exhibited by such indefinite media allows the vacuum radiation to couple with medium plane waves with longitudinal wavenumbers large enough to yield standing waves within the subwavelength etalon.

5.3 Conclusions

Resonance restoring in subwavelength etalons occurs for hyperbolic media with $|\varepsilon_x| < 1$ and $|\varepsilon_z| < 1$ since, as reported in ***Fig.5.10***, the unbounded hyperbolas have an angular aperture so large or so small to intersect a number of horizontal lines within the white stripe $k_x/k_0 < 1$, thus yielding a number of standing waves which can be actually excited through the plane wave impinging from vacuum. In summary, a subwavelength thick slab exhibits etalon resonances with associated narrow angular transmittance peaks only if the principal permittivities have different signs and have amplitude smaller than one.

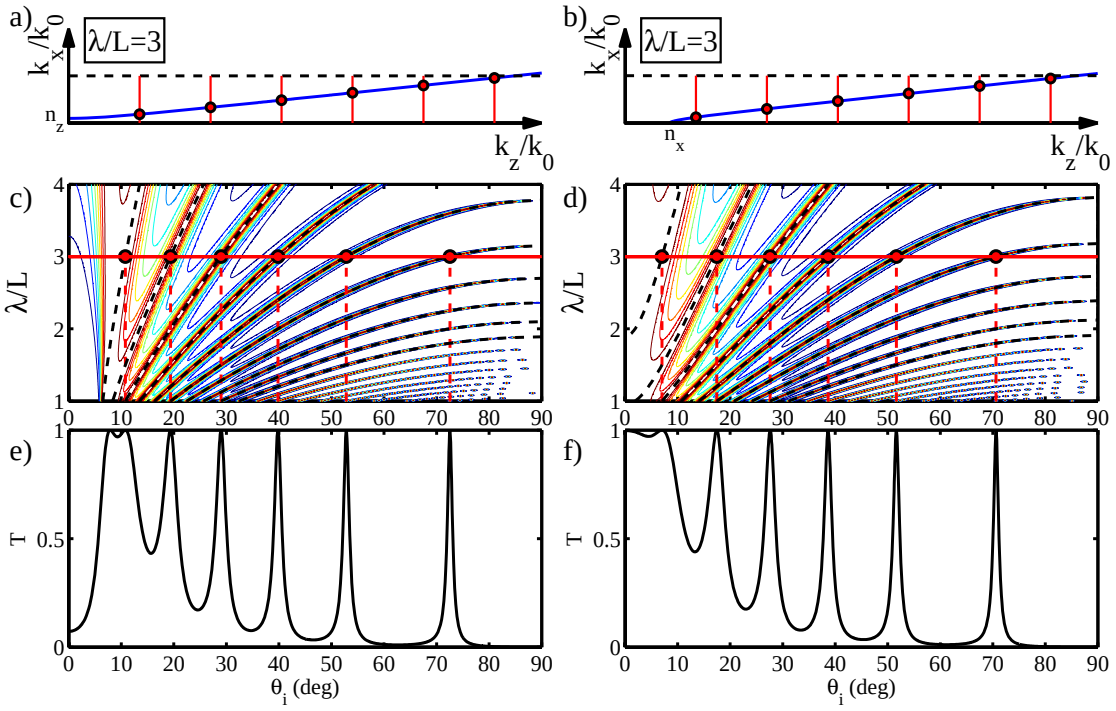

Figure 5.10: TM plane wave on a lossless uniaxial hyperbolic material in a subwavelenght case $\lambda/L = 3$ with permittivities of amplitude smaller than one ($|\varepsilon_x| = 0.9$ and $|\varepsilon_z| = 0.01$). Extraordinary hyperbolic dispersion relation (blue curve) $k_x^2/\varepsilon_z - k_z^2/|\varepsilon_x| = k_0^2$ (a) and $-k_x^2/|\varepsilon_z| + k_z^2/\varepsilon_x = k_0^2$ (b) with the wave vectors $k_z/k_0 = m\lambda/(2L)$ (vertical red lines) and relative intersections (circles) corresponding to the available slab standing waves. c) and d) contour of etalon's transmittance, the unitary level curves (black dashed curves) intersect the horizontal line $\lambda/L = 3$ whenever the resonance condition is satisfied and the red circles identify the corresponding incident angle for the external TM wave. e) and f) are transmittance profiles as function of incident angle when $\lambda/L = 3$.

6 Efficient second harmonic generation

Optical properties of many materials depend on the direction of propagation, on the polarization state and on the intensity of electromagnetic radiation. Optical anisotropic nonlinear materials can exhibit several optical phenomena, including double refraction, polarization effects and electro-optical effects. In particular in this chapter we are concerned on a nonlinear optical process, in which photons interacting with a nonlinear material are combined to form new photons with half the wavelength of the initial ones: the second harmonic generation process.

We theoretically predict efficient optical second harmonic generation from a nanometer thick slab consisting of a quadratic nonlinear anisotropic medium whose linear principal permittivities have, at the fundamental wavelength, real parts of different signs (indefinite permittivity) and magnitude smaller than one. We show that, by illuminating the slab with a p-polarized fundamental wave (with intensity of a few MW/cm^2), highly efficient scattering of the second harmonic field occurs in conditions at which the slab is linearly fully transparent for the fundamental wave, i.e. when the impinging wave couples to one of the slab standing waves (responsible for the etalon resonances, as we have discussed in above chapter). The high efficiency of the second harmonic generation process stems from the enhancement of the longitudinal field, perpendicular to the slab surface, produced by the very small value of the slab dielectric permittivities. We investigate the role played by medium losses showing that, even in the strong absorption regime, the described process yields a second-harmonic field which is much stronger than that produced

by a standard (not indefinite) nonlinear slab.

6.1 Introduction

Enhancing optical second harmonic generation [64, 65] is at present one of the most relevant task of nonlinear optics due to the major role played by frequency-doubling in coherent green and blue light sources design [66], chemistry [67], biosensing [68], etc. In situations where standard phase-matching (§Appendix A) techniques cannot be used, efficient second harmonic generation is generally achieved by resorting to specific configurations providing a strong field enhancement such as, for example, resonant micro-cavities [69, 70, 71] or photonic crystals [72, 73, 74, 75]. Conceiving subwavelength coherent light sources is a fundamental issue of modern nanophotonics [76, 77] so that achieving second harmonic generation from nanostructures is an important target. At the nanometer length scale, the small interaction distances generally entail an highly inefficient second harmonic generation so that peculiar mechanisms for locally enhancing the electromagnetic field of the fundamental wave have to be harnessed. As an example, the plasmonic field enhancement occurring in vicinity of the subwavelength apertures in a metallic film is responsible for an efficient second harmonic generation [78, 79, 80, 81] when the holes are filled by a quadratic nonlinear material. Another strong plasmonic field enhancement occurs within spherical nanocavities with dielectric core and plasmonic nanoshell [82] so that, if the core is filled with a noncentrosymmetric nonlinear medium, a lager enhancement of the second harmonic generation is observed [83].

In this chapter we theoretically show that a micrometer-thick slab consisting of a quadratic nonlinear medium whose linear permittivities are very small and have different signs is able to provide highly efficient second harmonic generation. The properties and applications of ε-near-zero materials have recently been discussed both in the linear [54, 55, 84, 85, 86] and in the nonlinear [9, 87, 88, 89, 90] regimes, and indefinite materials [13, 40, 41, 47, 91] have attracted a good deal of attention as well. Here we point out that the small values of the dielectric permittivity produce a

strong enhancement of the longitudinal field perpendicular to the slab surface. The field enhancement is simply a consequence of the fact that when the slab is fully transparent for the fundamental wave there is obviously no reflected wave so that the vacuum field coincides with that of the incident fundamental wave. Therefore, at the vacuum-slab interface, the normal component of the fundamental field within the slab coincides with the normal component of the incident field divided by the very small dielectric permittivity, as a consequence of one of the field-matching conditions. Such a strong longitudinal field in turn produces a strong enhancement of the second-harmonic polarization source and leads to the possibility of observing a very efficient second harmonic generation process, for impinging optical intensities of a few MW/cm^2, even in a slab whose thickness is comparable with the fundamental wavelength.

Since the whole mechanism supporting the second harmonic generation process considered in the present chapter is based on the fact that the permittivities have magnitudes smaller than 1, it is evident that medium losses play a major role on the discussed phenomenology. Consequently, we have investigated both the linear slab behavior and the second harmonic generation process in three different regimes: the ideal lossless regime (real permittivities), the weak-absorption regime (imaginary parts of the permittivities much smaller than the real parts), and the strong-absorption regime (imaginary parts of the permittivities comparable with the real parts). We have shown that, even though absorption has a strong detrimental effect on the second harmonic generation process, in the weak- and strong-absorption regimes, second harmonic generation efficiencies are still considerable and definitely much larger that those pertaining to second harmonic generation from a standard (not indefinite) quadratic nonlinear slab. This is a remarkable result since we additionally prove that, by considering suitably designed mixtures of liquid crystals and metal nanoparticles, the weak-absorbtion regime can be achieved by adding active components (dye molecules) to the mixture whereas, most importantly, the feasibility of the strong-absorption regime does not demand the use of gain constituents.

6.2 Linear slab resonances and field enhancement

The geometry of the considered second harmonic generation setup is sketched in ***Fig.6.1***, the fundamental and second harmonic quantities being labeled hereafter with the superscripts (1) and (2). The fundamental and second harmonic wavelengths are $\lambda^{(1)}$ and $\lambda^{(2)} = \lambda^{(1)}/2$. The slab of thickness L is a uniaxially anisotropic medium with relative dielectric tensor $\varepsilon = \mathrm{diag}\left[\varepsilon_o^{(1)}, \varepsilon_o^{(1)}, \varepsilon_e^{(1)}\right]$ (i.e., with the optical axis along the z direction) whose ordinary and extraordinary permittivities, $\varepsilon_o^{(1)}$ and $\varepsilon_e^{(1)}$, respectively, have real parts of different signs (indefinite or hyperbolic medium) and magnitude smaller than 1. In addition we chose the slab to exhibit a quadratic nonlinear optical response characterized by the d matrix (see Ref. [92])

$$d = \begin{pmatrix} 0 & 0 & 0 & 0 & 0 & 0 \\ 0 & \delta & \Delta & 0 & 0 & 0 \\ 0 & 0 & 0 & \Delta & 0 & 0 \end{pmatrix} \tag{6.1}$$

since the symmetry properties of such nonlinearity are compatible with the electromagnetic structure of the fundamental wave and second-harmonic wave we are interested in and, remarkably, since they are directly shown by the nanocomposite discussed later[1]. The slab is illuminated by a plane fundamental wave with incidence angle ϑ and with its electric field polarized in the plane of incidence (p-polarization) so that the reflected (r) and transmitted (t) plane fundamental waves are p-polarized as well. The slab also scatters reflected and transmitted second harmonic plane waves whose electric fields are polarized perpendicular to the plane of incidence (s-polarization), as a consequence of the chosen anisotropic quadratic nonlinearity (see ***Fig.6.1*** for the definitions of the field amplitudes and wave vectors).

[1]Note that, for the sake of simplicity, we regard the matrix d of (6.1) to be independent of the frequency since in this paper, apart from the ideal lossless case, we mainly deal with the undepleted pump regime, where only the nonlinear matrix d at the second harmonic frequency plays a role. However, it should be noted that our method and numerical analysis can easily be extended to encompass nonlinear dispersion.

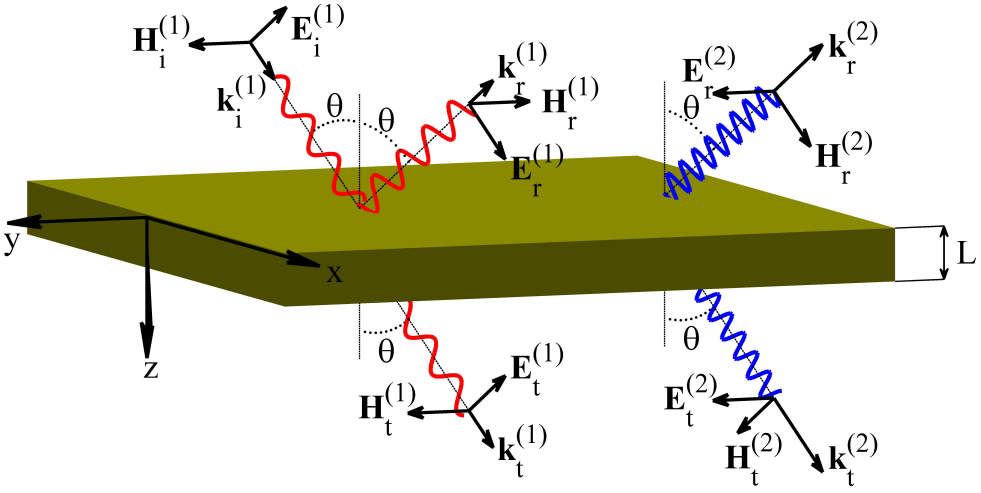

Figure 6.1: Slab and fields geometry for the second harmonic generation process.

6.2.1 Linear slab behavior in the lossless regime

As a prelude to the analysis of the second harmonic process, it is worth discussing the linear slab behavior observable when the optical intensity of the incident fundamental wave is very small. For the purpose of theoretically discussing the basic phenomenology and its underlying mechanism, we consider here an ideal situation where absorption is negligible and we choose $\varepsilon_o^{(1)} = 0.29$ and $\varepsilon_e^{(1)} = -0.03$, and $\lambda^{(1)} = 500\,\text{nm}$. Subsequently, the role played by absorption will be discussed as the imaginary parts of the permittivities are gradually increased, thus approaching more realistic situations. Since the ordinary waves of the slab with wave vectors in the xz plane are polarized along the y axis, in the considered interaction configuration only extraordinary plane waves are excited, with wave vectors $\boldsymbol{k}^{(1)} = k_x^{(1)}\boldsymbol{e}_x + k_z^{(1)}\boldsymbol{e}_z$ satisfying the dispersion relation $[k_x^{(1)}]^2/\varepsilon_e^{(1)} + [k_z^{(1)}]^2/\varepsilon_o^{(1)} = [k^{(1)}]^2$, where $k^{(1)} = 2\pi/\lambda^{(1)}$. By enforcing transverse-momentum conservation across the slab interfaces, i.e., $k_x^{(1)} = k^{(1)}\sin\vartheta$, we readily obtain $k_z^{(1)} = k^{(1)}\sqrt{\varepsilon_o^{(1)}\left[1 - \sin^2\vartheta/\varepsilon_e^{(1)}\right]}$ (A.12).

The slab transmittance $T = |\boldsymbol{E}_t^{(1)}|^2/|\boldsymbol{E}_i^{(1)}|^2$ (where $\boldsymbol{E}_t^{(1)}$ and $\boldsymbol{E}_i^{(1)}$ are the complex electric amplitude of transmitted and incident waves, respectively; see ***Fig.6.1***) is easily evaluated by adopting the same procedure used to deal with the standard Fabry-Perot etalon (Chapter 4), where the extraordinary-plane-wave dispersion is

used instead of its isotropic counterpart, and the result is (A.13)

$$T = \frac{1}{\left|\cos(k_z^{(1)}L) - iF\sin(k_z^{(1)}L)\right|^2} \tag{6.2}$$

where

$$F = \frac{1}{2}\left(\frac{k^{(1)}\varepsilon_o^{(1)}\cos\vartheta}{k_z^{(1)}} + \frac{k_z^{(1)}}{k^{(1)}\varepsilon_o^{(1)}\cos\vartheta}\right)$$

In ***Fig.6.2a*** we plot the transmittance T of (6.2) as a function of both the incidence angle ϑ and the slab thickness L in the range $0 < L < 500\,\text{nm} = \lambda^{(1)}$. From the plots we note that the slab is mostly opaque to the considered radiation ($T \ll 1$) except around very specific incidence angles (dependent on the slab thickness) at which it is completely transparent. From (6.2) it is evident that the slab is fully transparent ($T = 1$) if $k_z^{(1)}L = m\pi$ and the ensuing curves of complete transparency are reported as dashed lines along the top plane of ***Fig.6.2a***. From a physical point of view, full slab transparency occurs when the impinging wave couples to one of the slab standing waves (responsible for the etalon resonances) and, as discussed in Chapter 4, such standing waves exist even within a subwavelength-thick slab since the medium is hyperbolic (indefinite) with permittivities of moduli smaller than 1. Note that if $k_z^{(1)}L$ is slightly different from $m\pi$, the denominator in (6.2) is dominated by the term containing F (since $|F| \approx |\varepsilon_o^{(1)}|^{-1} \gg 1$) so that the overall transmissivity turns out to be proportional to $|\varepsilon_o^{(1)}|$, thus explaining the sharpness of the ridges of T (see ***Fig.6.2a***) located at the curves of complete transparency.

In ***Fig.6.2b*** we plot the longitudinal field enhancement factor

$$\Gamma = \frac{|\boldsymbol{e}_z \cdot \boldsymbol{E}^{(1)}(0^+)|}{|\boldsymbol{e}_z \cdot \boldsymbol{E}_i^{(1)}|},$$

defined as the ratio between the modulus of the field perpendicular to the slab within the medium just across the interface $z = 0$ (see ***Fig.6.1***) and the modulus of the longitudinal field of the sole incident fundamental wave. Note that, corresponding to the curves of complete slab transparency, the field enhancement factor reaches its maximum value $\Gamma = 33.33 = 1/|\varepsilon_e^{(1)}|$. This is easily understood from one of the field-matching conditions at the interface $z = 0$ (continuity of the normal component

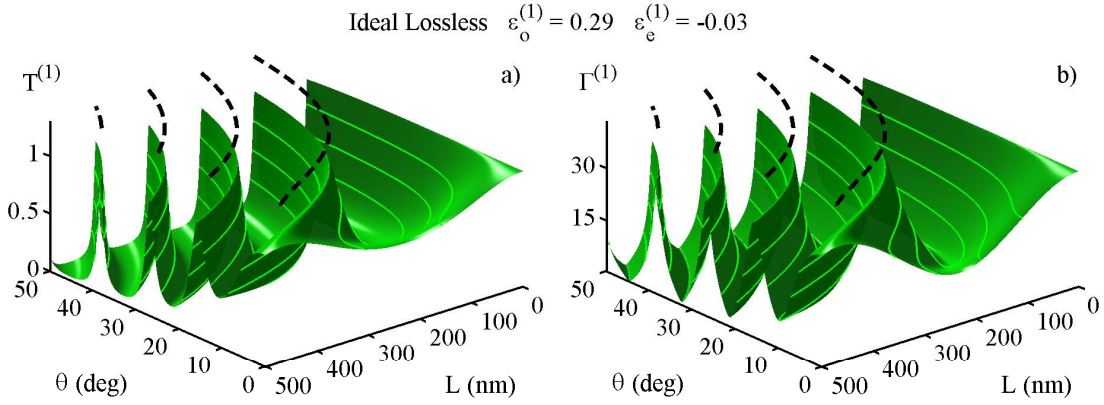

Figure 6.2: Linear slab transmissivity T (a) and longitudinal field enhancement factor Γ (b) for ideal situation of lossless propagation $\varepsilon_o^{(1)} = 0.29$ and $\varepsilon_e^{(1)} = -0.03$. The dashed lines along the top planes in (a) and (b) represent the full transparency curves of the linear slab, $k_z^{(1)} L = m\pi$, for various m.

of the electric displacement field, i.e., $\boldsymbol{e}_z \cdot (\boldsymbol{E}_i^{(1)} + \boldsymbol{E}_r^{(1)}) = \varepsilon_e^{(1)} \left[\boldsymbol{e}_z \cdot \boldsymbol{E}^{(1)}(0^+)\right]$) since when $T = 1$ no reflected wave is generated (i.e., $\boldsymbol{E}_r^{(1)} = 0$), so that

$$\boldsymbol{e}_z \cdot \boldsymbol{E}^{(1)}(0^+) = \frac{1}{\varepsilon_e^{(1)}} \boldsymbol{e}_z \cdot \boldsymbol{E}_i^{(1)} .$$

We conclude that the considered slab provides a powerful mechanism for attaining a strong enhancement (amounting to $1/|\varepsilon_e^{(1)}| \gg 1$) of the longitudinal field.

6.2.2 Linear slab behavior in the weak-absorption regime

The occurrence of the slab resonances described above (with ensuing full slab transparency and longitudinal field enhancement) is inherently a coherent phenomenon so that it is worth discussing here the effect of the unavoidable medium losses which generally play a very important (and usually detrimental) role when the permittivity amplitudes are smaller than 1. In order to discuss more realistic situations than the ideal one reported in ***Fig.6.2a*** and ***Fig.6.2b*** (where the imaginary parts of the permittivities exactly vanish), we here consider a slab filled by a medium with permittivities $\varepsilon_o^{(1)} = 0.29 + 0.001i$ and $\varepsilon_e^{(1)} = -0.03 + 0.001i$ (at $\lambda^{(1)} = 500\,\mathrm{nm}$), for which the slab transmittance T and the field enhancement factor Γ are reported in ***Fig.6.3a*** and ***Fig.6.3b***, respectively. Comparing ***Fig.6.2a*** and ***Fig.6.2b*** with

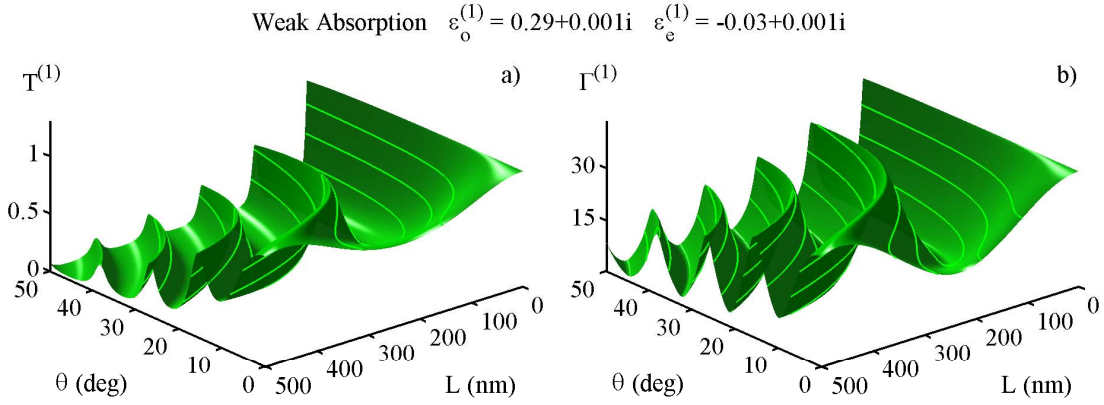

Figure 6.3: Linear slab transmissivity T (a) and longitudinal field enhancement factor Γ (b) for weak-absorption regime $\varepsilon_o^{(1)} = 0.29{+}0.001i$ and $\varepsilon_e^{(1)} = -0.03{+}0.001i$.

Fig.6.3a and ***Fig.6.3b***, we note that the overall electromagnetic phenomenology is unaltered since both T and Γ exhibit sharp peaks, the most striking difference being the global decrease of the peak heights and their dependence on both ϑ and L. This happens since the imaginary parts of the permittivities are considerably smaller then the real parts (weak-absorption regime), so that the coherent mechanism supporting etalon resonances discussed above is not fully ruled out by absorption. Specifically, the included weak absorption prevents slab reflection from exactly vanishing since it forbids fully coherent compensation between forward and backward waves traveling within the slab (they exhibit evanescent tails). As a consequence, the slab is never fully transparent ($T \neq 1$) and the enhancement factor is never strictly equal to $1/|\varepsilon_e^{(1)}|$. This is an interesting situation since the main features of the coherent phenomenology are not lost and, as will be proved, a nanocomposite exhibiting the required dielectric tensor can be designed by resorting to gain media for achieving partial loss compensation.

6.2.3 Linear slab behavior in the strong-absorption regime

In order to further investigate the role played by absorption, we now consider a slab filled by a medium with permittivities $\varepsilon_o^{(1)} = 0.29 + 0.015i$ and $\varepsilon_e^{(1)} = -0.03 + 0.015i$ (at $\lambda^{(1)} = 500\,\text{nm}$) for which the slab transmittance T and the

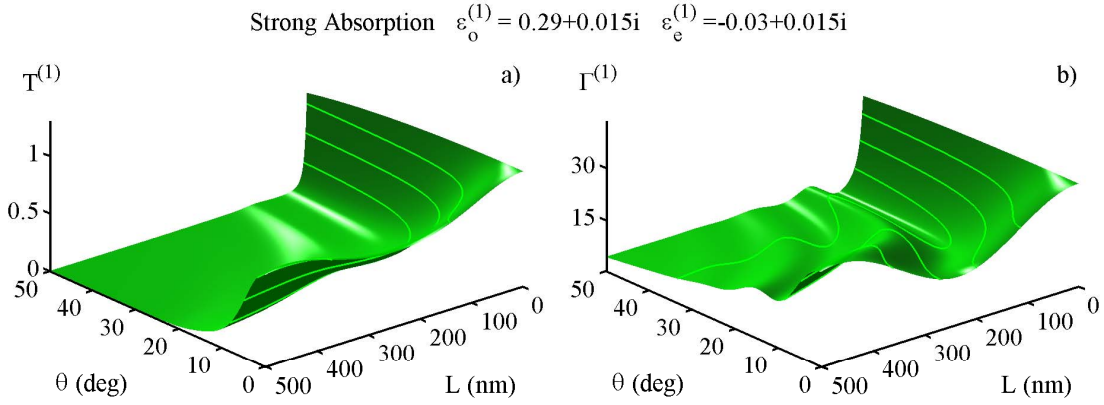

Figure 6.4: Linear slab transmissivity T (a) and longitudinal field enhancement factor Γ (b) for strong-absorption regime $\varepsilon_o^{(1)} = 0.29 + 0.015i$ and $\varepsilon_e^{(1)} = -0.03 + 0.015i$.

field enhancement factor Γ are reported in ***Fig.6.4a*** and ***Fig.6.4b***, respectively. It is evident that the etalon resonances are almost totally ruled out by absorption, and the field enhancement factor also does not show pronounced peaks. This is a consequence of the fact that, in this situation, the imaginary parts of the permittivities are comparable with the real parts (strong-absorption regime) so that evanescently fading counterpropagating waves within the slab are not able to set up the coherent mechanism producing etalon resonances described above. However, from ***Fig.6.4b*** it is evident that a reduced enhancement of the longitudinal field survives in the strong-absorption regime, and this is important since, as we will show, a nanocomposite medium exhibiting the required dielectric tensor can be designed even without the use of gain media.

6.3 Second harmonic generation process

In order to discuss the second harmonic generation process we consider the Maxwell's curl equations in a dielectric non-magnetic homogeneous anisotropic non-

linear medium

$$\begin{cases} \boldsymbol{\nabla} \times \boldsymbol{E} = -\mu_0 \dfrac{\partial \boldsymbol{H}}{\partial t} \\ \boldsymbol{\nabla} \times \boldsymbol{H} = \dfrac{\partial \boldsymbol{D}}{\partial t} + \dfrac{\partial \boldsymbol{P}_{NL}}{\partial t} \end{cases} \tag{6.3}$$

where the electric displacement $\boldsymbol{D}$ is related to linear electric polarization by constitutive relation through electric susceptibility linear tensor $\chi^{(1)}$ or dielectric permittivity tensor ε

$$\boldsymbol{D} = \varepsilon_0 \boldsymbol{E} + \boldsymbol{P}_L = \varepsilon_0 (\mathbb{1} + \chi^{(1)}) \boldsymbol{E} = \varepsilon_0 \varepsilon \boldsymbol{E}$$

and P_{NL} is the nonlinear electric polarization. We write the electric and magnetic fields as superposition of higher harmonics

$$\begin{cases} \boldsymbol{E}(\boldsymbol{r}, t) = \dfrac{1}{2} \displaystyle\sum_{n=-\infty}^{\infty} \boldsymbol{E}^{(n)}(\boldsymbol{r}) e^{-in\omega t} \\ \boldsymbol{H}(\boldsymbol{r}, t) = \dfrac{1}{2} \displaystyle\sum_{n=-\infty}^{\infty} \boldsymbol{H}^{(n)}(\boldsymbol{r}) e^{-in\omega t} \end{cases}$$

where $\boldsymbol{E}^{(-n)} = \boldsymbol{E}^{(n)*}$ and $\boldsymbol{H}^{(-n)} = \boldsymbol{H}^{(n)*}$. Using this definitions, for the quantities related to the linear polarization we have

$$\boldsymbol{D}(\boldsymbol{r}, t) = \varepsilon_0 \boldsymbol{E}(\boldsymbol{r}, t) + \boldsymbol{P}_L(\boldsymbol{r}, t) = \frac{1}{2} \varepsilon_0 \sum_{n=-\infty}^{\infty} \left[\varepsilon_{ij}^{(n)} E_j^{(n)}(\boldsymbol{r}) \boldsymbol{e}_i \right] e^{-in\omega t} ,$$

where $\varepsilon_{ij}^{(n)}$ is the ij-th element of the dielectric permittivity tensor at frequency $n\omega$, and considering a quadratic nonlinearity we get

$$\begin{aligned} \boldsymbol{P}_{NL}(\boldsymbol{r}, t) = \varepsilon_0 \chi_{ijk}^{(2)} E_j(\boldsymbol{r}, t) E_k(\boldsymbol{r}, t) \boldsymbol{e}_i = \\ = \varepsilon_0 \chi_{ijk}^{(2)} \sum_{n=-\infty}^{\infty} \sum_{m=-\infty}^{\infty} E_j(\boldsymbol{r})^{(n)} E_k(\boldsymbol{r})^{(m)} e^{-i(m+n)\omega t} \boldsymbol{e}_i = \\ = \frac{1}{2} \sum_{n=-\infty}^{\infty} \left[\frac{1}{2} \varepsilon_0 \chi_{ijk}^{(2)} \sum_{m=-\infty}^{\infty} E_j(\boldsymbol{r})^{(n-m)} E_k(\boldsymbol{r})^{(m)} \right] e^{-in\omega t} \boldsymbol{e}_i \, . \end{aligned}$$

Therefore, Maxwell's equations (6.3) for each harmonic are

$$\begin{cases} \boldsymbol{\nabla} \times \boldsymbol{E}^{(n)}(\boldsymbol{r}) = in\omega\mu_0 \boldsymbol{H}^{(n)}(\boldsymbol{r}) \\ \boldsymbol{\nabla} \times \boldsymbol{H}^{(n)}(\boldsymbol{r}) = -in\omega\varepsilon_0 \left[\varepsilon_{ij}^{(n)} E_j(\boldsymbol{r})^{(n)} + \dfrac{1}{2} \chi_{ijk}^{(2)} \displaystyle\sum_{m=-\infty}^{\infty} E_j(\boldsymbol{r})^{(n-m)} E_k(\boldsymbol{r})^{(m)} \right] \boldsymbol{e}_i \end{cases}$$

Substituting $\chi^{(2)}_{ijk}/2$ with the elements of quadratic nonlinear d matrix (d_{ijk}), considering the optical principal axes as the reference frame ($\varepsilon^{(1)}_{ij} = \varepsilon^{(1)}_{i}\delta_{ij}$ and $\varepsilon^{(2)}_{ij} = \varepsilon^{(2)}_{i}\delta_{ij}$) and limiting our argument to the fundamental frequency and to the second harmonic, the equations are

$$\begin{cases} \boldsymbol{\nabla} \times \boldsymbol{E}^{(1)}(\boldsymbol{r}) = in\omega\mu_0 \boldsymbol{H}^{(1)}(\boldsymbol{r}) \\ \boldsymbol{\nabla} \times \boldsymbol{H}^{(1)}(\boldsymbol{r}) = -i\omega\varepsilon_0 \left\{ \varepsilon^{(1)}_i E_i(\boldsymbol{r})^{(1)} + \dots \right. \\ \qquad \left. \dots + d_{ijk} \left[E_j(\boldsymbol{r})^{(1)*} E_k(\boldsymbol{r})^{(2)} + E_j(\boldsymbol{r})^{(2)} E_k(\boldsymbol{r})^{(1)*} \right] \right\} \boldsymbol{e}_i \end{cases}$$

for the first one

$$\begin{cases} \boldsymbol{\nabla} \times \boldsymbol{E}^{(2)}(\boldsymbol{r}) = in\omega\mu_0 \boldsymbol{H}^{(2)}(\boldsymbol{r}) \\ \boldsymbol{\nabla} \times \boldsymbol{H}^{(2)}(\boldsymbol{r}) = -i2\omega\varepsilon_0 \left\{ \varepsilon^{(2)}_i E_i(\boldsymbol{r})^{(2)} + d_{ijk} \left[E_j(\boldsymbol{r})^{(1)} E_k(\boldsymbol{r})^{(1)} \right] \right\} \boldsymbol{e}_i \end{cases}$$

for the second.

We note that the incident p-polarized fundamental wave (see ***Fig.6.1***) couples, within the slab, with the transverse magnetic (TM) fundamental field

$$\begin{cases} \boldsymbol{E}^{(1)} = e^{ik^{(1)}x\sin\vartheta} \left[E^{(1)}_x(z)\boldsymbol{e}_x + E^{(1)}_z(z)\boldsymbol{e}_z \right] \\ \boldsymbol{H}^{(1)} = e^{ik^{(1)}x\sin\vartheta} \left[H^{(1)}_y(z)\boldsymbol{e}_y \right] \end{cases} \tag{6.4}$$

which in turn, as a consequence of the quadratic nonlinear response characterized by the d matrix of (6.1), produces the transverse electric (TE) second-harmonic field

$$\begin{cases} \boldsymbol{E}^{(2)} = e^{i2k^{(1)}x\sin\vartheta} \left[E^{(2)}_y(z)\boldsymbol{e}_y \right] \\ \boldsymbol{H}^{(2)} = e^{i2k^{(1)}x\sin\vartheta} \left[H^{(2)}_x(z)\boldsymbol{e}_x + H^{(2)}_z(z)\boldsymbol{e}_z \right] \end{cases} \tag{6.5}$$

where we have assumed $e^{-i\omega t}$ and $e^{-i2\omega t}$ as time factors for the fundamental wave and the second harmonic wave fields, respectively ($\omega = ck^{(1)}$). This happens since the electric displacement fields within the slab, in the presence of the fields of (6.4) (neglecting the generation of higher harmonics), are

$$\boldsymbol{D}^{(1)} = e^{ik^{(1)}x\sin\vartheta}\varepsilon_0 \left[\varepsilon^{(1)}_o E^{(1)}_x \boldsymbol{e}_x + \left(\varepsilon^{(1)}_e E^{(1)}_z + 2\Delta E^{(1)*}_z E^{(2)}_y \right) \boldsymbol{e}_z \right] ,$$

$$\boldsymbol{D}^{(2)} = e^{i2k^{(1)}x\sin\vartheta}\varepsilon_0 \left[\varepsilon^{(2)}_o E^{(2)}_y + \Delta E^{(1)2}_z \right] \boldsymbol{e}_y ,$$

which are compatible with the structure of TE second harmonic field (6.5). The second-harmonic TE field within the slab matches the s-polarized reflected and transmitted plane second harmonic waves (see ***Fig.6.1***) which are consequently scattered by the slab as a consequence of its illumination by the plane fundamental wave.

The coupled sets of Maxwell's equations for the fundamental wave and the second harmonic one yield

$$\begin{cases} \dfrac{dE_x^{(1)}}{dz} = i\left[k^{(1)}\sin\vartheta E_z^{(1)} + \omega\mu_0 H_y^{(1)}\right] \\ \dfrac{dH_y^{(1)}}{dz} = i\omega\varepsilon_0\varepsilon_o^{(1)} E_x^{(1)} \\ k^{(1)}\sin\vartheta H_y^{(1)} + \omega\varepsilon_0\left[\varepsilon_e^{(1)} E_z^{(1)} + 2\Delta E_z^{(1)*} E_y^{(2)}\right] = 0 \\ \dfrac{dE_y^{(2)}}{dz} = -2i\omega\mu_0 H_x^{(2)} \\ \dfrac{dH_x^{(2)}}{dz} = 2ik^{(1)}\sin\vartheta H_z^{(2)} - 2i\omega\varepsilon_0\left[\varepsilon_o^{(2)} E_y^{(2)} + \Delta E_z^{(1)2}\right] \\ k^{(1)}\sin\vartheta E_y^{(2)} - \omega\mu_0 H_z^{(2)} = 0 \end{cases} \tag{6.6}$$

which is a system of ordinary differential equations for the z dependent amplitudes of the fields of (6.4) and (6.5).

Defining dimensionless quantities

$$\begin{cases} E_x^{(1)}(x,z) = \dfrac{1}{2\Delta} e^{i\xi\sin\vartheta} A_x^{(1)}(\zeta) \\ H_y^{(1)}(x,z) = \dfrac{1}{2\Delta}\sqrt{\dfrac{\varepsilon_0}{\mu_0}} e^{i\xi\sin\vartheta} A_y^{(1)}(\zeta) \\ E_z^{(1)}(x,z) = \dfrac{1}{2\Delta} e^{i\xi\sin\vartheta} A_z^{(1)}(\zeta) \end{cases} \qquad \begin{cases} H_x^{(2)}(x,z) = \dfrac{1}{2\Delta}\sqrt{\dfrac{\varepsilon_0}{\mu_0}} e^{2i\xi\sin\vartheta} A_x^{(2)}(\zeta) \\ E_y^{(2)}(x,z) = \dfrac{1}{2\Delta} e^{2i\xi\sin\vartheta} A_y^{(2)}(\zeta) \\ H_z^{(2)}(x,z) = \dfrac{1}{2\Delta}\sqrt{\dfrac{\varepsilon_0}{\mu_0}} e^{2i\xi\sin\vartheta} A_z^{(2)}(\zeta) \end{cases}$$

where $\xi = (\omega/c)x = k^{(1)}x$, $\zeta = (\omega/c)z = k^{(1)}z$ and $\Lambda = (\omega/c)L = k^{(1)}L$, the

dimensionless equations (6.6)

$$\begin{cases} \dfrac{dA_x^{(1)}}{d\zeta} = i\left[A_y^{(1)} + \sin\vartheta A_z^{(1)}\right] \\ \dfrac{dA_y^{(1)}}{d\zeta} = i\varepsilon_o^{(1)} A_x^{(1)} \\ \sin\vartheta A_y^{(1)} + \varepsilon_e^{(1)} A_z^{(1)} + A_z^{(1)*} A_y^{(2)} = 0 \\ \dfrac{dA_y^{(2)}}{d\zeta} = -2iA_x^{(2)} \\ \dfrac{dA_x^{(2)}}{d\zeta} = -2i\left[\varepsilon_o^{(2)} A_y^{(2)} - \sin\vartheta A_z^{(2)} + \dfrac{1}{2} A_z^{(1)2}\right] \\ \sin\vartheta A_y^{(2)} - A_z^{(2)} = 0 \end{cases} \tag{6.7}$$

In order to describe the scattering of second harmonic fields discussed above, this system has to be supplied with the standard electromagnetic matching conditions at $\zeta = 0$ and $\zeta = \Lambda$ (continuity of the electric and magnetic tangential field components) with the additional requirement that the amplitude of the second harmonic wave impinging from vacuum (for $\zeta < 0$) vanishes. Outside the slab $\zeta < 0$ and $\zeta > \Lambda$, the fields can be written as

$$\zeta < 0 \begin{cases} \begin{pmatrix} A_x^{(1)} \\ A_y^{(1)} \\ A_z^{(1)} \end{pmatrix} = e^{i\zeta\cos\vartheta} \begin{pmatrix} \cos\vartheta \\ 1 \\ -\sin\vartheta \end{pmatrix} Q_I^{(1)} + e^{-i\zeta\cos\vartheta} \begin{pmatrix} \cos\vartheta \\ -1 \\ \sin\vartheta \end{pmatrix} Q_R^{(1)} \\ \begin{pmatrix} A_x^{(2)} \\ A_y^{(2)} \\ A_z^{(2)} \end{pmatrix} = e^{-2i\zeta\cos\vartheta} \begin{pmatrix} \cos\vartheta \\ 1 \\ \sin\vartheta \end{pmatrix} Q_R^{(2)} \end{cases}$$

where $Q_I^{(1)}$ and $Q_R^{(1)}$ are the incident and reflected dimensionless amplitude of fundamental wave and $Q_R^{(2)}$ is the backward-scattered adimentional amplitude of second

harmonic wave ($Q_I^{(2)} = 0$, the sole incident field is the fundamental harmonic),

$$\zeta > \Lambda \begin{cases} \begin{pmatrix} A_x^{(1)} \\ A_y^{(1)} \\ A_z^{(1)} \end{pmatrix} = e^{i\zeta\cos\vartheta} \begin{pmatrix} \cos\vartheta \\ 1 \\ -\sin\vartheta \end{pmatrix} Q_T^{(1)} \\ \begin{pmatrix} A_x^{(2)} \\ A_y^{(2)} \\ A_z^{(2)} \end{pmatrix} = e^{2i\zeta\cos\vartheta} \begin{pmatrix} -\cos\vartheta \\ 1 \\ \sin\vartheta \end{pmatrix} Q_T^{(2)} \end{cases}$$

where $Q_T^{(1)}$ is the transmitted dimensionless amplitude of fundamental wave and $Q_T^{(2)}$ is the forward-scattered dimensionless amplitude of second harmonic wave. The field-matching conditions at the slab's edges are

$$\begin{cases} A_x^{(1)}(0) = \cos\vartheta\left[Q_I^{(1)} + Q_R^{(1)}\right] \\ A_y^{(1)}(0) = Q_I^{(1)} - Q_R^{(1)} \\ A_x^{(1)}(\Lambda) = \cos\vartheta e^{i\Lambda\cos\vartheta} Q_T^{(1)} \\ A_y^{(1)}(\Lambda) = e^{i\Lambda\cos\vartheta} Q_T^{(1)} \end{cases} \quad \begin{cases} A_x^{(2)}(0) = \cos\vartheta Q_R^{(2)} \\ A_y^{(2)}(0) = Q_R^{(2)} \\ A_x^{(2)}(\Lambda) = -\cos\vartheta e^{2i\Lambda\cos\vartheta} Q_T^{(2)} \\ A_y^{(2)}(\Lambda) = e^{2i\Lambda\cos\vartheta} Q_T^{(2)} \end{cases}$$

Manipulating the boundary conditions we get

$$\begin{cases} A_x^{(1)}(0) + \cos\vartheta A_y^{(1)}(0) - 2\cos\vartheta Q_I^{(1)} = 0 \\ A_x^{(1)}(\Lambda) - \cos\vartheta A_y^{(1)}(\Lambda) = 0 \end{cases} \quad \begin{cases} A_x^{(2)}(0) - \cos\vartheta A_y^{(2)}(0) = 0 \\ A_x^{(2)}(\Lambda) + \cos\vartheta A_y^{(2)}(\Lambda) = 0 \end{cases}$$

which solely depend on $Q_I^{(1)}$ which is the known amplitude of the incident fundamental field.

Therefore, for the fundamental harmonic we have

$$\begin{cases} \dfrac{dA_x^{(1)}}{d\zeta} = i\left[A_y^{(1)} + \sin\vartheta A_z^{(1)}\right] \\ \dfrac{dA_y^{(1)}}{d\zeta} = i\varepsilon_o^{(1)} A_x^{(1)} \\ \sin\vartheta A_y^{(1)} + \varepsilon_e^{(1)} A_z^{(1)} + A_z^{(1)*} A_y^{(2)} = 0 \\ A_x^{(1)}(0) + \cos\vartheta A_y^{(1)}(0) - 2\cos\vartheta Q_I^{(1)} = 0 \\ A_x^{(1)}(\Lambda) - \cos\vartheta A_y^{(1)}(\Lambda) = 0 \end{cases} \tag{6.8}$$

and for the second harmonic wave we get

$$\begin{cases} \dfrac{dA_x^{(2)}}{d\zeta} = -2i\left[\varepsilon_o^{(2)} A_y^{(2)} - \sin\vartheta A_z^{(2)} + \dfrac{1}{2}A_z^{(1)2}\right] \\ \dfrac{dA_y^{(2)}}{d\zeta} = -2iA_x^{(2)} \\ \sin\vartheta A_y^{(2)} - A_z^{(2)} = 0 \\ A_x^{(2)}(0) - \cos\vartheta A_y^{(2)}(0) = 0 \\ A_x^{(2)}(\Lambda) + \cos\vartheta A_y^{(2)}(\Lambda) = 0 \end{cases} \tag{6.9}$$

Considering a slab with nonlinear coefficient $\Delta = 140\,\mathrm{pm/V}$ and illuminated by an incident fundamental wave, at $\lambda^{(1)} = 500\,\mathrm{nm}$, of optical intensity $I_i^{(1)} = 1/2\sqrt{\varepsilon_0/\mu_0}|\boldsymbol{E}_i^{(1)}|^2 = 4\,\mathrm{MW/cm^2}$, we have numerically solved the electromagnetic boundary-value problem ((6.8) and (6.9)) by means of a suitable relaxation method and, consequently, we have evaluated the slab efficiencies $\eta_R^{(2)} = |\boldsymbol{E}_r^{(2)}|^2/|\boldsymbol{E}_i^{(1)}|^2$ and $\eta_T^{(2)} = |\boldsymbol{E}_t^{(2)}|^2/|\boldsymbol{E}_i^{(1)}|^2$ of converting the incident fundamental wave into reflected (for $z < 0$) and transmitted (for $z > L$) second harmonic waves, for a number of slabs with different linear properties and for various incidence angles ϑ and slab thicknesses L.

6.3.1 Relaxation iterative method

Relaxation is an iterative method used in numerical computing for solving both linear and nonlinear vector equations. Let us consider the equation $\Theta(X) = 0$ where X is vector with N entries and $\Theta(X)$ is a vector function. To solve the system we use a trial solution $X = X_0 + dX$ where X_0 is a known guess solution and dX is regarded as a small correction so that

$$\Theta(X) = \Theta(X_0 + dX) \simeq \Theta(X_0) + JdX = 0\,, \tag{6.10}$$

where J is the Jacobian matrix of first-order partial derivates $J_{ij} = \partial\Theta_i/\partial X_j$. From (6.10) we get

$$dX = -J^{-1}\Theta(X_0)\,,$$

so that, if $|dX|$ is smaller than the prescribed tolerance then X_0 is the acceptable solution of (6.10), otherwise we set $X_0 + dX$ for the guess solution and we use (6.10) again to evaluate its correction. The procedure is iterated so that if $X_0^{(k)}$ is the guess solution at n-th iteration then the guess solution at the next $(k+1)$-th iteration is $X_0^{(n+1)} = X_0^{(k)} + dX^{(k)}$, and it iteration stops when $|dX|$ is smaller than the prescribed tolerance.

Numerical discretization procedure

We have subdivided the ζ range ($0 < \zeta < \Lambda$, $d\zeta = \Lambda/n$) into n parts so that the $N = 12n$ unknown entries of the vector X (it is here necessary to also consider the complex conjugate of the entries as independent quantities) are

$$\begin{cases} A_x^{(1)} = X_{1\ldots n} \\ A_y^{(1)} = X_{n+1\ldots 2n} \\ A_z^{(1)} = X_{2n+1\ldots 3n} \end{cases} \quad \begin{cases} A_x^{(2)} = X_{3n+1\ldots 4n} \\ A_y^{(2)} = X_{4n+1\ldots 5n} \\ A_z^{(2)} = X_{5n+1\ldots 6n} \end{cases}$$

$$\begin{cases} A_x^{(1)*} = X_{6n+1\ldots 7n} \\ A_y^{(1)*} = X_{7n+1\ldots 8n} \\ A_z^{(1)*} = X_{8n+1\ldots 9n} \end{cases} \quad \begin{cases} A_x^{(2)*} = X_{9n+1\ldots 10n} \\ A_y^{(2)*} = X_{10n+1\ldots 11n} \\ A_z^{(2)*} = X_{11n+1\ldots 12n} \end{cases} .$$

The discretized version of the electromagnetic boundary-value problem (6.8) and

(6.9) reads

$$\begin{cases} A_x^{(1)}(\zeta+d\zeta) - A_x^{(1)}(\zeta) = id\zeta\left[A_y^{(1)}(\zeta) + \sin\vartheta A_z^{(1)}(\zeta)\right] \\ A_x^{(1)}(0) + \cos\vartheta A_y^{(1)}(0) - 2\cos\vartheta Q_I^{(1)} = 0 \\ A_y^{(1)}(\zeta+d\zeta) - A_y^{(1)}(\zeta) = id\zeta\varepsilon_o^{(1)} A_x^{(1)}(\zeta) \\ A_x^{(1)}(\Lambda) - \cos\vartheta A_y^{(1)}(\Lambda) = 0 \\ \sin\vartheta A_y^{(1)}(\zeta) + \varepsilon_e^{(1)} A_z^{(1)}(\zeta) + A_z^{(1)*}(\zeta) A_y^{(2)}(\zeta) = 0 \\ A_x^{(2)}(\zeta+d\zeta) - A_x^{(2)}(\zeta) = -2id\zeta\left[\varepsilon_o^{(2)} A_y^{(2)}(\zeta) - \sin\vartheta A_z^{(2)}(\zeta) + \frac{1}{2} A_z^{(1)2}(\zeta)\right] \\ A_x^{(2)}(0) - \cos\vartheta A_y^{(2)}(0) = 0 \\ A_y^{(2)}(\zeta+d\zeta) - A_y^{(2)}(\zeta) = -2id\zeta A_x^{(2)}(\zeta) \\ A_x^{(2)}(\Lambda) + \cos\vartheta A_y^{(2)}(\Lambda) = 0 \\ \sin\vartheta A_y^{(2)}(\zeta) - A_z^{(2)}(\zeta) = 0 \end{cases}$$

Therefore the N coupled equations for the N unknowns are

$$
\begin{aligned}
&k = 1 \ldots n-1 && \Theta_k = X_k + id\zeta\left[X_{k+n} + \sin\vartheta X_{k+2n}\right] - X_{k+1} = 0\\
&k = n && \Theta_n = X_1 + \cos\vartheta X_{1+n} - 2\cos\vartheta Q_I^{(1)} = 0\\
&k = n+1 \ldots 2n-1 && \Theta_k = X_k + id\zeta\varepsilon_o^{(1)} X_{k-n} - X_{k+1} = 0\\
&k = 2n && \Theta_{2n} = X_n - \cos\vartheta X_{2n} = 0\\
&k = 2n+1 \ldots 3n && \Theta_k = \sin\vartheta X_{k-n} + \varepsilon_e^{(1)} X_k + X_{k+2n} X_{k+6n} = 0\\
&k = 3n+1 \ldots 4n-1 && \Theta_k = X_k - 2id\zeta\left[\varepsilon_o^{(2)} X_{k+n} - \sin\vartheta X_{k+2n} + \frac{1}{2}X_{k-n}^2\right] - X_{k+1}\\
&k = 4n && \Theta_{4n} = X_{1+3n} - \cos\vartheta X_{1+4n} = 0\\
&k = 4n+1 \ldots 5n-1 && \Theta_k = X_k - 2id\zeta X_{k-n} - X_{k+1}\\
&k = 5n && \Theta_{5n} = X_{4n} + \cos\vartheta X_{5n} = 0\\
&k = 5n+1 \ldots 6n && \Theta_k = \sin\vartheta X_{k-n} - X_k = 0\\
&k = 6n+1 \ldots 7n-1 && \Theta_k = X_k - id\zeta\left[X_{k+n} + \sin\vartheta X_{k+2n}\right] - X_{k+1} = 0\\
&k = 7n && \Theta_{7n} = X_{1+6n} + \cos\vartheta X_{1+7n} - 2\cos\vartheta Q_I^{(1)} = 0\\
&k = 7n+1 \ldots 8n-1 && \Theta_k = X_k - id\zeta\varepsilon_o^{(1)} X_{k-n} - X_{k+1} = 0\\
&k = 8n && \Theta_{8n} = X_{7n} - \cos\vartheta X_{8n} = 0\\
&k = 8n+1 \ldots 9n && \Theta_k = \sin\vartheta X_{k-n} + \varepsilon_e^{(1)} X_k + X_{k+2n} X_{k-6n} = 0\\
&k = 9n+1 \ldots 10n-1 && \Theta_k = X_k + 2id\zeta\left[\varepsilon_o^{(2)} X_{k+n} - \sin\vartheta X_{k+2n} + \frac{1}{2}X_{k-n}^2\right] - X_{k+1}\\
&k = 10n && \Theta_{10n} = X_{1+9n} - \cos\vartheta X_{1+10n} = 0\\
&k = 10n+1 \ldots 11n-1 && \Theta_k = X_k + 2id\zeta X_{k-n} - X_{k+1}\\
&k = 11n && \Theta_{11n} = X_{10n} + \cos\vartheta X_{11N} = 0\\
&k = 11n+1 \ldots 12n && \Theta_k = \sin\vartheta X_{k-n} - X_k = 0
\end{aligned}
$$

while the elements of Jacobian matrix $J_{kl} = \partial\Theta_k/\partial X_l$ are

$$
\begin{aligned}
&k = 1 \ldots n-1 && J_{kl} = \delta_{kl} + id\zeta\left[\delta_{(k+n)l} + \sin\vartheta\delta_{(k+2n)l}\right] - \delta_{k(l+1)} = 0\\
&k = n && J_{nl} = \delta_{1l} + \cos\vartheta\delta_{(1+n)l} - 2\cos\vartheta Q_I^{(1)} = 0\\
&k = n+1 \ldots 2n-1 && J_{kl} = \delta_{kl} + id\zeta\varepsilon_o^{(1)}\delta_{(k-n)l} - \delta_{(k+1)l} = 0\\
&k = 2n && J_{(2n)l} = \delta_{nl} - \cos\vartheta\delta_{(2n)l} = 0\\
&k = 2n+1 \ldots 3n && J_{kl} = \sin\vartheta\delta_{(k-n)l} + \varepsilon_e^{(1)}\delta_{kl} + X_{(k+6n)l}\delta_{(k+2n)l} +\\
& && + X_{(k+2n)l}\delta_{(k+6n)l} = 0\\
&k = 3n+1 \ldots 4n-1 && J_{kl} = \delta_{kl} - 2id\zeta\left[\varepsilon_o^{(2)}\delta_{(k+n)l} - \sin\vartheta\delta_{(k+2n)l} +\right.\\
& && \left. + X_{k-n}\delta_{(k-n)l}\right] - \delta_{(k+1)l}\\
&k = 4n && J_{(4n)l} = \delta_{(1+3n)l} - \cos\vartheta\delta_{(1+4n)l} = 0\\
&k = 4n+1 \ldots 5n-1 && J_{kl} = \delta_{kl} - 2id\zeta\delta_{(k-n)l} - \delta_{(k+1)l}\\
&k = 5n && J_{(5n)l} = \delta_{(4n)l} + \cos\vartheta\delta_{(5n)l} = 0\\
&k = 5n+1 \ldots 6n && J_{kl} = \sin\vartheta\delta_{(k-n)l} - \delta_{kl} = 0\\
&k = 6n+1 \ldots 7n-1 && J_{kl} = \delta_{kl} - id\zeta\left[\delta_{(k+n)l} + \sin\vartheta\delta_{(k+2n)l}\right] - \delta_{(k+1)l} = 0\\
&k = 7n && J_{(7n)l} = \delta_{(1+6n)l} + \cos\vartheta\delta_{(1+7n)l} - 2\cos\vartheta Q_I^{(1)} = 0\\
&k = 7n+1 \ldots 8n-1 && J_{kl} = \delta_{kl} - id\zeta\varepsilon_o^{(1)}\delta_{(k-n)l} - \delta_{(k+1)l} = 0\\
&k = 8n && J_{(8n)l} = \delta_{(7n)l} - \cos\vartheta\delta_{(8n)l} = 0\\
&k = 8n+1 \ldots 9n && J_{kl} = \sin\vartheta\delta_{(k-n)l} + \varepsilon_e^{(1)}\delta_{kl} + X_{k-6n}\delta_{k+2n} +\\
& && + X_{k+2n}\delta_{k-6n} = 0\\
&k = 9n+1 \ldots 10n-1 && J_{kl} = \delta_{kl} + 2id\zeta\left[\varepsilon_o^{(2)}\delta_{(k+n)l} - \sin\vartheta\delta_{(k+2n)l} +\right.\\
& && \left. + X_{k-n}\delta_{(k-n)l}\right] - \delta_{(k+1)l}\\
&k = 10n && J_{(10n)l} = \delta_{(1+9n)l} - \cos\vartheta\delta_{(1+10n)l} = 0\\
&k = 10n+1 \ldots 11n-1 && J_{kl} = \delta_{kl} + 2id\zeta\delta_{(k-n)l} - \delta_{(k+1)l}\\
&k = 11n && J_{(11n)l} = \delta_{(10n)l} + \cos\vartheta\delta_{(11N)l} = 0\\
&k = 11n+1 \ldots 12n && J_{kl} = \sin\vartheta\delta_{(k-n)l} - \delta_{kl} = 0
\end{aligned}
$$

where δ_{ij} is the Kronecker delta.

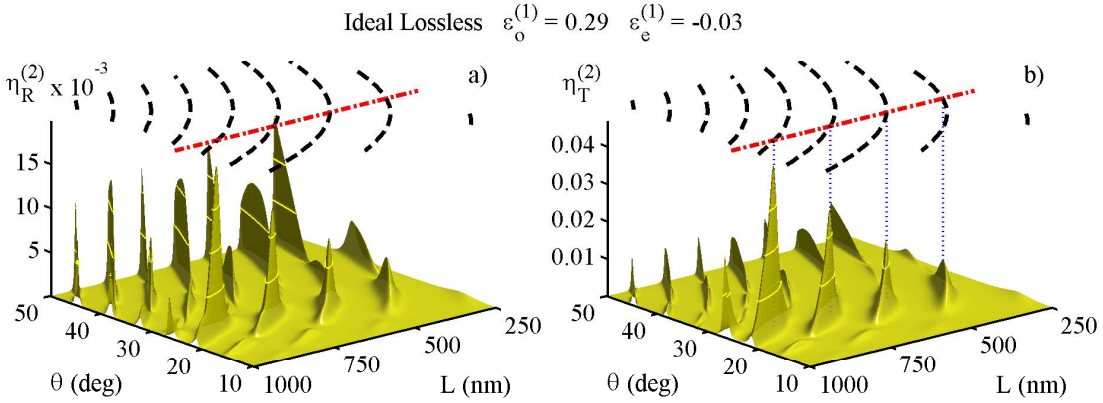

Figure 6.5: Second harmonic generation slab efficiencies $\eta_R^{(2)}$ (a) and $\eta_T^{(2)}$ (b) of converting the incident fundamental wave into backward- and forward-scattered second harmonic waves, respectively, evaluated for the optical intensity $I_i^{(1)} = 4\,\mathrm{MW/cm^2}$ of the incident fundamental wave in the ideal situation of lossless propagation with $\varepsilon_o^{(1)} = 0.29$, $\varepsilon_e^{(1)} = -0.03$ and $\varepsilon_o^{(2)} = 2.26$. The dashed curves and the dash-dotted lines along the top planes of (a) and (b) represent the curves $k_z^{(1)}L = m\pi$ and the phase-matching angle ϑ_{pm}, respectively.

6.3.2 Second harmonic generation in lossless regime

In ***Fig.6.5a*** and ***Fig.6.5b*** we plot $\eta_R^{(2)}$ and $\eta_T^{(2)}$, respectively, evaluated in an ideal situation of a lossless slab characterized by the permittivities $\varepsilon_o^{(1)} = 0.29$, $\varepsilon_e^{(1)} = -0.03$ and $\varepsilon_o^{(2)} = 2.26$ (note that the considered permittivities for the fundamental wave coincide with those of ***Fig.6.2a*** and ***Fig.6.2b***). It is particularly evident that, for the chosen optical intensity of the incident fundamental wave, second harmonic generation uniquely occurs at the specific incident angles ϑ and slab thicknesses L satisfying the relation $k_z^{(1)}(\vartheta)L = m\pi$, i.e., in conditions of full transparency of the linear slab for the fundamental wave (see the dashed lines along the top planes of ***Fig.6.5a*** and ***Fig.6.5b***). Physically, the fact that the second harmonic wave field scattered by the slab is generally very weak (for the considered intensity $I_i^{(1)}$) is easily grasped by noting that second harmonic generation is here due to the source term proportional to $E_z^{(1)2}$ in the fifth of (6.6), which is generally very small and definitely unable to produce a strong second harmonic signal within the small

thickness of the considered slab. However, such an unattractive scenario is greatly altered if the conditions of full transparency of the slab for the fundamental wave are met, since the enhancement mechanism of the longitudinal field $E_z^{(1)}$ described above produces a strong enhancement of the polarization source term containing $E_z^{(1)2}$, in turn entailing a very pronounced frequency-doubling efficiency (see the sharp ridges of ***Fig.6.5a*** and ***Fig.6.5b*** corresponding to the dashed curves on the top planes). Note that, from ***Fig.6.5a*** and ***Fig.6.5b***, the intensities of the backward and forward second harmonic waves scattered by the slab are roughly at most 10% and 30% of the incident fundamental wave intensity, respectively, and it is worth stressing that these are giant frequency-doubling efficiencies for such a thin slab. ***Fig.6.5b*** also clearly shows that the forward-scattering efficiency of the second harmonic wave is not uniformly large along the curves $k^{(1)}(\vartheta)L = m\pi$ but exhibits its more pronounced peaks around the specific incident angle 25.4°, and this happens since this angle provides phase matching between the fundamental and second harmonic waves. In fact, the wave vector of the second harmonic wave within the slab is $k_z^{(2)} = 2k^{(1)}\sqrt{\varepsilon_o^{(2)} - \sin^2\vartheta}$ (in the **undepleted pump regime**) so that the condition $2k_z^{(1)} = k_z^{(2)}$ yields the phase-matching angle (B.1)

$$\vartheta_{pm} = \arcsin\sqrt{\varepsilon_e^{(1)}\frac{\varepsilon_o^{(1)} - \varepsilon_o^{(2)}}{\varepsilon_o^{(1)} - \varepsilon_e^{1}}} = 25.4^\circ\,,$$

an angle which is reported as the straight dash-dotted line on the top planes of ***Fig.6.5a*** and ***Fig.6.5b*** (note the pronounced peaks of $\eta_T^{(2)}$ of ***Fig.6.5b*** corresponding to the intersection between the dashed curves and the dash-dotted line).

Note that a similar high-efficiency second harmonic generation process has been recently investigated in Ref. [93], where the authors consider a subwavelength-thick slab filled by a quadratically nonlinear medium with isotropic permittivity very close to zero. In Ref. [93] the enhancement mechanism of the longitudinal field component is the same as the one considered in the present paper, but there very high slab transparency for the fundamental wave is achieved by resorting to a very thin slab, whereas in the present paper slab transparency is a consequence of the kind of etalon resonance provided by medium hyperbolicity (indefinite permittivity

tensor). As a consequence, the power of the second harmonic generation process discussed in Ref. [93] cannot be fully exploited because of the required very small slab thickness, a drawback which we avoid in the present paper since slab resonances occur at different and greater slab thicknesses.

6.3.3 Second harmonic generation in the weak-absorption regime

Since the second harmonic gerneration process described above is mainly triggered by a field enhancement mechanism of linear origin and, as discussed in the previous section, material absorption fundamentally affects the linear slab behavior, it is worth discussing here the effect of losses on the second harmonic field scattering. As in the linear case, we here investigate the weak-absorption regime by means of a slab characterized by the permittivities $\varepsilon_o^{(1)} = 0.29{+}0.001i$, $\varepsilon_e^{(1)} = -0.03{+}0.001i$ and $\varepsilon_o^{(2)} = 2.26$ and the same d matrix as above. The corresponding second harmonic generation efficiencies $\eta_R^{(2)}$ and $\eta_T^{(2)}$ are plotted in ***Fig.6.6a*** and ***Fig.6.6b***, from which we note that the overall portraits of backward and forward second harmonic waves scattering globally resemble those pertaining the ideal situation of ***Fig.6.5a*** and ***Fig.6.5b***, with a slight change of the phase-matching angle and with the very important difference that both efficiencies are roughly reduced by a factor of 10. Such phenomenology is consistent with the corresponding linear slab behavior since the peaks of $\eta_R^{(2)}$ and $\eta_T^{(2)}$ of ***Fig.6.6a*** and ***Fig.6.6b*** are located along the ridges of ***Fig.6.3a*** and ***Fig.6.3b*** and, remarkably, since the decrease of second harmonic efficiencies occurs in correspondence with the decrease of the field enhancement factor $\Gamma^{(1)}$, as is evident from a comparison of ***Fig.6.2b*** and ***Fig.6.3b***. Again these are important results since a medium exhibiting such linear and nonlinear optical properties can actually be synthesized by resorting to gain media, thus assuring the feasibility of the discussed phenomenology.

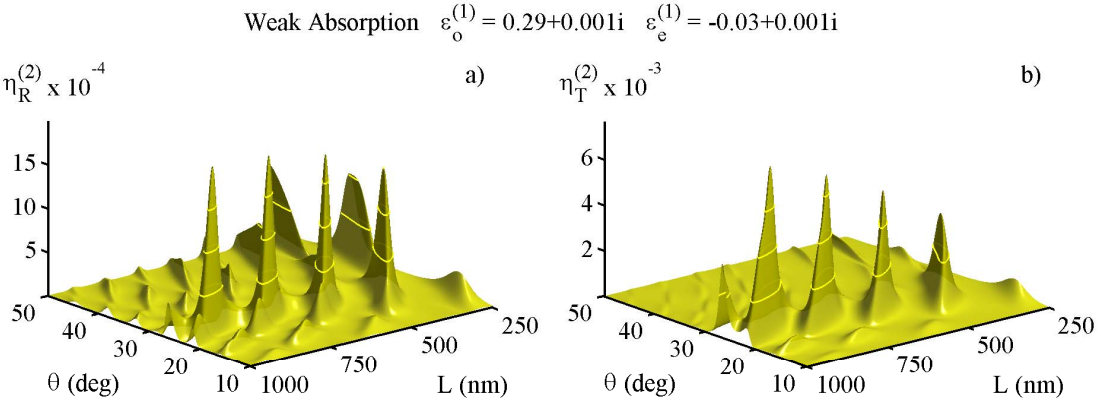

Figure 6.6: Second harmonic generation slab efficiencies $\eta_R^{(2)}$ (a) and $\eta_T^{(2)}$ (b) of converting the incident fundamental wave into backward- and forward-scattered second harmonic waves, respectively, evaluated for the optical intensity $I_i^{(1)} = 4\,\mathrm{MW/cm^2}$ of the incident fundamental wave in the weak-absorption regime with $\varepsilon_o^{(1)} = 0.29 + 0.001i$, $\varepsilon_e^{(1)} = -0.03 + 0.001i$ and $\varepsilon_o^{(2)} = 2.26$.

6.3.4 Second harmonic generation in the strong-absorption regime

In analogy to the linear situation, we now consider a situation of strong absorption by resorting to a slab characterized by the permittivities $\varepsilon_o^{(1)} = 0.29 + 0.015i$, $\varepsilon_e^{(1)} = -0.03 + 0.015i$ and $\varepsilon_o^{(2)} = 2.26$ and the same d matrix as above. The corresponding second harmonic generation efficiencies $\eta_R^{(2)}$ and $\eta_T^{(2)}$ are plotted in ***Fig.6.7a*** and ***Fig.6.7b***, from which it is evident that the second harmonic generation mechanism described above is almost destroyed by material losses since frequency-doubling efficiencies do not exhibit the multipeaked structures. The residual of the phenomenology described above is a single wide peak located at an angle close to the phase-matching angle of ***Fig.6.5b*** and ***Fig.6.6b***, a peak providing second harmonic generation efficiencies three and two orders of magnitude smaller than those pertaining to the ideal and the weak-absorption situations, respectively. Again, this phenomenology is compatible with the linear slab behavior reported in ***Fig.6.4a*** and ***Fig.6.4b*** where, as discussed in the preceding section, slab resonances are almost ruled out by material losses. However, the second harmonic generation

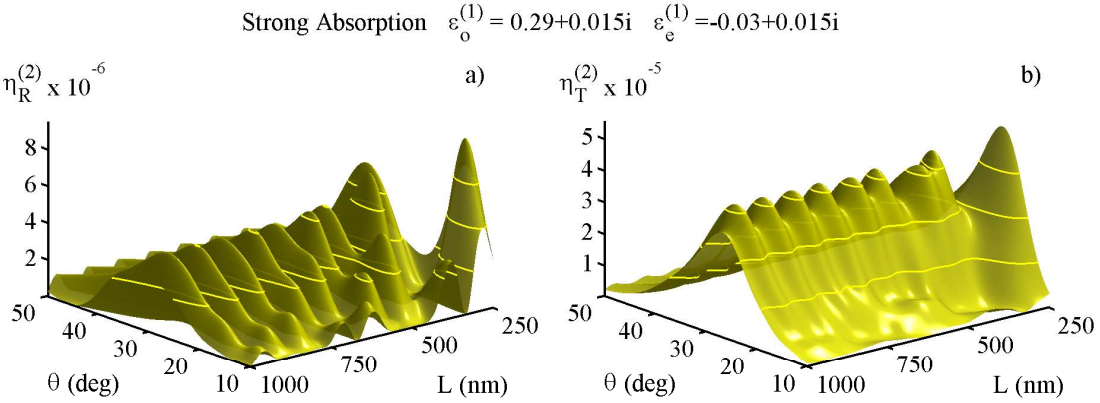

Figure 6.7: Second harmonic generation slab efficiencies $\eta_R^{(2)}$ (a) and $\eta_T^{(2)}$ (b) of converting the incident fundamental wave into backward- and forward-scattered second harmonic waves, respectively, evaluated for the optical intensity $I_i^{(1)} = 4\,\mathrm{MW/cm^2}$ of the incident fundamental wave in the strong-absorption regime with $\varepsilon_o^{(1)} = 0.29 + 0.015i$, $\varepsilon_e^{(1)} = -0.03 + 0.015i$ and $\varepsilon_o^{(2)} = 2.26$.

efficiencies of ***Fig.6.7a*** and ***Fig.6.7b*** are nonetheless remarkable for a slab of micrometer thickness. This is due to the fact that $\Gamma^{(1)}$ of ***Fig.6.4b*** still shows a shallow structure (at angles smaller than 30°) where it exceeds 10, which is a reminiscence of the corresponding strong ridge of ***Fig.6.2b*** and ***Fig.6.3b***. Such a field enhancement factor, combined with phase matching, yields the peak values $\eta_R^{(2)} = 3 \times 10^{-5}$ and $\eta_T^{(2)} = 4 \times 10^{-4}$ of ***Fig.6.7a*** and ***Fig.6.7b***. Again, such results are interesting since a medium exhibiting such linear and nonlinear optical properties can be designed even without the use of gain media.

6.4 Comparison of second harmonic generation in indefinite ENZ media and in nonindefinite and non-ENZ media

The strong frequency-doubling efficiency is, in our scheme, fully due to the above-discussed linear enhancement mechanism, which in turn takes place in the presence of principal permittivities of different signs (indefinite media) and of magnitudes

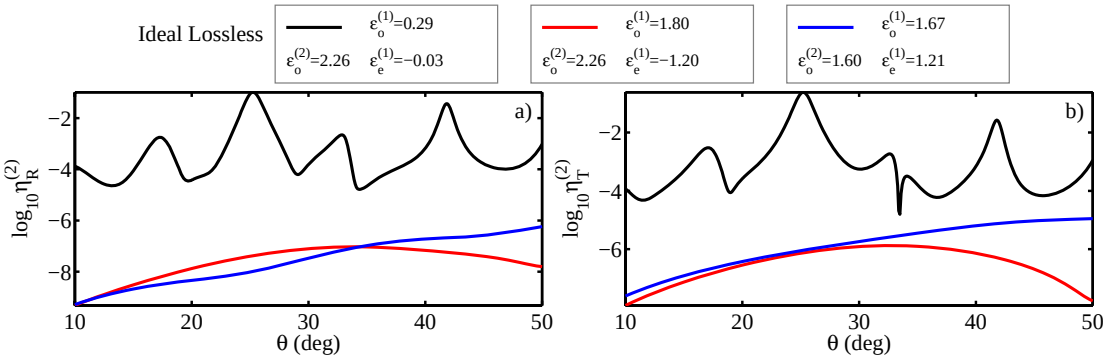

Figure 6.8: Logarithm of the second harmonic generation efficiencies $\eta_R^{(2)}$ (a) and $\eta_T^{(2)}$ (b) as functions of the incidence angle ϑ for different slabs of thickness $L = 700\,\text{nm}$ in the ideal lossless regime. Black, red and blue lines correspond to indefinite ε-near-zero, indefinite non-ε-near-zero, and standard uniaxial media, respectively.

smaller than one (ε-near-zero or ENZ media). In order to additionally stress the key and irreplaceable role played by this unusual linear optical response (experienced by the fundamental wave) in the whole second harmonic generation process, we have evaluated the second harmonic scattering efficiencies $\eta_R^{(2)}$ and $\eta_T^{(2)}$ of other slabs (of thickness $L = 700\,\text{nm}$) exhibiting the same nonlinear optical coefficient Δ as above but characterized by two distinct dielectric behaviors at the fundamental frequency: (1) indefinite permittivity with principal permittivities of magnitude greater than 1 and (2) standard uniaxial anisotropic permittivity.

In ***Fig.6.8***, ***Fig.6.9*** and ***Fig.6.10*** we plot the logarithm of such efficiencies as a function of the incidence angle ϑ and compare the results with those extracted from ***Fig.6.5***, ***Fig.6.6*** and ***Fig.6.7*** (at $L = 700\,\text{nm}$) using black lines for the indefinite ε-near zero medium (with $\Re[\varepsilon_o^{(1)}] = 0.29$, $\Re[\varepsilon_e^{(1)}] = -0.03$ and $\varepsilon_o^{(2)} = 2.26$), red lines for the indefinite non-ε-near-zero medium (with $\Re[\varepsilon_o^{(1)}] = 1.80$, $\Re[\varepsilon_e^{(1)}] = -1.20$ and $\varepsilon_o^{(2)} = 2.26$), and blue lines for the standard uniaxial crystal (with $\Re[\varepsilon_o^{(1)}] = 1.67$, $\Re[\varepsilon_e^{(1)}] = 1.21$ and $\varepsilon_o^{(2)} = 1.60$). The values of the permittivities of the nonindefinite and non-ε-near-zero media have here been chosen, for comparison purposes, with the requirement that their real parts provide the same phase-matching angle $\vartheta_{pm} = 25.4°$ as in the situation considered above.

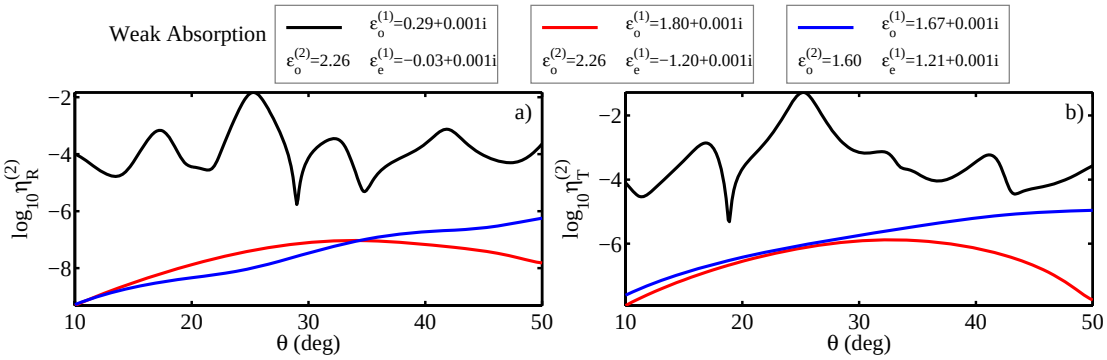

Figure 6.9: Logarithm of the second harmonic generation efficiencies $\eta_R^{(2)}$ (a) and $\eta_T^{(2)}$ (b) as functions of the incidence angle ϑ for different slabs of thickness $L = 700\,\mathrm{nm}$ in the weak-absorption regime. Black, red and blue lines correspond to indefinite ε-near-zero, indefinite non-ε-near-zero, and standard uniaxial media, respectively.

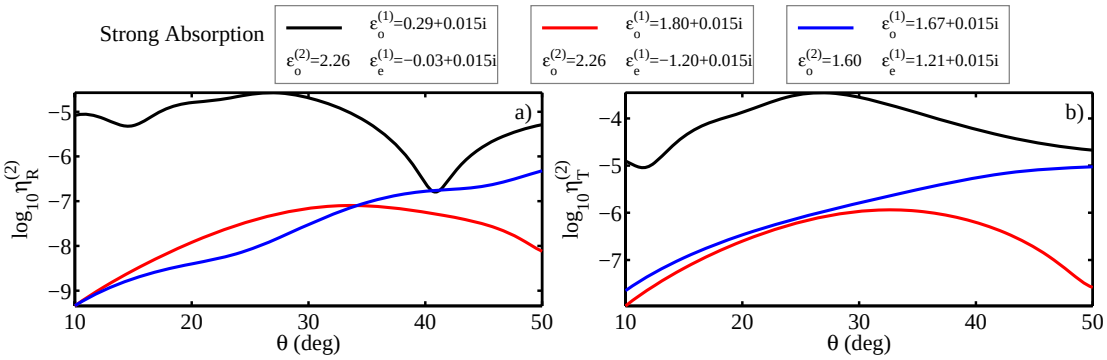

Figure 6.10: Logarithm of the second harmonic generation efficiencies $\eta_R^{(2)}$ (a) and $\eta_T^{(2)}$ (b) as functions of the incidence angle ϑ for different slabs of thickness $L = 700\,\mathrm{nm}$ in the strong-absorption regime. Black, red and blue lines correspond to indefinite ε-near-zero, indefinite non-ε-near-zero, and standard uniaxial media, respectively.

Each of these three situations is again investigated within the same three regimes hitherto considered, i.e., the ideal lossless regime (***Fig.6.8***), the weak-absorption regime (***Fig.6.9***), and the strong-absorption regime (***Fig.6.10***). The result emerging from ***Fig.6.8***, ***Fig.6.9*** and ***Fig.6.10*** is striking in that, in each possible situation, the second harmonic generation efficiency profiles characterizing the indefinite ε-near-zero medium are uniformly much greater (by several orders of magnitude) than those characterizing the slabs with different permittivity tensors at the fundamental wavelength. It is not excessive to state that such thin slabs (of thickness slightly greater than the fundamental wavelength) actually do not host second-harmonic generation *unless* their permittivity tensor is, at the fundamental frequency, indefinite with principal permittivities of magnitude smaller than 1, i.e., the conditions investigated in this paper. Apart from this general result, the very important point here is that, even in the most unfavorable situation of the strong-absorption regime where the underlying field enhancement mechanism is severely hampered by losses, the considered second harmonic generation process is remarkable and still far more efficient than other processes.

6.5 Indefinite ENZ slab feasibility

A quadratically nonlinear anisotropic medium with very small principal permittivities of different signs is hardly found in nature and therefore, in order to prove the feasibility of the phenomenology discussed above, we here discuss and numerically design actual nanocomposites exhibiting such an uncommon optical response. We adopt the general strategy of achieving effective electromagnetic properties by dispersing nanoparticles within a hosting dielectric matrix. Since our target is an extremely anisotropic medium with quadratic nonlinear optical response, the dielectric matrix has to be optically anisotropic and quadratically nonlinear and, not less importantly, it has to allow nanoparticle dispersion. Particularly suitable for this role are some bent-core liquid crystals which, in addition to their reconfigurable uniaxial anisotropy and their intrinsic capability of hosting dispersed nanoparti-

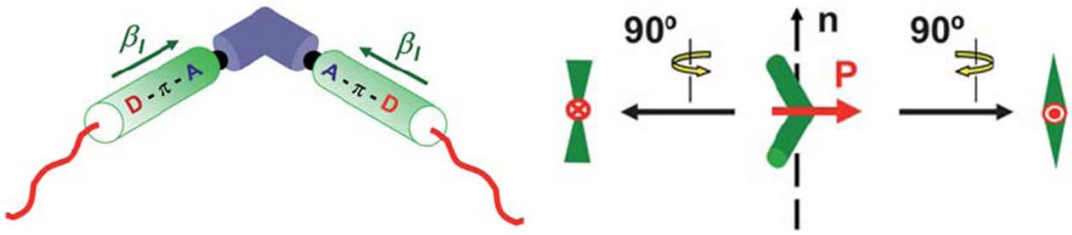

Figure 6.11: Schematic representations used for bent molecules in bent-core liquid crystal [94].

cle, are characterized by a marked quadratic nonlinear optical response [94] resulting from the shape of their molecules. In fact, the compact packing of the kinked molecules produces a strong polar interaction so that the sample can be ordered in a noncentrosymmetric polar fashion to show a marked quadratic nonlinear optical response [94] (***Fig.6.11***). Therefore, for the nanocomposite we are designing, we here assume the hosting matrix to be a bent-core liquid crystal characterized, in the reference frame hitherto used (see ***Fig.6.1***), by the permittivity tensor $\varepsilon = \text{diag}\left[\varepsilon_o^{(LC)}, \varepsilon_o^{(LC)}, \varepsilon_e^{(LC)}\right] = (2.25, 2.25, 2.89)$ (which are typical principal permittivities for liquid crystals) and by the d matrix of (6.1) (a situation easily achievable through an externally applied bias electric field). By dispersion of suitable nanoparticles within the liquid crystal, the overall macroscopic medium is led to exhibit effective electromagnetic properties different from those of its constituents since the nanoparticle radius (of the order of a few nanometers) is much smaller than both the fundamental and the second-harmonic wavelengths. Since one of the effective principal permittivities must have a negative real part, it is evident that metal nanoparticles have to be employed whose composition and volume density have to be suitably chosen to achieve the desired permittivity indefiniteness.

We have numerically designed the linear permittivity tensor by means of an anisotropic extension of the standard Maxwell-Garnett mixing rule [16]. According to this approach, if $\varepsilon^{(M)} = \text{diag}\left[\varepsilon_o^{(M)}, \varepsilon_o^{(M)}, \varepsilon_e^{(M)}\right]$ is the permittivity tensor of the hosting dielectric matrix and $\varepsilon^{(m)}$ is the dielectric permittivity of the metal nanoparticles (which are optically isotropic), the mixture's effective permittivity is

$\varepsilon^{(eff)} = \text{diag}\left[\varepsilon_o^{(eff)}, \varepsilon_o^{(eff)}, \varepsilon_e^{(eff)}\right]$ so that the homogeneous effective medium is a uniaxial crystal with principal axis coinciding with those of the hosting matrix, and its ordinary ($j = o$) and extraordinary ($j = e$) effective permittivities are (2.28)

$$\varepsilon_j^{(eff)} = \left\{ 1 + \frac{f\left[\varepsilon^{(m)} - \varepsilon_j^{(M)}\right]}{\varepsilon_j^{(M)} + (1-f)N_j\left[\varepsilon^{(m)} - \varepsilon_j^{(M)}\right]} \right\} \varepsilon_j^{(M)} . \tag{6.11}$$

where the depolarization factors N_j are (2.24)

$$N_j = \frac{1}{2}\int_0^\infty \frac{\varepsilon_j^{(M)} ds}{\left[1+\varepsilon_j^{(M)} s\right]\sqrt{\left[1+\varepsilon_o^{(M)} s\right]^2\left[1+\varepsilon_e^{(M)} s\right]}} \tag{6.12}$$

The permittivities of (6.11) are the anisotropic generalization of the standard Maxwell-Garnett mixing rule (to which (6.12) reduces in the isotropic limit where $N_j = 1/3$), the depolarization factors accounting for the effect of the anisotropy. Note that, in analogy to the isotropic situation, the nanoparticle radius does not appear in (6.11) so that the mixture design has to be performed by tuning the volume filling fraction f.

We have assumed the quadratically nonlinear optical response of the mixture to coincide with that of the liquid crystal, thus neglecting the effect of the nanoparticles. This is justified by the fact that, since the nanoparticles are spheres, dielectrically homogeneous, isotropic, and randomly dispersed within the liquid crystal, the d matrix associated with the quadratic nonlinearity of the mixture, for symmetry reasons, has to show the same structure as that in (6.1). Therefore nanoparticles can change only the values of Δ and δ of (6.1), a variation we have neglected because of the small nanoparticle densities we use.

6.5.1 Nanocomposite design: weak-absorption regime

In order to achieve the weak-absorption regime it is imperative to resort to gain media that partially compensate the medium losses due to the metal nanoparticles. This can be done by dispersing, within the liquid crystal bulk, optically pumped dye molecules whose presence is not incompatible with the target of achieving permittivities of very small amplitudes [95]. Specifically, we consider here rhodamine

6G molecules whose dispersion within the liquid crystal produces a change of the dielectric permittivity $\Delta\varepsilon^{(R6G)}$ yielding, for the permittivity tensor of the hosting matrix,

$$\varepsilon^{(M)} = \varepsilon^{(LC)} + \Delta\varepsilon^{(R6G)}\mathbb{1}\,, \tag{6.13}$$

where $\mathbb{1}$ is the identity matrix.

The classical electron oscillator model envisions that the electron charge cloud in a real atom may be displaced from its equilibrium position with and instantaneous displacement $\boldsymbol{r}(t)$. Because of the positive charge on the nucleus, this displacement causes the electronic charge cloud to experience a linear restoring force $-K\boldsymbol{r}(t)$. The electronic cloud is thus similar to a point electron with mass m and charge e that is attached to a spring with spring constant K. The classical equation of motion for an electron suspended on such a spring and subjected to an externally applied electric field $\boldsymbol{E}(\boldsymbol{r},t)$ is then

$$\frac{d^2\boldsymbol{r}}{dt^2} + \gamma\frac{d\boldsymbol{r}}{dt} + \omega_a^2\boldsymbol{r}(t) = -\frac{e}{m}\boldsymbol{E}(\boldsymbol{r},t)\,, \tag{6.14}$$

where γ is the damping rate or damping coefficient for the oscillator and ω_a is the classical oscillator's resonance frequency, given by $\omega_a^2 = K/m$.

We assume to model the gain material made of fluorescent dye molecules as a four level atomic system with occupation density $N_i(\boldsymbol{r},t)$ of the i-th state ($i = g,\ 1,\ 2,\ 3$) and N_0 the total dye concentration ($N_0 = N_g + N_1 + N_2 + N_3$). By definition the polarization density $\boldsymbol{P}_e(\boldsymbol{r},t)$ at the emission frequency band, is the total dipole moment per unit volume, therefore, it can be expressed as $\boldsymbol{P}_e(\boldsymbol{r},t) = \Delta N(\boldsymbol{r},t)e\boldsymbol{r}(t)$, where $\Delta N(\boldsymbol{r},t) = N_2(\boldsymbol{r},t) - N_1(\boldsymbol{r},t)$ is the population inversion between levels 2 and 1. According to [96, 97] the polarization density obeys to classical equation of motion (6.14)

$$\frac{\partial^2}{\partial t^2}\boldsymbol{P}_e(\boldsymbol{r},t) + \Delta\omega_e\frac{\partial}{\partial t}\boldsymbol{P}_e(\boldsymbol{r},t) + \omega_e^2\boldsymbol{P}_e(\boldsymbol{r},t) = -\sigma_e\Delta N(\boldsymbol{r},t)\boldsymbol{E}(\boldsymbol{r},t)\,, \tag{6.15}$$

where $\Delta\omega_e$ is the bandwidth of the dye transition at the emitting angular frequency ω_e and σ_e the coupling strength of $\boldsymbol{P}_e(\boldsymbol{r},t)$ to the electric field $\boldsymbol{E}(\boldsymbol{r},t)$. Assuming time harmonic electric field $\boldsymbol{E}(\boldsymbol{r},t) = \Re\left[\boldsymbol{E}(\boldsymbol{r})e^{-i\omega t}\right]$, harmonic polarization density

$\boldsymbol{P}_e(\boldsymbol{r},t) = \Re\left[\boldsymbol{P}_e(\boldsymbol{r})e^{-i\omega t}\right] = \varepsilon_0\chi_e\boldsymbol{E}(\boldsymbol{r},t)$ and constant population inversion ΔN (i.e., steady state), (6.15) becomes

$$\chi_e = \frac{1}{\varepsilon_0}\frac{\sigma_e\Delta N}{\omega^2-\omega_e^2+i\omega\Delta\omega_e}\,.$$

The total displacement can be written as

$$\boldsymbol{D}(\boldsymbol{r}) = \varepsilon_0\boldsymbol{E}(\boldsymbol{r}) + \boldsymbol{P}_r(\boldsymbol{r}) + \boldsymbol{P}_e(\boldsymbol{r})\,,$$

where $\boldsymbol{P}_r(\boldsymbol{r})$ is the polarization contribution due to dielectric medium hosting the dye and $\boldsymbol{P}_e(\boldsymbol{r})$ is the polarization contribution due to the dispersed gain material in host matrix. Therefore the dielectric permittivity change due to the active molecules is

$$\Delta\varepsilon^{(R6G)} = \frac{\sigma_e\Delta N}{\varepsilon_0(\omega^2-\omega_e^2+i\Delta\omega_e)}\,,$$

where $\sigma_e = 6.55\times10^{-8}\,\mathrm{C}^2/\mathrm{kg}$, $\lambda_e = 2\pi c/\omega_e = 570\,\mathrm{nm}$ is the center emission wavelength, $\Delta\lambda_e = 30\,\mathrm{nm}$ ($\Delta\omega_e = 2\pi c\Delta\lambda_e/\lambda_e^2$) is the wavelength line width. ΔN, the inversion population between levels 2 and 1, is given by

$$\Delta N = \frac{(\tau_{21}-\tau_{10})\Gamma_{pump}}{1+(\tau_{32}+\tau_{21}+\tau_{10})\Gamma_{pump}}N_0\,,$$

where τ_{ij} is the lifetime for the transition from state i to the lower state j ($\tau_{21} = 3.99\,\mathrm{ns}$, $\tau_{32} = \tau_{10} = 100\,\mathrm{fs}$), N_0 is the dye molecule density and Γ_{pump} is the pumping rate from level 0 to level 3 defined as $\Gamma_{pump} = \sigma_a I_{pump}\lambda_a/(hc)$ where $\sigma_a = 3.2\times10^{-16}\,\mathrm{cm}^{-2}$ is the absorption cross section, I_{pump} is the pump intensity, h is the Planck constant, and $\lambda_a = 531\,\mathrm{nm}$ is the pump wavelength.

We consider chromium nanoparticles with a diameter of 7 nm [98] whose dielectric permittivity $\varepsilon^{(m)}$ is given by the Drude model,

$$\varepsilon^{(m)} = 1 - \frac{\omega_p^2}{\omega^2+i\gamma\omega}\,, \tag{6.16}$$

where $\omega_p = 6.68\times10^{15}\,\mathrm{s}^{-1}$ and $\gamma = 7.13\times10^{13}\,\mathrm{s}^{-1}$ [99]. We choose here $f = 0.146$ for the volume filling fraction of the chromium nanoparticles, $N_0 = 6\times10^{18}\,\mathrm{cm}^{-3}$ for the rhodamine molecule concentration, and $I_{pump} = 380\,\mathrm{W/cm}^2$ for the optical pump intensity. Using such numerical data and inserting (6.13) and (6.16) into (6.11) we

obtain, for $\lambda^{(1)} = 574\,\mathrm{nm}$, $[\varepsilon_o^{(1)}]^{(eff)} = 0.2894{+}0.0011i$, $[\varepsilon_e^{(1)}]^{(eff)} = -0.0319{+}0.0012i$ and $[\varepsilon_o^{(2)}]^{(eff)} = 2.2638 + 0.0035i$ which are values compatible with those used above for discussing both the slab linear transmission and the second harmonic process in the weak-absorption regime.

6.5.2 Nanocomposite design: strong-absorption regime

The strong-absorption regime is achieved more simply than the weak one since gain media are not required when synthesizing the nanocomposite. Therefore the dielectric matrix in this case coincides with the liquid crystal, so that

$$\varepsilon^{(M)} = \varepsilon^{LC}\,. \tag{6.17}$$

We consider palladium nanoparticles [100] whose dielectric permittivity ε^m is given by the Drude model of (6.16) with parameters $\omega_p = 6.68 \times 10^{15}\,\mathrm{s}^{-1}$ and $\gamma = 7.13 \times 10^{13}\,\mathrm{s}^{-1}$ [99]. Choosing $f = 0.146$ for the volume filling fraction of the palladium nanoparticles and inserting (6.17) and (6.16) into (6.11) we obtain, for $\lambda^{(1)} = 454\,\mathrm{nm}$, $[\varepsilon_o^{(1)}]^{(eff)} = 0.2927 + 0.0154i$, $[\varepsilon_e^{(1)}]^{(eff)} = -0.0287 + 0.0148i$ and $[\varepsilon_o^{(2)}]^{(eff)} = 2.2612 + 0.0005i$ which, again, are values compatible with those used above for discussing both the slab linear transmission and the second harmonic generation process in the strong-absorption regime.

6.6 Conclusions

In conclusion, we have shown that a micrometer-thick slab filled by an indefinite medium with permittivity moduli smaller than 1 and exhibiting quadratic optical nonlinearity is able to host a very efficient second harmonic generation process. The frequency-doubling efficiency is much greater (by several orders of magnitude) than that characterizing second harmonic generation from a slab filled by a standard quadratic medium, and it is caused by a powerful field enhancement mechanism resulting from the very small value of the longitudinal permittivity of the slab. Even though the overall process is supported by a coherent linear mechanism, we

have shown that absorption does not fully suppress the proposed second harmonic generation efficiency. It is worth stressing that the proposed field enhancement mechanism can easily be observed also in setups different from the considered slab. Our findings offer a different way to achieve efficient second harmonic generation from micro- and nanostructures and therefore we believe they could pave the way for conceiving a method for generation of nanometer-sized coherent light sources.

7 Terahertz active spatial filtering

We theoretically consider infrared-driven hyperbolic metamaterials able to spatially filter terahertz radiation. The metamaterial is a slab made of alternating semiconductor and dielectric layers whose homogenized uniaxial response, at THz frequencies, shows principal permittivities of different signs. The gap provided by metamaterial hyperbolic dispersion allows the slab to stop spatial frequencies within a bandwidth tunable by changing the infrared radiation intensity. We numerically prove the device functionality by resorting to full wave simulation coupled to the dynamics of charge carries photoexcited by infrared radiation in semiconductor layers.

7.1 Terahertz hyperbolic metamaterial

Manipulating terahertz radiation is generally difficult since most standard materials simply do not respond to such frequencies. However, the advent of metamaterials has partially reduced this difficulty because their electromagnetic properties can be artificially manipulated [101] through a suitable design of the underlying constituent unit cells. At the same time, a number of setups have been proposed for steering the THz radiation [102]. Reconfigurable electrically [103] or optically [104] driven metamaterials have been exploited for conceiving active THz devices [105].

Most of the proposed active THz devices are tunable frequency domain filters since it is relatively simple to control the metamaterial dispersion properties through

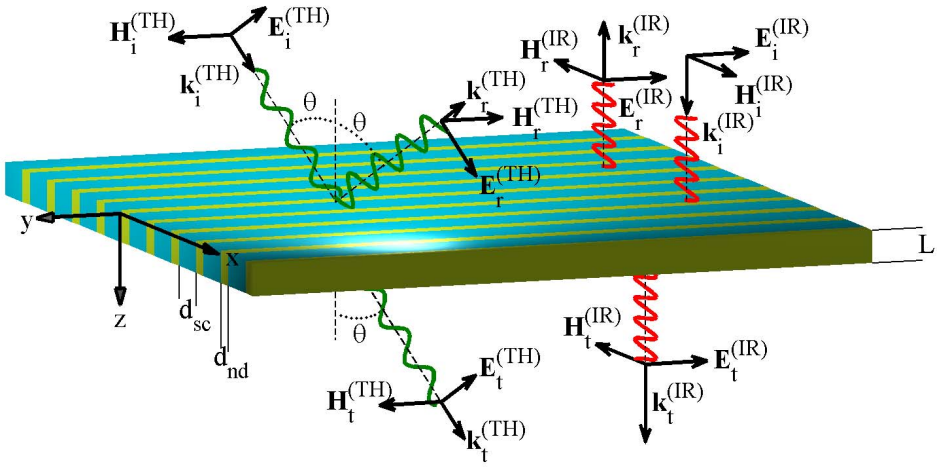

Figure 7.1: Layered metamaterial setup together with THz (TH) and infrared (IR) plane waves geometry.

external stimuli. In this letter, we propose a theoretical way to achieve active and spatial filtering of the THz radiation using a suitable hyperbolic metamaterial whose THz response can be tuned by an auxiliary infrared field. The hyperbolic dispersion relation characterizing extraordinary plane waves in indefinite media is the main physical ingredient leading to unusual optical effects [11, 106] and supporting a number of proposed devices [54, 91, 107].

Fig.7.1 shows the tunable hyperbolic metamaterial we consider here, together with the field's geometry. The metamaterial slab of thickness L is obtained by stacking along the x axis alternating layers of an intrinsic semiconductor (sc) and a negative dielectric (nd) of thicknesses d_{sc} and d_{nd}, respectively. It is illuminated by an infrared monochromatic (IR) plane wave linearly polarized along the y axis and normally impinging onto the slab interface at $z = 0$. The THz field (TH) is a transverse magnetic (TM or p-polarized) monochromatic plane impinging with incidence angle ϑ onto the interface.

7.2 Semiconductor dielectric behavior

The infrared field within the semiconductor layers photoexcites electrons to the conduction band, which dynamically recombine so that resulting electron density N is described by the rate equation [108]

$$\frac{\partial N}{\partial t} = \frac{\varepsilon_0}{2\hbar}\Im[\varepsilon_{sc}(\omega_{IR})]|E^{(IR)}|^2 - \frac{N}{\tau_R} - BN^2\,, \tag{7.1}$$

where $\hbar$ is the Planck constant divided by 2π, ε_0 is the absolute vacuum permittivity, $\varepsilon_{sc}(\omega_{IR})$ is the semiconductor permittivity at the infrared frequency ω_{IR}, $E^{(IR)}$ is the infrared field within the semiconductor layers, τ_R is the carrier's nonradiative recombination time and B is the coefficient of radiative recombination. The semiconductor dielectric behavior at the infrared frequency is described by the linearized permittivity model [108]

$$\varepsilon_{sc}(\omega_{IR}) = \left(n_{IR} + \frac{\delta n_0}{N_0}N\right)^2 + i\frac{n_{IR}c}{\omega_{IR}}A(N_0 - N) \tag{7.2}$$

where n_{IR} is the infrared semiconductor refractive index background, N_0 is the transparency value of the carrier density, δn_0 the refractive index change at transparency, c is the speed of light in vacuum and A is the differential absorption coefficient. At steady state ($\partial N/\partial t = 0$), compatible with the considered monochromatic IR field, equation (7.1) and (7.2) yield

$$N = \frac{1}{2\tau_R B}\left[-(1+W) + \sqrt{(1+W)^2 + 4\tau_R B N_0 W}\right]\,, \tag{7.3}$$

where $W = |E^{(IR)}/E_{sat}|^2$ and $|E_{sat}| = [\tau_R\varepsilon_0 n_{IR}cA/(2\hbar\omega_{IR})]^{-1/2}$, so that electron density shows a saturable behavior (i.e., $N \simeq N_=$ if $|E^{(IR)}| \gg |E_{sat}|$), as a consequence of the saturable absorption model of (7.2).

Maxwell equations for the field $E^{(IR)}$ together with (7.2) and (7.3) describe the infrared nonlinear behavior within semiconductor layers. The resulting (and selfconsistently evaluated) electron density N has a strong impact on the semiconductor response at the THz frequency ω_{TH}, since the permittivity is

$$\varepsilon_{sc}(\omega_{TH}) = \varepsilon_{sc}^{(0)}(\omega_{TH}) + \frac{i}{\varepsilon_0}\frac{(e^2\tau/m^*)N}{\omega_{TH}(1 - i\omega_{TH}\tau)} \tag{7.4}$$

where $\varepsilon_{sc}^{(0)}(\omega_{TH})$ is the semiconductor permittivity in the absence of the infrared radiation, $-e$ and m^* are electron charge and reduced mass, and τ is the relaxation time. In equation (7.4), note that the term, proportional to N, is the standard Drude permittivity contribution due to conduction band electrons and is the physical ingredient that allows the infrared field to tune the overall slab THz response.

7.3 Structured metamaterial dielectric behavior

If the layers thicknesses d_{sc} and d_{nd} are much smaller than the THz wavelength (on the order of tens of microns), the overall metamaterial slab of ***Fig.7.1*** shows a homogeneous THz uniaxial response with permittivities (the optical axis lying along the staking x-axis) [109]

$$\varepsilon_x(\omega_{TH}) = \frac{1}{\dfrac{f_{sc}}{\varepsilon_{sc}(\omega_{TH})} + \dfrac{f_{nd}}{\varepsilon_{nd}(\omega_{TH})}} \tag{7.5}$$

$$\varepsilon_z(\omega_{TH}) = \varepsilon_y(\omega_{TH}) = f_{sc}\varepsilon_{sc}(\omega_{TH}) + f_{nd}\varepsilon_{nd}(\omega_{TH})\,, \tag{7.6}$$

where

$$f_{sc} = \frac{d_{sc}}{d_{sc}+d_{nd}} \qquad f_{nd} = \frac{d_{nd}}{d_{sc}+d_{nd}}$$

are the layers filling fractions whereas $\varepsilon_{nd}(\omega_{TH})$ is the the dielectric permittivity of the negative dielectric layers for which $\Re[\varepsilon_{nd}(\omega_{TH})] < 0$.

Because the permittivities $\varepsilon_x(\omega_{TH})$ and $\varepsilon_z(\omega_{TH})$ involve averages of different kinds, it is well known that it is possible to tailor the structure so $\varepsilon_x(\omega_{TH})$ and $\varepsilon_z(\omega_{TH})$ have different signs, the resulting hyperbolic medium begin tunable, in the present analysis, through the auxiliary infrared field. The considered wavelengths are $\lambda_{IR} = 2\pi c/\omega_{IR} = 0.879\,\mu\text{m}$ and $\lambda_{TH} = 2\pi c/\omega_{TH} = 23.08\,\mu\text{m}$ and we have chosen gallium arsenide (GaAs) as semiconductor (for which $\tau_R = 10\,\text{ns}$, $B = 1.3\times10^{-10}\,\text{cm}^3\text{s}^{-1}$, $n_{IR} = 3.6$, $\delta n_0 = -0.07$, $N_0 = 9.91\times10^{17}\,\text{cm}^3$, $A = 1.71\times10^{-15}\,\text{cm}^2$, $\varepsilon_{sc}^{(0)}(\omega_{TH}) = 12.9$, $\tau = 3.29\times10^{-13}\,\text{s}$ and $m^* = 0.067m_0$, m_0 being the electron mass [108]) with filling fraction $f_{sc} = 0.1$ and a negative dielectric with

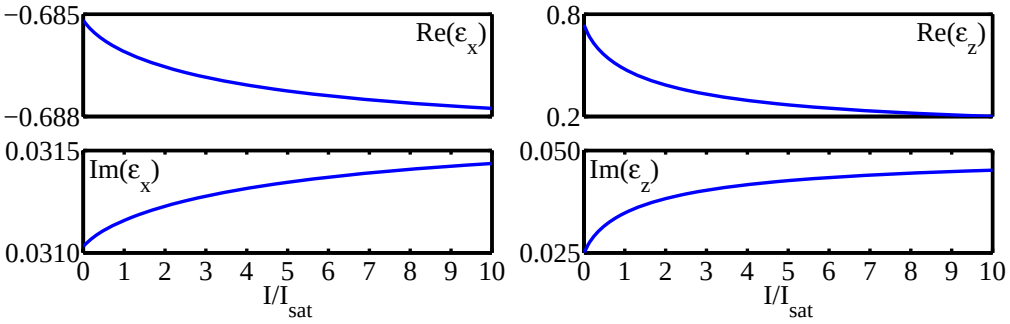

Figure 7.2: Terahertz homogenized slab permittivities $\varepsilon_x(\omega_{TH})$ and $\varepsilon_z(\omega_{TH})$ as functions of the normalized local optical intensity of the infrared field.

permittivity $\varepsilon_{nd}(\omega_{TH}) = -0.61 + 0.003i$. This value coincides with that of calcium fluoride CaF_2 with an imaginary part reduced by a tenth for discussion purposes.

Fig.7.2 plots $\varepsilon_x(\omega_{TH})$ and $\varepsilon_z(\omega_{TH})$ as functions of the infrared optical intensity $I^{(IR)} = \varepsilon_0 c|E^{(IR)}|^2/2$ (normalized with the saturation intensity $I_{sat} = \varepsilon_0 c|E_{sat}|^2/2 = 3.7\,\mathrm{kW/cm^2}$), with the simplified assumption that such intensity can be regarded as uniform within the bulk of the slab and equal to incident infrared plane wave intensity (see below). It is evident from ***Fig.7.2*** that the structure has been tailored to show indefinite permittivity tensor in the absence of infrared illumination (i.e., $\Re(\varepsilon_x) < 0$ and $\Re(\varepsilon_z) < 0$ for $I^{(IR)} = 0$). Remarkably, the infrared intensity $I^{(IR)}$ has a strong impact on $\Re(\varepsilon_z) < 0$. In ***Fig.7.3***, we have plotted the reflectivity $R = |\boldsymbol{E}_r^{(TH)}|^2/|\boldsymbol{E}_i^{(TH)}|^2$ and the transmissivity $T = |\boldsymbol{E}_t^{(TH)}|^2/|\boldsymbol{E}_i^{(TH)}|^2$ (see ***Fig.7.1*** for the definition of the field amplitudes) as functions of the THz incidence angle ϑ for a homogenized slab of thickness $L = 9.23\,\mu\mathrm{m}$ with permittivities coinciding with those of ***Fig.7.2*** at the intensities $I^{(IR)} = 0$, $I^{(IR)} = I_{sat}$ and $I^{(IR)} = 10I_{sat}$ (see Ref. [110] for the expression of T). It is worth noting that all the three transmissivity curves have a bell-shaped profile with maximum located at an angle dependent on the infrared intensity (analogously the reflectivity have a complementary behavior) so that the slab can be regarded as an active spatial filter allowing (forbidding) transmission (reflection) of those THz plane waves with incidence angle close to a central angle in turn tunable through the infrared optical intensity.

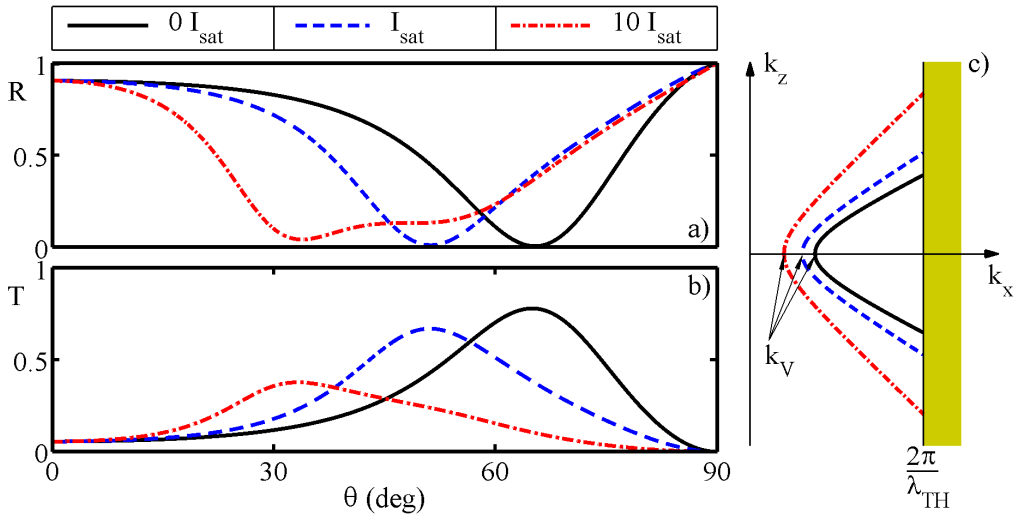

Figure 7.3: (a) Reflectivity R, (b) transmissivity T at the wavelength $\lambda_{TH} = 23.08\,\mu\text{m}$ as functions of the THz incidence angle ϑ for a homogenized slab of thickness $L = 9.23\,\mu\text{m}$ and permittivities of ***Fig.7.1*** at three different local infrared intensities $I^{(IR)}$ and, (c) THz hyperbolic dispersion curves for the three cases of panels (a) and (b). The hyperbola vertex is at $k_x = k_V = (2\pi/\lambda_{TH})/\sqrt{|\varepsilon_z|}$.

7.4 Physical mechanism and simulations

The physical mechanism supporting such an active spatial filtering functionality can easily be grasped by noting that the chosen TM incident THz plane waves couples to the slab extraordinary waves whose dispersion relation is $k_x^2/\varepsilon_z - k_z^2/\varepsilon_x = (2\pi/\lambda_{TH})^2$, where the signs of the permittivities (***Fig.7.2***) have been explicitly reported for clarity purposes (neglecting the permittivities' imaginary parts). Such dispersion relation is, in the k_xk_z plane, a hyperbola with vertices along the k_x-axis located at $k_x = \pm k_V = (2\pi/\lambda_{TH})\sqrt{|\varepsilon_z|}$ (see ***Fig.7.3c*** where the hyperbola corresponding to the considered three infrared intensities are plotted). A momentum match at the interface $z = 0$ implies that the extraordinary plane waves have transverse wave vector $k_x = (2\pi/\lambda_{TH})\sin\vartheta$ so that in the two situations $|\sin\vartheta| < \sqrt{|\varepsilon_z|}$ or $|\sin\vartheta| > \sqrt{|\varepsilon_z|}$ (i.e. $|k_x| < k_V$ or $|k_x| > k_V$, respectively) the externally impinging THz plane wave excites, within the slab, evanescent or propagating waves, respectively. As a consequence, the transmission is low for $\sin\vartheta < \sqrt{|\varepsilon_z|}$ (where

evanescent waves provides a residual "tunneling" radiation), it reaches a maximum at greater angles (due to the slab propagating waves) and it eventually vanishes at $\vartheta = 90°$ for geometrical reasons.

The discussion of the THz spatial filtering functionality has hitherto been based, for clarity purposes, on three simplified assumptions:

- low-loss regime (small imaginary part of the negative dielectric permittivity),
- THz electromagnetic homogenization of the layered medium, and
- uniformity of the infrared optical intensity within the slab bulk.

While the first two assumptions can easily be supported, the third one is more serious since the layers' periodicity is generally comparable with the infrared wavelength and, in addition, the reflection of infrared radiation by the slab together with its nonlinear behavior within semiconductor layers have to be considered. To account for of all these physical ingredients and to show that the structure actually behaves as an active THz spatial filter, we have resorted to full wave simulations where linear and nonlinear Maxwell equations for the THz and the infrared field are coupled to the electron dynamics described by (7.3) and (7.2). We have chosen the layers thicknesses $d_{sc} = 24nm$ and $d_{nd} = 220nm$ and the permittivities $\varepsilon_{nd}(\omega_{TH}) = -0.61 - 0.03i$, $\varepsilon_{nd}(\omega_{IR}) = 2.04$ which are the CaF_2 permittivities at the considered THz and infrared frequencies, respectively, whereas all the remaining involved parameters are those used above.

Fig.7.4 shows the results of the simulations, where we plotted the THz transmissivity and reflectivity of the structure for three different values of the optical intensity $I_i^{(IR)} = \varepsilon_0 c|\boldsymbol{E}_i^{(IR)}|^2/2$ of the *incident* infrared plane wave (***Fig.7.1***). Note that the overall spatial filtering functionality is evidently exhibited by the considered realistic structure, even though the values of the transmissivity are smaller as compared to those of ***Fig.7.3***. This is a consequence of the fact that full-wave simulations have been performed using the actual value of the CaF_2 permittivity, whereas in the effective medium predictions ***Fig.7.3***, a reduced value of its imaginary part has been used.

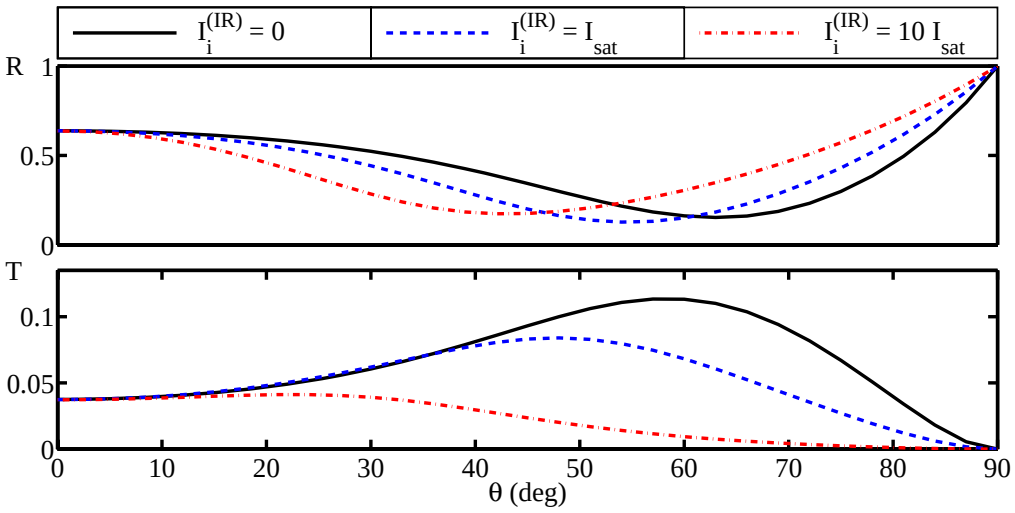

Figure 7.4: THz transmissivity R and reflectivity T of the metamaterial of ***Fig. 7.1***, evaluated trough full waves simulations, for three different values of the optical intensity $I_i^{(IR)}$ of the *incident* infrared plane wave.

In conclusion, we have proposed a metamaterial structure which, driven by an auxiliary infrared field, is able to spatially filter THz radiation. We believe that the proposed combination of hyperbolic metamaterial and semiconductor concepts offer a different way to create novel and efficient THz active devices.

A

Propagation in anisotropic media

Monochromatic plane-wave propagation in anisotropic media

In an anisotropic crystal, the phase velocity of light depends on its state of polarization and on its direction of propagation. Given a direction of propagation in the medium, there exist only two eigenwaves with defined eigen-phase-velocities and polarization directions. Let us consider a monochromatic plane wave of angular frequency ω_0

$$\boldsymbol{E}(\boldsymbol{r},t) = \boldsymbol{E}_0 e^{-i(\omega_0 t - \boldsymbol{k}\cdot\boldsymbol{r})}\,, \qquad \boldsymbol{H}(\boldsymbol{r},t) = \boldsymbol{H}_0 e^{-i(\omega_0 t - \boldsymbol{k}\cdot\boldsymbol{r})}\,. \tag{A.1}$$

propagating in a linear non-magnetic dielectric homogeneous anisotropic medium. Substituting (A.1) into the macroscopic Maxwell's curl equations in the absence of sources we obtain

$$\begin{aligned} \boldsymbol{\nabla}\times\boldsymbol{E} &= -\frac{\partial \boldsymbol{B}}{\partial t}\,, \qquad &\Rightarrow \qquad \boldsymbol{k}\times\boldsymbol{E}_0 &= \omega_0\mu_0\boldsymbol{H}_0\,, \\ \boldsymbol{\nabla}\times\boldsymbol{H} &= \frac{\partial \boldsymbol{D}}{\partial t}\,, \qquad &\Rightarrow \qquad \boldsymbol{k}\times\boldsymbol{H}_0 &= -\omega_0\varepsilon_0\bar{\bar{\varepsilon}}_r\boldsymbol{E}_0\,, \end{aligned}$$

$$\boldsymbol{k}\times\boldsymbol{k}\times\boldsymbol{E}_0 = \omega_0\mu_0\boldsymbol{k}\times\boldsymbol{H}_0 = -\omega_0^2\varepsilon_0\mu_0\bar{\bar{\varepsilon}}_r\boldsymbol{E}_0\,,$$

and further we get the vector Helmholtz equation

$$\boldsymbol{k}\times\boldsymbol{k}\times\boldsymbol{E}_0 + \omega_0^2\varepsilon_0\mu_0\bar{\bar{\varepsilon}}_r\boldsymbol{E}_0 = 0\,. \tag{A.2}$$

This equation can also be written as

$$(\boldsymbol{k}\cdot\boldsymbol{E}_0)\boldsymbol{k} - k^2\boldsymbol{E}_0 + \omega_0^2\varepsilon_0\mu_0\boldsymbol{D}_0 = 0\,, \quad \Rightarrow \quad \omega_0^2\varepsilon_0\mu_0\boldsymbol{D}_0 = k^2\boldsymbol{E}_0 - (\boldsymbol{k}\cdot\boldsymbol{E}_0)\boldsymbol{k}\,, \tag{A.3}$$

where we used the identity[1] $\boldsymbol{k} \times \boldsymbol{k} \times \boldsymbol{E}_0 = \boldsymbol{k}(\boldsymbol{k} \cdot \boldsymbol{E}_0) - k^2 \boldsymbol{E}_0$. In (A.3) the electric displacement $\boldsymbol{D}_0$ is expressed by the difference between a vector parallel to $\boldsymbol{E}_0$ and the component of $\boldsymbol{E}_0$ parallel to $\boldsymbol{k}$. In other words, $\boldsymbol{D}_0$ belongs to the plane perpendicular to $\boldsymbol{k}$ and only two mutual orthogonal polarization for $\boldsymbol{D}_0$ within the crystal exist.

In the optical principal coordinate system (A.2) can be written as

$$\begin{pmatrix} \omega_0^2 \varepsilon_0 \mu_0 \varepsilon_x - k_y^2 - k_z^2 & k_x k_y & k_x k_z \\ k_x k_y & \omega_0^2 \varepsilon_0 \mu_0 \varepsilon_y - k_x^2 - k_z^2 & k_y k_z \\ k_x k_z & k_y k_z & \omega_0^2 \varepsilon_0 \mu_0 \varepsilon_z - k_x^2 - k_y^2 \end{pmatrix} \begin{pmatrix} E_{0x} \\ E_{0y} \\ E_{0z} \end{pmatrix} = 0$$

For nontrivial solution to exist, the coefficient's determinant must vanish

$$(\varepsilon_x k_x^2 + \varepsilon_y k_y^2 + \varepsilon_z k_z^2)(k_x^2 + k_y^2 + k_z^2) - k_0^2 [\varepsilon_x \varepsilon_y (k_x^2 + k_y^2) + \varepsilon_y \varepsilon_z (k_y^2 + k_z^2) + \varepsilon_x \varepsilon_z (k_x^2 + k_z^2)] + \\ + k_0^4 \varepsilon_x \varepsilon_y \varepsilon_z = 0\,, \quad \text{(A.4)}$$

where $k_0 = \omega/c = \omega\sqrt{\varepsilon_0 \mu_0}$. This equation represents a three-dimensional surface in $\boldsymbol{k}$ space and it is known as the Fresnel's wave surface or *normal surface* (***Fig.A.1***). It consists of two shells which have four points (two for positive values, corresponding to propagating waves, and two for negative values, corresponding to counter-propagating waves) in common, the two line that go through the origin and these points are the crystal's *optical axes*. Given a direction of propagation, there are two k values which are the intersections of direction of propagation and the normal surface. These two values correspond to two different phase velocities of the waves propagating along the chosen direction.

Equation (A.4) is often written in terms of the direction cosines of wave vector.

---

[1]

$$\boldsymbol{k} \times \boldsymbol{k} \times \boldsymbol{E} = \varepsilon_{ijk} k_j (\varepsilon_{klm} k_l E_m) = \varepsilon_{ijk} \varepsilon_{klm} k_j k_l E_m = \varepsilon_{kij} \varepsilon_{klm} k_j k_l E_m = \\ = (\delta_{il}\delta_{jm} - \delta_{im}\delta_{jl}) k_j k_l E_m = k_j k_i E_j - k_j k_j E_i = \boldsymbol{k}(\boldsymbol{k} \cdot \boldsymbol{E}) - k^2 \boldsymbol{E}$$

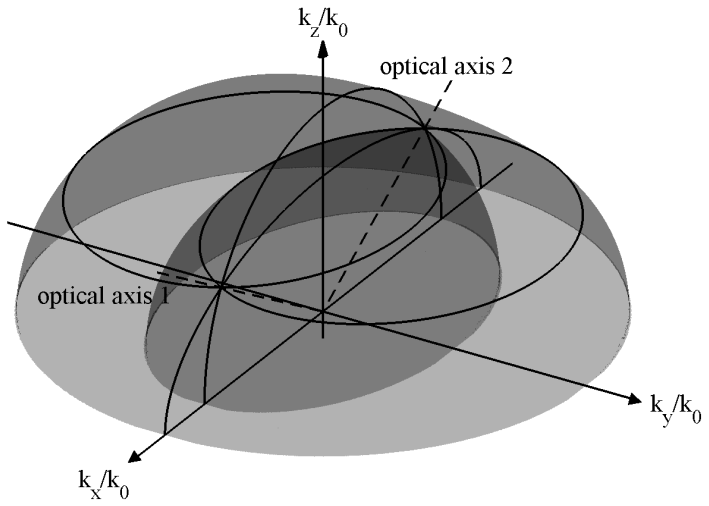

Figure A.1: Positive shells of Fresnel's wave surface or normal surface for a *biaxial* anisotropic crystal; they have two points in common which locate the crystal's optical axes.

By using the relation $s_i = k_i/k$, we get

$$(\varepsilon_x s_x^2 + \varepsilon_y s_y^2 + \varepsilon_z s_z^2)k^4 - k_0^2[\varepsilon_x\varepsilon_y(s_x^2 + s_y^2) + \varepsilon_y\varepsilon_z(s_y^2 + s_z^2) + \varepsilon_x\varepsilon_z(s_x^2 + s_z^2)]k^2 + \\ + k_0^4\varepsilon_x\varepsilon_y\varepsilon_z = 0\,. \quad \text{(A.5)}$$

This is a quadratic equation in k^2, because of the electric displacement $\boldsymbol{D}$ have only two degree of freedom; for a given direction of propagation the electric displacement $\boldsymbol{D}$ belongs to the perpendicular plane to $\boldsymbol{k}$, then there exist only two independent eigenvectors of the equation (A.2).

For example, considering a monochromatic plane wave propagating along the direction $\boldsymbol{s} = [0, \sin\vartheta, \cos\vartheta]$ (ϑ angle between $\boldsymbol{s}$ direction and s axis), then the (A.5) becomes

$$(\varepsilon_y \sin^2\vartheta + \varepsilon_z \cos^2\vartheta)k^4 - k_0^2[\varepsilon_y\varepsilon_z + \varepsilon_x\varepsilon_y \sin^2\vartheta + \varepsilon_x\varepsilon_z \cos^2\vartheta]k^2 + k_0^4\varepsilon_x\varepsilon_y\varepsilon_z = 0\,.$$

The eigenvalues of this secular equation are

$$k_1^2 = \frac{\varepsilon_y\varepsilon_z}{\varepsilon_y \sin^2\vartheta + \varepsilon_z \cos^2\vartheta}k_0^2\,, \qquad k_2^2 = \varepsilon_x k_0^2\,, \qquad \text{(A.6)}$$

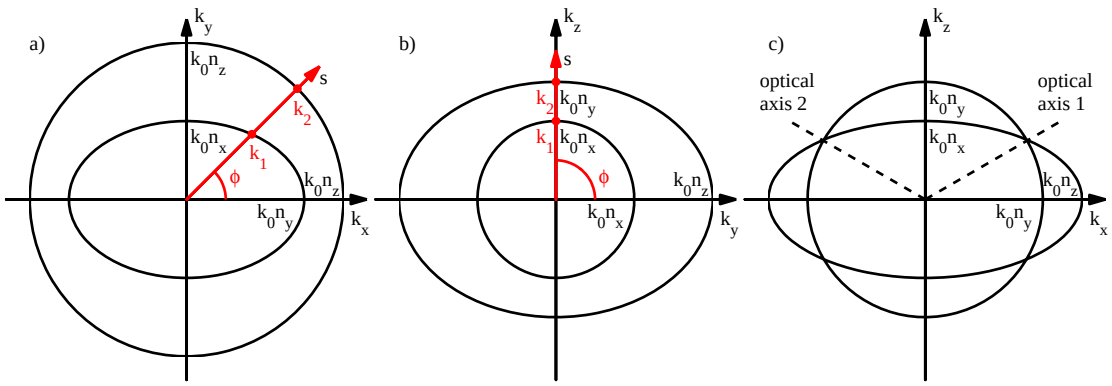

Figure A.2: Intersections of the Fresnel's wave surface with $k_x k_y$ plane (a), $k_x k_z$ plane (b) and $k_y k_z$ plane (c).

(***Fig.A.2a***) and the corresponding eigenvectors belong to plane perpendicular to $\boldsymbol{s}$ (parallel to the x axis and the direction $[0, -\sin\vartheta, \cos\vartheta]$ of yz plane ***Fig.A.4a***). Another particular case is that of a monochromatic plane wave propagating in z direction $\boldsymbol{s} = [0, 0, 1]$, than the (A.5) becomes

$$k^4 - k_0^2[\varepsilon_y + \varepsilon_x]k^2 + k_0^4 \varepsilon_x \varepsilon_y = 0\,,$$

the eigenvalues of this secular equation are (***Fig.A.2b***)

$$k_1^2 = \varepsilon_x k_0^2\,, \qquad\qquad k_2^2 = \varepsilon_y k_0^2 \tag{A.7}$$

and the corresponding eigenvector are long the x and y axes (***Fig.A.4b***).

If the field impinging on the facet of an anisotropic crystal is linearly polarized along one of the optical principal axes, its propagation into the crystal is unaltered. On the other hand, if the impinging field has a linear polarization state along an arbitrary direction, its polarization within the crystal generally changes because of difference between two component velocities.

The normal surface is uniquely determined by the principal dielectric permittivities ε_x, ε_y and ε_z. As we have seen above, when these three values are all different, there are two optical axes and in this case the anisotropic crystal is said to be *biaxial*. In other optical anisotropic material it happens that two of principal dielectric permittivities are equal, as $\varepsilon_x = \varepsilon_y \neq \varepsilon_z$, in which case the characteristic polynomial

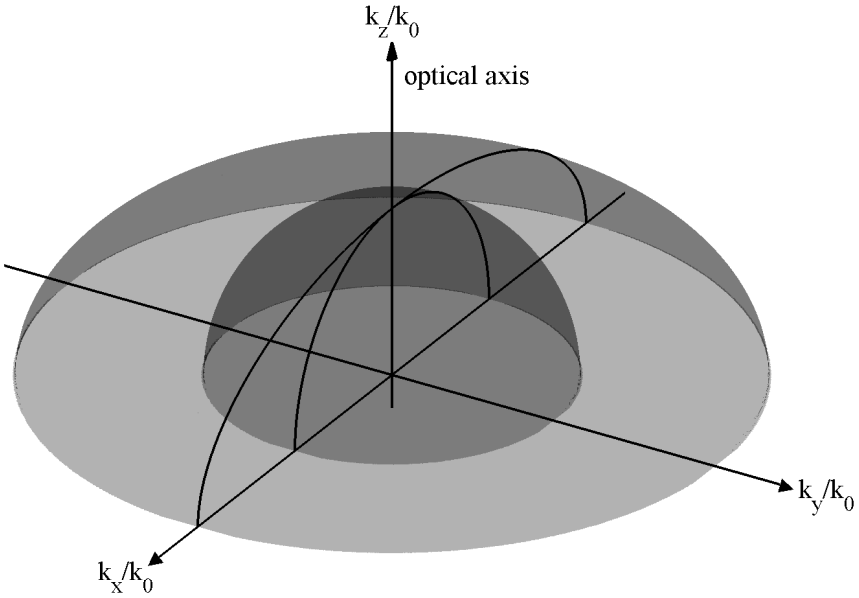

Figure A.3: Positive shells of Fresnel's wave surface for a *uniaxial* anisotropic crystal; they have one points in common which locate the only crystal's optical axis.

(A.4) can be factored as

$$\left[\frac{k^2}{\varepsilon_x} - k_0^2\right]\left[\frac{k_x^2 + k_y^2}{\varepsilon_z} + \frac{k_z^2}{\varepsilon_x} - k_0^2\right] = 0 \tag{A.8}$$

so that its shell are a sphere and an ellipsoid. These two sheets of normal surface touch at two points on z axis, which is the only optical axis, and the crystal is said to be *uniaxial* (***Fig.A.3***).

In a biaxial crystal, the principal axes are labeled in such a way that the three dielectric permittivities are in the following order: $\varepsilon_x < \varepsilon_y < \varepsilon_z$. With this convention the optical axes lie in the $k_x k_z$ plane (***Fig.A.1*** and ***Fig.A.2c***). In a uniaxial crystal, the directions that correspond to the two equal values of permittivity are called *ordinary* direction ($\varepsilon_x = \varepsilon_y = \varepsilon_o$), the other is called *extraordinary* ($\varepsilon_z = \varepsilon_e$). If $\varepsilon_o < \varepsilon_e$, the crystal is said to be *positive*, whereas if $\varepsilon_o > \varepsilon_e$, it is said to be *negative*.

Optical indicatrix

The electric energy density of a plane electromagnetic wave in a dielectric anisotropic crystal is $U_e = 0.5[\boldsymbol{E} \cdot \boldsymbol{D}]$ and by using the first of relations (2.5), we have

$$U_e = \frac{1}{2}\varepsilon_0 \boldsymbol{E} \cdot (\bar{\bar{\varepsilon}}_r \boldsymbol{E}) \; .$$

In the optical principal coordinate system, the electric energy density can be written as

$$U_e = \frac{1}{2}\varepsilon_0(\varepsilon_x E_x^2 + \varepsilon_y E_y^2 + \varepsilon_z E_z^2) = \frac{1}{2\varepsilon_0}\left(\frac{D_x^2}{\varepsilon_x} + \frac{D_y^2}{\varepsilon_y} + \frac{D_z^2}{\varepsilon_z}\right) \; .$$

If we replace $\boldsymbol{D}/\sqrt{2U_e}$ by $\boldsymbol{r} = [x, y, z]$ and $\varepsilon_i/\varepsilon_0$ by n_i (the refractive index of the i direction), we get the equation of an ellipsoid in canonical position (center at origin) with major axes parallel to the reference directions whose respective lengths are $2n_x$, $2n_y$ and $2n_z$

$$\frac{x^2}{n_x^2} + \frac{y^2}{n_y^2} + \frac{z^2}{n_z^2} = 1 \, .$$

The ellipsoid is known ad the *index ellipsoid* or as the *optical indicatrix*. These ellipsoid is used mainly to find the two indexes of refraction and the two corresponding direction of $\boldsymbol{D}$ associated with the two independent plane waves that can propagate along an arbitrary direction $\boldsymbol{k}/k$ in an anisotropic crystal. This is done through the following instruction: find the intersection ellipse between a plane through the origin that is normal to the direction of propagation $\boldsymbol{k}/k$ and the index ellipsoid. The two semi-axes of the intersection ellipse are parallel to the allowed polarizations of the electric displacement $\boldsymbol{D}$ and whose lengths are equal to n_1 and n_2.

If un-polarized light enters in an uniaxial crystal with $\varepsilon_x = \varepsilon_y = \varepsilon_o$ and $\varepsilon_z = \varepsilon_e$, the component with polarization perpendicular to the optical axis is the ordinary wave, it is refracted according to the standard law of refraction and its permittivity is equal to ε_o (A.7). The component with polarization parallel to the optical axis is refracted as a nonstandard angle because of the dielectric permittivity seen by this wave depends by the wave's propagation direction within the crystal $\varepsilon_e(\vartheta)$ (A.6)

$$\varepsilon_e(\vartheta) = \frac{\varepsilon_o \varepsilon_e}{\varepsilon_o \sin^2\vartheta + \varepsilon_e \cos^2\vartheta} \qquad \Rightarrow \qquad \frac{1}{\varepsilon_e(\vartheta)} = \frac{\cos^2\vartheta}{\varepsilon_o} + \frac{\sin^2\vartheta}{\varepsilon_e} \, , \tag{A.9}$$

for this reason this component is said extraordinary wave.

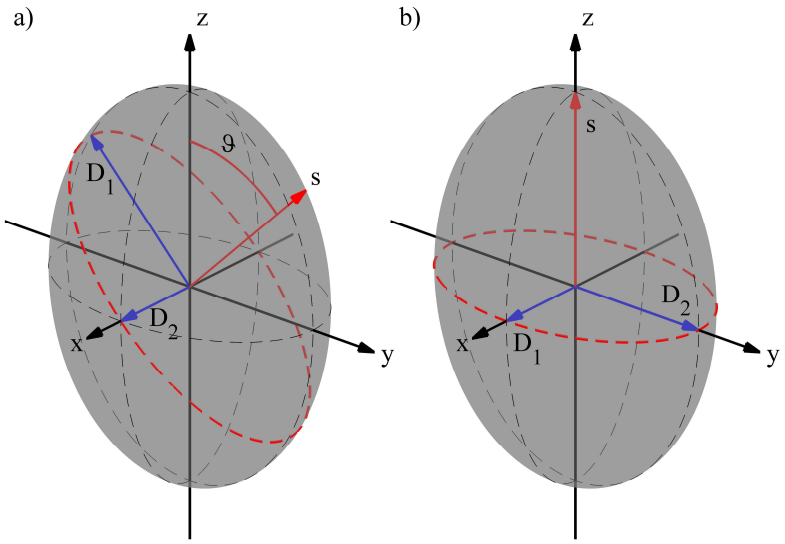

Figure A.4: Index ellipsoid or optical indicatrix. The two cases illustrated are for two different direction of propagation: $\boldsymbol{k}/k = [\cos(\pi/4), \sin(\pi/4), 0]$ (a) and $\boldsymbol{k}/k = [0, 0, 1]$ (b). The two semi-axes of the intersection ellipse (red) in the plane through the origin that is normal to the direction of propagation represent the allowed polarizations of dielectric displacement $\boldsymbol{D}$ (blue arrows) and their lengths are equal to the two indexes of refraction seen by the corresponding waves.

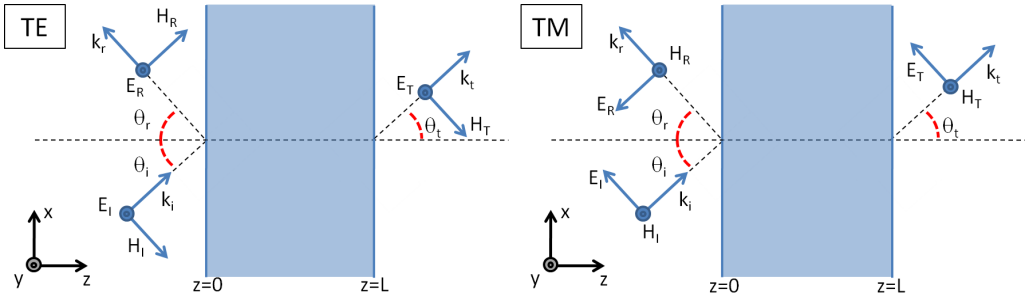

Figure A.5: Schematic illustration of plane of incidence of Transverse electric (TE, s-polarization) and transverse magnetic (TM, p-polarization) wave with incident, reflected and transmitted fields by a slab of thickness L.

TE and TM through anisotropic slab

We consider a slab of anisotropic material with principal axes coinciding with those of the reference frame. If the plane of incidence is xz plane and z is the propagation direction of a monochromatic plane wave of angular frequency ω_0, we evaluate the transmission coefficient through the slab ($z = 0$ input slab end-face, $z = L$ output slab end-face) for a transverse electric (TE) and transverse magnetic (TM) polarization (***Fig.A.5***). The transfer function (transmittance) can be derived by explicitly solving Maxwell's equations

$$\begin{cases} \dfrac{\partial E_z}{\partial y} - \dfrac{\partial E_y}{\partial z} = i\omega_0\mu_0 H_x \\ \dfrac{\partial E_x}{\partial z} - \dfrac{\partial E_z}{\partial x} = i\omega_0\mu_0 H_y \\ \dfrac{\partial E_y}{\partial x} - \dfrac{\partial E_x}{\partial y} = i\omega_0\mu_0 H_z \end{cases} \qquad \begin{cases} \dfrac{\partial H_z}{\partial y} - \dfrac{\partial H_y}{\partial z} = -i\omega\varepsilon_0\varepsilon_x E_x \\ \dfrac{\partial H_x}{\partial z} - \dfrac{\partial H_z}{\partial x} = -i\omega_0\varepsilon_0\varepsilon_y E_y \\ \dfrac{\partial H_y}{\partial x} - \dfrac{\partial H_z}{\partial y} = -i\omega_0\varepsilon_0\varepsilon_z E_z \end{cases} \tag{A.10}$$

subject to standard boundary conditions at the end-faces.

TE dispersion relation and transmission coefficient In the considered coordinate system a TE polarized plane wave is described by an electromagnetic field as

$$\text{TE}: \quad \begin{cases} \boldsymbol{E}(x,z) = E_y(x,z)\boldsymbol{e}_y \\ \boldsymbol{H}(x,z) = H_x(x,z)\boldsymbol{e}_x + H_z(x,z)\boldsymbol{e}_z \end{cases}$$

and the (A.10) became

$$\frac{\partial E_y}{\partial z} = -i\omega_0\mu_0 H_x\,, \qquad \frac{\partial E_y}{\partial x} = i\omega_0\mu_0 H_z\,, \qquad \frac{\partial H_x}{\partial z} - \frac{\partial H_z}{\partial x} = -i\omega_0\varepsilon_0\varepsilon_y E_y\,,$$
$$\frac{\partial^2 E_y}{\partial z^2} = -i\omega_0\mu_0\frac{\partial H_x}{\partial z}\,, \qquad \frac{\partial^2 E_y}{\partial x^2} = i\omega_0\mu_0\frac{\partial H_z}{\partial x}\,, \qquad \frac{\partial^2 E_y}{\partial z^2} + \frac{\partial^2 E_y}{\partial x^2} = -k_0^2\varepsilon_y E_y\,.$$

Setting for the fields

$$\begin{cases} H_x(x,z) = (\omega_0\varepsilon_0/k_0)e^{ik_0 x\sin\vartheta_i}A_x(z) \\ E_y(x,z) = e^{ik_0 x\sin\vartheta_i}A_y(z) \\ H_z(x,z) = (\omega_0\varepsilon_0/k_0)e^{ik_0 x\sin\vartheta_i}A_z(z) \end{cases}$$

and substituting this expressions in the above equations, we get

$$\frac{d^2A_y}{dz^2} = -ik_0\frac{dA_x}{dz}\,, \quad \sin\vartheta_i A_y = A_z\,, \quad \frac{d^2A_y}{dz^2} - k_0^2\sin^2\vartheta_i A_y = -k_0^2\varepsilon_y A_y\,,$$
$$\frac{d^2A_y}{dz^2} + k_0^2\left(\varepsilon_y - \sin^2\vartheta_i\right)A_y = 0\,.$$

From the last equation we get the dispersion relation for a TE wave in an anisotropic medium

$$\kappa^2 + k_0^2\left(\varepsilon_y - \sin^2\vartheta_i\right) = 0 \quad \Rightarrow \quad \kappa = \pm ik_z = \pm i\sqrt{k_0^2\left(\varepsilon_y - \sin^2\vartheta_i\right)}$$

and the fields' amplitudes become

$$\begin{cases} A_x(z) = -\dfrac{k_z}{k_0}\left[Q_+e^{ik_z z} - Q_-e^{-ik_z z}\right] \\ A_y(z) = Q_+e^{ik_z z} + Q_-e^{-ik_z z} \\ A_z(z) = \sin\vartheta_i\left[Q_+e^{ik_z z} + Q_-e^{-ik_z z}\right] \end{cases}$$

The fields outside and within the slab are (***Fig.A.5***)

$$z<0 \quad \begin{cases} \boldsymbol{E}(x,z) = E_I\boldsymbol{e}_y e^{ik_0(x\sin\vartheta_i + z\cos\vartheta_i)} + E_R\boldsymbol{e}_y e^{ik_0(x\sin\vartheta_i - z\cos\vartheta_i)} \\ \boldsymbol{H}(x,z) = \dfrac{k_0}{\omega_0\mu_0}E_I(-\cos\vartheta_i\boldsymbol{e}_x + \sin\vartheta_i\boldsymbol{e}_z)e^{ik_0(x\sin\vartheta_i + z\cos\vartheta_i)} + \\ \qquad + \dfrac{k_0}{\omega_0\mu_0}E_R(\cos\vartheta_i\boldsymbol{e}_x + \sin\vartheta_i\boldsymbol{e}_z)e^{ik_0(x\sin\vartheta_i - z\cos\vartheta_i)} \end{cases}$$

$$0<z<L \quad \begin{cases} \boldsymbol{E}(x,z) = \left(Q_+e^{ik_z z} + Q_-e^{-ik_z z}\right)\boldsymbol{e}_y e^{ik_0 x\sin\vartheta_i} \\ \boldsymbol{H}(x,z) = -\dfrac{k_z}{\omega_0\mu_0}\left(Q_+e^{ik_z z} - Q_-e^{-ik_z z}\right)\boldsymbol{e}_x e^{ik_0 x\sin\vartheta_i} + \\ \qquad + \dfrac{k_0\sin\vartheta_i}{\omega_0\mu_0}\left(Q_+e^{ik_z z} + Q_-e^{-ik_z z}\right)\boldsymbol{e}_z e^{ik_0 x\sin\vartheta_i} \end{cases}$$

$$z > 0 \quad \begin{cases} \boldsymbol{E}(x,z) = E_T \boldsymbol{e}_y e^{ik_0(x\sin\vartheta_i + z\cos\vartheta_i)} \\ \boldsymbol{H}(x,z) = \dfrac{k_0}{\omega_0\mu_0} E_T(-\cos\vartheta_i \boldsymbol{e}_x + \sin\vartheta_i \boldsymbol{e}_z) e^{ik_0(x\sin\vartheta_i + z\cos\vartheta_i)} \end{cases}$$

and subjecting the fields to the standard boundary conditions at the end-faces (continuity of the tangential components)

$$\begin{cases} \boldsymbol{E}(x,0^-)\cdot\boldsymbol{e}_y = \boldsymbol{E}(x,0^+)\cdot\boldsymbol{e}_y \\ \boldsymbol{H}(x,0^-)\cdot\boldsymbol{e}_x = \boldsymbol{H}(x,0^+)\cdot\boldsymbol{e}_x \\ \boldsymbol{E}(x,L^-)\cdot\boldsymbol{e}_y = \boldsymbol{E}(x,L^+)\cdot\boldsymbol{e}_y \\ \boldsymbol{H}(x,L^-)\cdot\boldsymbol{e}_x = \boldsymbol{H}(x,L^+)\cdot\boldsymbol{e}_x \end{cases}$$

we get

$$\begin{cases} E_I + E_R = Q_+ + Q_- \\ k_0\cos\vartheta_i(E_I - E_R) = k_z(Q_+ - Q_-) \\ Q_+ e^{ik_zL} + Q_- e^{-ik_zL} = E_T e^{ik_zL\cos\vartheta_i} \\ k_z\left(Q_+ e^{ik_zL} - Q_- e^{-ik_zL}\right) = k_0\cos\vartheta_i E_T e^{ik_0L\cos\vartheta_i} \end{cases}$$

and the relations between the complex amplitudes of incident field E_I, reflected field E_R and transmitted field E_T are

$$\begin{cases} \dfrac{E_R}{E_I} = \dfrac{i\dfrac{1}{2}\left(N_{TE} - \dfrac{1}{N_{TE}}\right)\sin(k_zL)}{\cos(k_zL) - i\dfrac{1}{2}\left(N_{TE} + \dfrac{1}{N_{TE}}\right)\sin(k_zL)} \\ \dfrac{E_T}{E_I} = \dfrac{1}{\cos(k_zL) - i\dfrac{1}{2}\left(N_{TE} + \dfrac{1}{N_{TE}}\right)\sin(k_zL)} e^{-ik_0L\cos\vartheta_i} \end{cases}$$

where $N_{TE} = k_0\cos\vartheta_i/k_z$. Therefore the reflectance R and transmittance T functions are

$$\begin{cases} R = \dfrac{\left|\dfrac{1}{2}\left(N_{TE} - \dfrac{1}{N_{TE}}\right)\sin(k_zL)\right|^2}{\left|\cos(k_zL) - i\dfrac{1}{2}\left(N_{TE} + \dfrac{1}{N_{TE}}\right)\sin(k_zL)\right|^2} \\ T = \dfrac{1}{\left|\cos(k_zL) - i\dfrac{1}{2}\left(N_{TE} + \dfrac{1}{N_{TE}}\right)\sin(k_zL)\right|^2} \end{cases} \tag{A.11}$$

TM dispersion relation and transmission coefficient In the considered coordinate system a TM polarized plane wave is described by an electromagnetic field as

$$\text{TM}: \quad \begin{cases} \boldsymbol{E}(x,z) = E_x(x,z)\boldsymbol{e}_x + E_z(x,z)\boldsymbol{e}_z \\ \boldsymbol{H}(x,z) = H_y(x,z)\boldsymbol{e}_y \end{cases}$$

and the (A.10) become

$$\frac{\partial H_y}{\partial z} = i\omega_0\varepsilon_0\varepsilon_x E_x\,, \quad \frac{\partial H_y}{\partial x} = -i\omega_0\varepsilon_0\varepsilon_z E_z\,, \quad \frac{\partial E_x}{\partial z} - \frac{\partial E_z}{\partial x} = i\omega_0\mu_0 H_y\,,$$
$$\frac{\partial^2 H_y}{\partial z^2} = i\omega_0\varepsilon_0\varepsilon_x\frac{\partial E_x}{\partial z}\,, \quad \frac{\partial^2 H_y}{\partial x^2} = -i\omega_0\varepsilon_0\varepsilon_z\frac{\partial E_z}{\partial x}\,, \quad \frac{1}{\varepsilon_x}\frac{\partial^2 H_y}{\partial z^2} + \frac{1}{\varepsilon_z}\frac{\partial^2 H_y}{\partial x^2} = -k_0^2 H_y\,,$$

Setting for the fields

$$\begin{cases} E_x(x,z) = e^{ik_0 x\sin\vartheta_i}A_x(z) \\ H_y(x,z) = (\omega_0\varepsilon_0/k_0)e^{ik_0 x\sin\vartheta_i}A_y(z) \\ E_z(x,z) = e^{ik_0 x\sin\vartheta_i}A_z(z) \end{cases}$$

and substituting this expressions in the above equations, we get

$$\frac{d^2A_y}{dz^2} = ik_0\varepsilon_x\frac{dA_x}{dz}\,, \quad \varepsilon_z A_z + \sin\vartheta_i A_y = 0\,, \quad \frac{1}{\varepsilon_x}\frac{d^2A_y}{dz^2} - \frac{1}{\varepsilon_z}k_0^2\sin^2\vartheta_i A_y = -k_0^2 A_y\,,$$
$$\frac{d^2A_y}{dz^2} + \varepsilon_x k_0^2\left(1 - \frac{\sin^2\vartheta_i}{\varepsilon_z}\right)A_y = 0\,.$$

From the last equation we get the dispersion relation for a TM wave in an anisotropic medium

$$\kappa^2 + \varepsilon_x k_0^2\left(1 - \frac{\sin^2\vartheta_i}{\varepsilon_z}\right) = 0 \quad \Rightarrow \quad \kappa = \pm ik_z = \pm i\sqrt{\varepsilon_x k_0^2\left(1 - \frac{\sin^2\vartheta_i}{\varepsilon_z}\right)} \tag{A.12}$$

and the fields' amplitudes become

$$\begin{cases} A_x(z) = \dfrac{k_z}{\varepsilon_x k_0}\left[Q_+ e^{ik_z z} - Q_- e^{-ik_z z}\right] \\ A_y(z) = Q_+ e^{ik_z z} + Q_- e^{-ik_z z} \\ A_z(z) = -\dfrac{\sin\vartheta_i}{\varepsilon_z}\left[Q_+ e^{ik_z z} + Q_- e^{-ik_z z}\right] \end{cases}$$

The fields outside and within the slab are (***Fig.A.5***)

$$
z<0 \quad \begin{cases} \boldsymbol{E}(x,z) = E_I(\cos\vartheta_i \boldsymbol{e}_x - \sin\vartheta_i \boldsymbol{e}_z)e^{ik_0(x\sin\vartheta_i + z\cos\vartheta_i)} + \\ \qquad\qquad + E_R(-\cos\vartheta_i \boldsymbol{e}_x - \sin\vartheta_i \boldsymbol{e}_z)e^{ik_0(x\sin\vartheta_i - z\cos\vartheta_i)} \\ \boldsymbol{H}(x,z) = \dfrac{k_0}{\omega_0\mu_0} E_I \boldsymbol{e}_y e^{ik_0(x\sin\vartheta_i + z\cos\vartheta_i)} + \\ \qquad\qquad + \dfrac{k_0}{\omega_0\mu_0} E_R \boldsymbol{e}_y e^{ik_0(x\sin\vartheta_i - z\cos\vartheta_i)} \end{cases}
$$

$$
0<z<L \quad \begin{cases} \boldsymbol{E}(x,z) = \dfrac{k_z}{\varepsilon_x k_0}\left(Q_+ e^{ik_z z} - Q_- e^{-ik_z z}\right)\boldsymbol{e}_x e^{ik_0 x\sin\vartheta_i} + \\ \qquad\qquad - \dfrac{\sin\vartheta_i}{\varepsilon_z}\left(Q_+ e^{ik_z z} + Q_- e^{-ik_z z}\right)\boldsymbol{e}_z e^{ik_0 x\sin\vartheta_i} \\ \boldsymbol{H}(x,z) = \dfrac{\omega_0\varepsilon_0}{k_0}\left(Q_+ e^{ik_z z} + Q_- e^{-ik_z z}\right)\boldsymbol{e}_y e^{ik_0 x\sin\vartheta_i} \end{cases}
$$

$$
z>0 \quad \begin{cases} \boldsymbol{E}(x,z) = E_T(\cos\vartheta_i \boldsymbol{e}_x - \sin\vartheta_i \boldsymbol{e}_z)e^{ik_0(x\sin\vartheta_i + z\cos\vartheta_i)} \\ \boldsymbol{H}(x,z) = \dfrac{k_0}{\omega_0\mu_0} E_T \boldsymbol{e}_y e^{ik_0(x\sin\vartheta_i + z\cos\vartheta_i)} \end{cases}
$$

and subjecting the fields to the standard boundary conditions at the ens-faces (continuity of the tangential components)

$$
\begin{cases} \boldsymbol{E}(x,0^-)\cdot\boldsymbol{e}_x = \boldsymbol{E}(x,0^+)\cdot\boldsymbol{e}_x \\ \boldsymbol{H}(x,0^-)\cdot\boldsymbol{e}_y = \boldsymbol{H}(x,0^+)\cdot\boldsymbol{e}_y \\ \boldsymbol{E}(x,L^-)\cdot\boldsymbol{e}_x = \boldsymbol{E}(x,L^+)\cdot\boldsymbol{e}_x \\ \boldsymbol{H}(x,L^-)\cdot\boldsymbol{e}_y = \boldsymbol{H}(x,L^+)\cdot\boldsymbol{e}_y \end{cases}
$$

we get

$$
\begin{cases} (E_I - E_R)\cos\vartheta_i = \dfrac{k_z}{\varepsilon_x k_0}(Q_+ - Q_-) \\ E_I + E_R = Q_+ + Q_- \\ \dfrac{k_z}{\varepsilon_x k_0}\left(Q_+ e^{ik_z L} - Q_- e^{-ik_z L}\right) = E_T\cos\vartheta_i e^{ik_0 L\cos\vartheta_i} \\ Q_+ e^{ik_z L} + Q_- e^{-ik_z L} = E_T e^{ik_0 L\cos\vartheta_i} \end{cases}
$$

and the relations between the complex amplitudes of incident field E_I, reflected field E_R and transmitted field E_T are

$$\begin{cases} \dfrac{E_R}{E_I} = \dfrac{-i\dfrac{1}{2}\left(N_{TM} - \dfrac{1}{N_{TM}}\right)\sin(k_z L)}{\cos(k_z L) - i\dfrac{1}{2}\left(N_{TM} + \dfrac{1}{N_{TM}}\right)\sin(k_z L)} \\ \dfrac{E_T}{E_I} = \dfrac{1}{\cos(k_z L) - i\dfrac{1}{2}\left(N_{TM} + \dfrac{1}{N_{TM}}\right)\sin(k_z L)} e^{-ik_0 L\cos\vartheta_i} \end{cases}$$

where $N_{TM} = \varepsilon_x k_0 \cos\vartheta_i / k_z$. Therefore the reflectance R and transmittance T functions are

$$\begin{cases} R = \dfrac{\left|\dfrac{1}{2}\left(N_{TM} - \dfrac{1}{N_{TM}}\right)\sin(k_z L)\right|^2}{\left|\cos(k_z L) - i\dfrac{1}{2}\left(N_{TM} + \dfrac{1}{N_{TM}}\right)\sin(k_z L)\right|^2} \\ T = \dfrac{1}{\left|\cos(k_z L) - i\dfrac{1}{2}\left(N_{TM} + \dfrac{1}{N_{TM}}\right)\sin(k_z L)\right|^2} \end{cases} \tag{A.13}$$

The (A.13) reduce (A.11) for a normal incidence. Actually, when the incident angle $\vartheta_i = 0$ for the TE waves $k_z = k_0\sqrt{\varepsilon_y}$ and $N_{TE} = 1/\sqrt{\varepsilon_y}$, for the TM waves (after a clockwise rotation about $\pi/2$ of reference frame around z axis, since the x and y direction play the same role to face the problem of slab transmittance) $k_z = k_0\sqrt{\varepsilon_y}$ and $N_{TM} = \sqrt{\varepsilon_y}$, therefore $N_{TE} + 1/N_{TE} = N_{TM} + 1/N_{TM}$.

B

Phase-matched second harmonic generation

Nonlinear metamaterials have potentially interesting applications in highly efficient nonlinear processes, owing to their ability to combine enhanced nonlinearities with exotic and configurable linear properties. Considering the electric nonlinear optical phenomena, they are nonlinear in the sense that they occur when the response of a material system $\boldsymbol{P}$ to an applied optical field $\boldsymbol{E}$ depends in a nonlinear manner on the strength of the optical field. For non spatial dishomogeneous and non temporal dispersive materials, the electric polarization's i-th component can be expressed in a Taylor series expansion

$$P_i = \varepsilon_0 \left[\chi_{ij} E_j + \chi^{(2)}_{ijk} E_j E_k + \chi^{(3)}_{ijkl} E_j E_k E_l + ... \right] ,$$

where χ_{ij} is the linear susceptibility ($[1 + \chi_{ij}] = \varepsilon^{(1)}_{ij}$), while $\chi^{(2)}_{ijk} = 2d_{ijk}$ and $\chi^{(3)}_{ijkl}$ are the second-order and third-order nonlinear optical susceptibility, respectively. The second-order nonlinearity $P^{NL}_i = 2d_{ijk} E_j E_k$ is responsible for second-harmonic generation (SHG or frequency doubling) [111].

Consider Maxwell's equations (2.1) and (2.2) and the constitutive relations (2.3) in an homogeneous dielectric non-magnetic medium in absence of sources. Exploiting the identity $\boldsymbol{\nabla} \times [\boldsymbol{\nabla} \times \boldsymbol{E}] = \boldsymbol{\nabla}[\boldsymbol{\nabla} \cdot \boldsymbol{E}] - \nabla^2 \boldsymbol{E}$ and the media homogeneity we have

$$\nabla^2 \boldsymbol{E} - \frac{\varepsilon^{(1)}_r}{c^2} \frac{\partial^2 \boldsymbol{E}}{\partial t^2} = \mu_0 \frac{\partial^2 \boldsymbol{P}^{(NL)}}{\partial t^2} .$$

We limit our considerations to two plane waves propagating along z direction at

frequency ω_1 and ω_2

$$E_i(z,t) = E_i^{(\omega_1)}(z,t) + E_i^{(\omega_2)}(z,t)\,,$$
$$E_i^{(\omega_1)}(z,t) = \frac{1}{2}\left[E_i^{(1)}(z)e^{-i(\omega_1 t - k_1 z)} + E_i^{(1)*}(z)e^{i(\omega_1 t - k_1 z)}\right],$$
$$E_i^{(\omega_2)}(z,t) = \frac{1}{2}\left[E_i^{(2)}(z)e^{-i(\omega_2 t - k_2 z)} + E_i^{(2)*}(z)e^{i(\omega_2 t - k_2 z)}\right],$$

where i labels cartesian coordinates ($i = x, y$).

$$\nabla^2 E_i^{(\omega_1)}(z,t) = \frac{1}{2}\left[\frac{\partial^2}{\partial z^2}E_i^{(1)}(z) - 2ik_1\frac{\partial}{\partial z}E_i^{(1)}(z) - k_1^2 E_i^{(1)}(z)\right]e^{-i(\omega_1 t - k_1 z)} + \text{c.c.}$$

Assuming that the variation of complex field amplitude with z is small enough so that

$$\frac{\partial^2}{\partial z^2}E_i^{(1)} \ll k_1\frac{\partial}{\partial z}E_i^{(1)}\,,$$
$$\nabla^2 E_i^{(\omega_1)}(z,t) = -\frac{1}{2}\left[2ik_1\frac{\partial}{\partial z}E_i^{(1)}(z) + k_1^2 E_i^{(1)}(z)\right]e^{-i(\omega_1 t - k_1 z)} + \text{c.c.}$$

For the time derivatives we have

$$\frac{\partial^2}{\partial t^2}E_i^{(\omega_1)}(z,t) = -\omega_1^2 E_i^{(\omega_1)}(z,t)\,,$$

so that

$$\nabla^2 E_i^{(\omega_1)}(z,t) - \frac{1}{c^2}\frac{\partial^2}{\partial t^2}\left[\varepsilon_r^{(1)}\right]_{ij}E_j^{(\omega_1)}(z,t) =$$
$$= -\frac{1}{2}\left[2ik_1\frac{\partial}{\partial z}E_i^{(1)}(z) + k_1^2 E_i^{(1)}(z) - \frac{\omega_1^2}{c^2}\left[\varepsilon_r^{(1)}\right]_{ij}E_j^{(1)}(z)\right]e^{-i(\omega_1 t - k_1 z)} + \text{c.c.} =$$
$$= \mu_0\frac{\partial^2 \boldsymbol{P}^{(NL)}}{\partial t^2}\,.$$

Limiting the Taylor series expansion of electric polarization up to the second-order in electric field, we have for the nonlinear polarization

$$P_i^{(NL)}(z,t) = 2\varepsilon_0 d_{ijk}E_j(z,t)E_k(z,t) =$$
$$= \frac{1}{2}\varepsilon_0 d_{ijk}\left[E_j^{(1)*}E_k^{(1)} + E_j^{(2)*}E_k^{(2)} + E_j^{(1)}E_k^{(1)}e^{-2i(\omega_1 t - k_1 z)} + E_j^{(2)}E_k^{(2)}e^{-2i(\omega_2 t - k_2 z)} + \right.$$
$$+ (E_j^{(2)}E_k^{(1)} + E_j^{(1)}E_k^{(2)})e^{-i[(\omega_1+\omega_2)t - (k_1+k_2)z]} +$$
$$\left. + (E_j^{(1)*}E_k^{(2)} + E_j^{(2)}E_k^{(1)*})e^{i[(\omega_1-\omega_2)t - (k_1-k_2)z]} + \text{c.c.}\right].$$

If $\omega_2 = 2\omega_1$ and considering only the fundamental and the double frequency

$$P_i^{(NL)}(z,t) = \frac{1}{2}\varepsilon_0 d_{ijk}\left[E_j^{(1)}E_k^{(1)}\right]e^{-2i(\omega_1 t - k_1 z)} + \\ + \frac{1}{2}\varepsilon_0 d_{ijk}\left[E_j^{(1)*}E_k^{(2)} + E_j^{(2)}E_k^{(1)*}\right]e^{-i[\omega_1 t + (k_1 - k_2)z]} + \text{c.c.}$$

the equations which must be satisfied separately by each frequency component are

$$\begin{cases} 2ik_1\dfrac{\partial}{\partial z}E_i^{(1)}(z) + k_1^2 E_i^{(1)}(z) - \dfrac{\omega_1^2}{c^2}\left[\varepsilon_r^{(1)}\right]_{ij}E_j^{(1)}(z) = \\ \qquad = \omega_1^2\varepsilon_0\mu_0 d_{ijk}\left[E_j^{(1)*}E_k^{(2)} + E_j^{(2)}E_k^{(1)*}\right]e^{-i(2k_1 - k_2)z} \\ 2ik_2\dfrac{\partial}{\partial z}E_i^{(2)}(z) + k_2^2 E_i^{(2)}(z) - \dfrac{\omega_2^2}{c^2}\left[\varepsilon_r^{(1)}\right]_{ij}E_j^{(2)}(z) = \\ \qquad = 4\omega_1^2\varepsilon_0\mu_0 d_{ijk}\left[E_j^{(1)}E_k^{(1)}\right]e^{-i(k_2 - 2k_1)z} \end{cases}$$

In the optical principal coordinate system the linear dielectric tensor is diagonal, so that

$$\begin{cases} \dfrac{\partial E_i^{(1)}(z)}{\partial z} = -\dfrac{i}{2}\dfrac{\omega_1}{c\sqrt{\varepsilon_r^{(1)}(\omega_1)}}d_{ijk}\left[E_j^{(1)*}E_k^{(2)} + E_j^{(2)}E_k^{(1)*}\right]e^{-i(2k_1 - k_2)z} \\ \dfrac{\partial E_i^{(2)}(z)}{\partial z} = -i\dfrac{\omega_1}{c\sqrt{\varepsilon_r^{(1)}(2\omega_1)}}d_{ijk}\left[E_j^{(1)}E_k^{(1)}\right]e^{-i(k_2 - 2k_1)z} \end{cases}$$

where we exploit the relation $k = \omega\sqrt{\varepsilon_r}/c$. The solution of the $E_i^{(2)}$'s equation for a nonlinear crystal of length L with no second-harmonic input ($E_i^{(2)}(0) = 0$) is

$$E_i^{(2)}(z) = \frac{\omega_1}{c\sqrt{\varepsilon_r^{(1)}(2\omega_1)}}d_{ijk}\left[E_j^{(1)}E_k^{(1)}\right]\frac{e^{-i(k_2 - 2k_1)z} - 1}{(k_2 - 2k_1)}$$

and at the end of the crystal

$$E_i^{(2)}(L) = \frac{\omega_1}{c\sqrt{\varepsilon_r^{(1)}(2\omega_1)}}d_{ijk}\left[E_j^{(1)}E_k^{(1)}\right]\frac{e^{-i(k_2 - 2k_1)L} - 1}{(k_2 - 2k_1)}\,.$$

An expression for the second-harmonic output power $P_i^{(\omega_2)}$

$$\frac{P_i^{(\omega_2)}}{\text{area}} = \frac{1}{2}\sqrt{\frac{\varepsilon_0\varepsilon_r^{(1)}(2\omega_1)}{\mu_0}}E_i^{(2)}(L)E_i^{(2)*}(L)\,,$$

$$\frac{P_i^{(\omega_2)}}{\text{area}} = \frac{2\pi^2}{\varepsilon_r^{(1)}(\omega_1)}\sqrt{\frac{\varepsilon_0}{\mu_0\varepsilon_r^{(1)}(2\omega_1)}}\left|d_{ijk}E_j^{(1)}E_k^{(1)}\right|^2\left(\frac{L}{\lambda_0}\right)^2\frac{\sin^2[(k_2 - 2k_1)L]}{[(k_2 - 2k_1)L/2]^2}\,,$$

with λ_0 is the free-space wavelength.

If $\Delta k \neq 0$ it means that the second-harmonic wave generated at some plane z is not in phase with the second-harmonic wave generated at another plane $z + \Delta z$ and this result is described by the interference factor $[\sin(\Delta kL/2)/(\Delta kL/2)]^2$. The requirement for efficient second-harmonic generation is that

$$\Delta k = k_2 - 2k_1 = k^{(2\omega_1)} - 2k^{(\omega_1)} = 0\,, \tag{B.1}$$

that is the *phase matching* condition. Under standard circumstances this condition can not to be satisfied because the index of refraction is a function of frequency and $n(2\omega_1) \neq n(\omega_1)$. The technique that is used to satisfy the phase matching requirement, that is the dielectric permittivity at the fundamental and second-harmonic frequencies must be equal, exploits the natural birefringence of anisotropic crystal. In normally dispersive anisotropic material, the dielectric permittivities seen by ordinary and extraordinary waves propagating along given directions increases with frequency and the phase matching condition is impossible to satisfy if the fundamental and second-harmonic wave are of the same type (both ordinary or extraordinary). But using two waves of different type and, for example, an uniaxial crystal, exists an ϑ_{pm} angle that (***Fig.B.1***) $\varepsilon_e^{(2\omega_1)}(\vartheta_{pm}) = \varepsilon_o^{(\omega_1)}$ (A.9)

$$\sin^2\vartheta_{pm} = \frac{\varepsilon_e^{(2\omega_1)}\left(\varepsilon_o^{(2\omega_1)} - \varepsilon_o^{(\omega_1)}\right)}{\varepsilon_o^{(\omega_1)}\left(\varepsilon_o^{(2\omega_1)} - \varepsilon_e^{(2\omega_1)}\right)}\,.$$

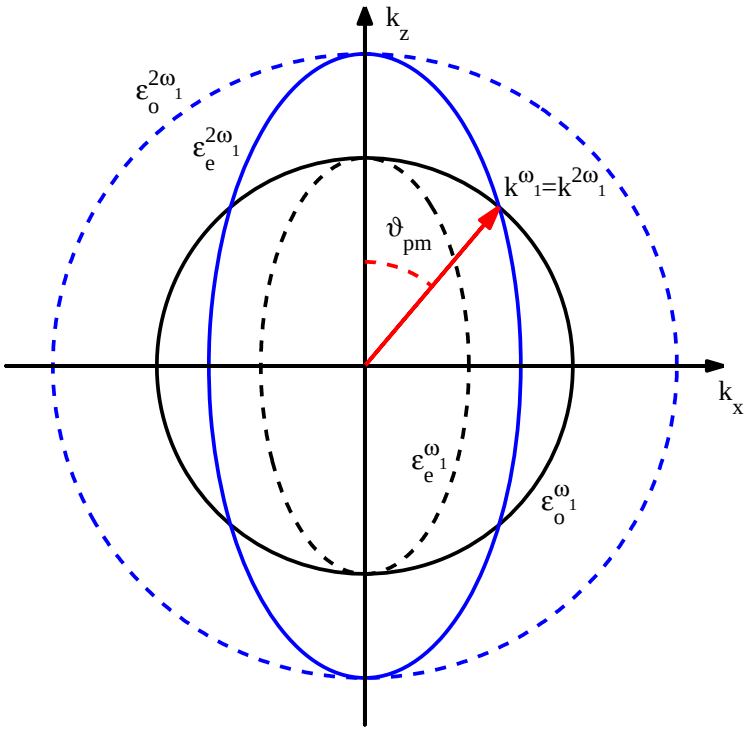

Figure B.1: Intersections of the Fresnel's wave surface with $k_x k_z$ plane of an uniaxial crystal for the ordinary and extraordinary waves at fundamental (black curves) and second-harmonic (blue curves) frequency. In the figure it is evident the propagation direction within the anisotropic media corresponding to the phase matching condition.

Bibliography

[1] W. Cai and V. Shalaev, *Optical Metamaterials - Fundamentals and Applications*, First Edition, Springer, (2010)

[2] D. R. Smith, Willie J. Padilla, D. C. Vier, S. C. Nemat-Nasser and S. Schultz: "Composite Medium with Simultaneously Negative Permeability and Permittivity", *Physical Review Letters*, **84**, 4184, (2000)

[3] V. G. Veselago: "Electrodynamics of substances with simultaneously negative values of ε and μ", *Soviet Physics Uspekhi* **10**, 509, (1968)

[4] R. A. Shelby, D. R. Smith and S. Schultz: "Experimental verification of a negative index of refraction", *Science* **292**, 77, (2001)

[5] J. B. Pendry: "Negative refraction makes a perfect lens", *Physical Review Letters* **85**, 3966, (2000)

[6] X. Ni, S. Ishii, M. D. Thoreson, V. M. Shalaev, S. Han, S. Lee and A. V. Kildishev: "Loss-compensated and active hyperbolic metamaterials", **Optics Express 19**, 25243 (2011)

[7] J. Schilling: "Uniaxial metallo-dielectric metamaterials with scalar positive permeability", *Physical Review E* **74**, 046618 (2006)

[8] R. Wangberg, J. Elser, E. E. Narimanov and V. A. Podolskiy: "Nonmagnetic nanocomposites for optical and infrared negative-refractive-index media", *Journal of the Optical Society of America B* **23**, 498 (2006)

[9] A. Ciattoni, C. Rizza and E. Palange: "Extreme nonlinear electrodynamics in metamaterials with very small linear dielectric permittivity", *Physical Review A* **81**, 043839, (2010)

[10] Y. J. Huang, W. T. Lu and S. Sridhar: "Nanowire waveguide made from extremely anisotropic metamaterials", *Physical Review A* **77**, 063836 (2008)

[11] Z. Jacob, L. V. Alekseyev and E. Narimanov: "Optical Hyperlens: Far-field imaging beyond the diffraction limit", *Optic Express* **14**, 8247 (2006)

[12] A. Fang, T. Koschny and C. M. Soukoulis: "Optical anisotropic metamaterials: Negative refraction and focusing", *Physical Review B* **79**, 245127 (2009)

[13] Y. Liu, G. Bartal, X. Zhang: "All-angle negative refraction and imaging in a bulk medium made of metallic nanowires in the visible region", *Optic Express* **16**, 15439 (2008)

[14] J. Elser, R. Wangberg, V. A. Podolskiy and E. E. Narimanov: "Nanowire metamaterials with extreme optical anisotropy", *Applied Physics Letters* **89**, 261102 (2006)

[15] Y. Zeng, Q. Wu and D. H. Werner: "Electrostatic theory for designing lossless negative permittivity metamaterials", *Optics Letters* **35**, 1431 (2010)

[16] A. Sihvola: "Mixing Rules with Complex Dielectric Coefficients", *Subsurface Sensing Technologies and Applications* **1**, 393 (2000)

[17] C. A. Foss, G. L. Hornyak, J. A. Stockert and C. R. Martin: "Template synthesized nanoscopic gold particles: optical spectra and the effects of particle size and shape", *Journal of Physical Chemistry* **98**, 2963 (1994)

[18] D. Felbacq, G. Bouchitté, B. Guizal and A. Moreau: "Two-scale approach to the homogenization of membrane photonic crystals", *Journal of Nanophotonics* **2**, 023501, (2008)

[19] A. Yariv, *Optical Waves in Crystals - Propagation and Control of Laser Radiation*, First Edition, Wiley, (1984)

[20] M. Born and E. Wolf, *Principles of Optics*, Sixth Edition, Cambridge University Press, (1980)

[21] B. Wood, J. B. Pendry and D. P. Tsai: "Directed subwavelength imaging using a layered metal-dielectric system", *Physical Review B* **74**, 115116, (2006)

[22] J. C. Maxwell-Garnett: "Colours in metal glasses and in metallic films", *Philosophical Transactions of the Royal Society London* **203**, 385 (1904)

[23] D. A. G. Bruggeman: "Berechnung verschiedener physikalischer Konstanten von heterogenen Substanzen. I. Dielektrizitätskonstanten und Leitfähigkeiten der Mischkörper aus isotropen Substanzen", *Annalen der Physik (Leipzig)* **24**, 636 (1935)

[24] J. D. Jackson: *Classsical electrodynamics*, Third Edition, John Wiley & Sons, (1999)

[25] C. F. Bohren and D. R. Huffman, *Absorption and scattering of light by small particles*, Wiley, (1983)

[26] H. Masuda and K. Fukuda: "Ordered metal nanohole arrays made by a two-step replication of honeycomb structures of anodic alumina", *Science* **268**, 1466 (1995)

[27] C. R. Martin: "Nanomaterials: a membrane-based synthetic approach", *Science* **266**, 1961 (1994)

[28] N. A. F. Al-Rawashdeh, M. L. Sandrock, C. J. Seugling and C. A. Foss: "Visible region polarization spectroscopic studies of template-synthesized gold nanoparticles oriented in polyethylene", *Journal of Physical Chemistry B* **102**, 361 (1998)

[29] M. Meier and A. Wokaun: "Enhanced fields on large metal particles: dynamic depolarization", *Optic Letters* **8**, 581 (1983)

[30] R. J. Gehr and R. W. Boyd: "Optical properties of nanostructured optical materials", *Chemical Material* **8**, 1807 (1996)

[31] G. L. Hornyak, C. J. Patrissi and C. R. Martin: "Fabrication, characterization, and optical properties of gold nanoparticle/porous alumina composites: the non-scattering Maxwell-Garnett limit", *Journal of Physical Chemistry B* **101**, 1548 (1997)

[32] E. Wäckelgard: "The experimental dielectric function of porous anodic alumina in the infrared region; a comparison with the Maxwell-Garnett model", *Journal of Physics: Condensed Matter* **8**, 4289 (1996)

[33] Y. Rao, J. Qu, T. Marinis and C. P. Wong: "A precise numerical prediction of effective dielectric constant for polymer-ceramic composite based on effective medium theory", *IEEE Transactions on Components and Packaging technologies* **23**, 680 (2000)

[34] C. G. Parazzoli, R. B. Greegor, K. Li, B. E. C. Koltenbah and M. Tanielian: "Experimental verification and simulation of negative index of refraction using Snell's law", *Physical Review Letters* **90**, 107401-1, (2003)

[35] V. M. Shalaev, W. Cai, U. K. Chettiar, H. Yuan, A. K. Sarychev, V. P. Drachev and A. V. Kildishev: "Negative index of refraction in optical metamaterials", *Optics Letters* **30**, 3356, (2005)

[36] J. B. Pendry and D. R. Smith: "Reversing light with negative refraction", *Physics Today* **57**, 37, (2004)

[37] V. A. Podolskiy and E. E. Narimanov: "Near-sighted superlens", *Optics Letters* **30**, 75 (2005)

[38] D. O. S. Melville and R. J. Blaikie: "Super-resolution imaging through a planar silver layer", *Optics Express* **13**, 2127, (2005)

[39] L. V. Alekseyev and E. Narimanov: "Slow light and 3D imaging with non-magnetic negative index systems", *Optics Express* **14**, 11184, (2006)

[40] D. R. Smith and D. Schurig: "Electromagnetic wave propagation in media with indefinite permittivity and permeability tensors", *Physical Review Letters* **90**, 077405 (2003)

[41] M. A. Noginov, Y. A. Barnakov, G. Zhu, T. Tumkur, H. Li and E. E. Narimanov: "Bulk photonic metamaterial with hyperbolic dispersion", *Applied Physics Letters* **94**, 151105 (2009)

[42] A. J. Hoffman, L. Alekseyev, S. S. Howard, K. J. Franz, D. Wasserman, V. A. Podolsky, E. E. Narimanov, D. L. Sivco and C. Gmachl: "Negative refraction in semiconductor metamaterials", *Nature Materials* **6**, 946 (2007)

[43] D. Korobkin, B. Neuner, C. Fietz, N. Jegenyes, G. Ferro and G. Shvets: "Measurements of the negative refractive index of sub-diffraction waves propagating in an indefinite permittivity medium", *Optics Express* **18**, 22734 (2010)

[44] J. Sun, J. Zhou, B. Li and F. Kang: "Indefinite permittivity and negative refraction in natural material: Graphite", *Applied Physics Letters* **98**, 101901, (2011)

[45] R. Wang, J. Sun and J. Zhoua: "Indefinite permittivity in uniaxial single crystal at infrared frequency", *Applied Physics Letters* **97**, 031912, (2010)

[46] I. V. Lindell, S. A. Tretyakov, K. I. Nikoskinen and S. Ilvonen: "BW media-media with negative parameters, capable of supporting backward waves", *Microwave and Optical Technology Letters* **31**, 129 (2001)

[47] Z. Liu, Z. Liang, X. Jiang, X. Hu, X. Li and J. Zi: "Hyper-interface, the bridge between radiative wave and evanescent wave", *Applied Physics Letters* **96**, 113507 (2010)

[48] H. Lee, Z. Liu, Y. Xiong, C. Sun and X. Zhang: "Development of optical hyperlens for imaging below the diffraction limit", *Optics Express* **15**, 15886 (2007)

[49] J. Yao, K. T. Tsai, Y. Wang, Z. Liu, G. Bartal, Y. L. Wang and X. Zhang: "Imaging visible light using anisotropic metamaterial slab lens", *Optics Express* **17**, 22380 (2009)

[50] B. D. F. Casse, W. T. Lu, Y. J. Huang, E. Gultepe, L. Menon and S. Sridhara: "Super-resolution imaging using a three-dimensional metamaterials nanolens", *Applied Physics Letters* **96**, 023114 (2010)

[51] Z. Liu, H. Lee, Y. Xiong, C. Sun, X. Zhang: "Far-field optical hyperlens magnifying sub-diffraction-limited objects", *Science* **315**, 1686 (2007)

[52] J. Yang, X. Hu, X. Li, Z. Liu, X. Jiang and J. Zi: "Cancellation of reflection and transmission at metamaterial surfaces", *Optics Letters* **35**, 16 (2010)

[53] J. Zhao, Y. Chen and Y. Feng: "Polarization beam splitting through an anisotropic metamaterial slab realized by a layered metal-dielectric structure", *Applied Physics Letters* **92**, 071114 (2008)

[54] L. V. Alekseyev, E. E. Narimanov, T. Tumkur, H. Li, Y. A. Barnakov and M. A. Noginov: "Uniaxial epsilonnear-zero metamaterial for angular filtering and polarization control", *Applied Physics Letters* **97**, 131107 (2010)

[55] M. Silveirinha and N. Engheta: "Tunneling of electromagnetic energy through subwavelength channels and bends using ε-near-zero materials", *Physical Review Letters* **97**, 157403 (2006)

[56] D. T. Emerson: "The work of Jagadis Chandra Bose: 100 years of millimeter-wave research", *Transactions on microwave theory and techniques* **45**, 2267, (1997)

[57] P. B. Johnson and R. W. Christy: "Optical constants of the noble metals", *Physical Review B* **6**, 4370, (1972)

[58] E. Palik and G. Ghosh: *Handbook of Optical Constants of Solids II*, Academic, New York, (1991)

[59] J. S. Patel and H. Yokoyama: "Continuous anchoring transition in liquid crystals", *Nature* **362**, 525, (1993)

[60] G. P. Bryan-Brown, E. L. Wood and I. C. Sage: "Weak surface anchoring of liquid crystals", *Nature* **399**, 338 (1999)

[61] S. Gauza, J. Li, S. T. Wu, A. Spadlo, R. Dabrowski, Y. N. Tzeng and K. L. Cheng: "High birefringence and high resistivity isothiocyanate-based nematic liquid crystal mixtures", *Liquid Crystals* **32**, 1077, (2005)

[62] R. Stepanyan: "Effective dielectric properties of composite materials in the surface layer", *Physical Reviwe B* **67**, 073403 (2003)

[63] A. Yariv and P. Yeh, *Optical Electronics in Modern Communication*, Sixth Edition, Oxfornd University Press, (2007)

[64] H. Z. Kang, T. H. Zhang, H. H. Ma, C. B. Lou, S. M. Liu, J. G. Tian and J. J. Xu: "$(2+1)D$ surface solitons in virtue of the cooperation of nonlocal and local nonlinearities", *Optics Letters* **35**, 1605, (2010)

[65] G. K. Samanta, S. Chaitanya Kumar, Kavita Devi and M. Ebrahim-Zadeh: "Multicrystal, continuous-wave, single-pass second-harmonic generation with 56% efficiency ", *Optics Letters* **35**, 3513, (2010)

[66] M. Yamada, N. Nada, M. Saitoh, and K. Watanabe: "Firstorder quasi-phase matched $LiNbO_3$ waveguide periodically poled by applying an external field for efficient blue second harmonic generation", *Applied Physics Letters* **62**, 435, (1993)

[67] R. M. Corn and D. A. Higgins: "Optical second harmonic generation as a probe of surface chemistry", *Chemical Review* **94**, 107, (1994)

[68] P. J. Campagnola and L. M. Loew: "Second harmonic imaging microscopy for visualizing biomolecular arrays in cells, tissues and organisms", *Nature Biotechnology* **21**, 1356, (2003)

[69] V. Pellegrini, R. Colombelli, I. Carusotto, F. Beltram, S. Rubini, R. Lantier, A. Franciosi, C. Vinegoni and L. Pavesi: "Resonant second harmonic generation in ZnSe bulk microcavity", *Applied Physics Letters* **74**, 1945, (1999)

[70] H. Cao, D. B. Hall, J. M. Torkelson and C.-Q. Cao: "Large enhancement of second harmonic generation in polymer films by microcavities", *Applied Physics Letters* **76**, 538, (2000)

[71] S. Lei, Y. Yao, Z. Li, T. Yu and Z. Zou: "Design and theoretical analysis of resonant cavity for second-harmonic generation with high efficiency", *Applied Physics Letters* **98**, 031102, (2011)

[72] J. P. Mondia, H. M. van Driel, W. Jiang, A. R. Cowan and Jeff F. Young: "Enhanced second-harmonic generation from planar photonic crystals", *Optics Letters* **28**, 2500, (2003)

[73] M. Liscidini, A. Locatelli, L. C. Andreani and C. De Angelis: "Maximum-exponent scaling behavior of optical second-harmonic generation in finite multilayer photonic crystals ", *Physical Review Letters* **99**, 053907, (2007)

[74] M. Siltanen, S. Leivo, P. Voima, M. Kauranen, P. Karvinen, P. Vahimaa and M. Kuittinen: "Strong enhancement of second-harmonic generation in all-dielectric resonant waveguide grating", *Applied Physics Letters* **91**, 111109, (2007)

[75] L. Zhao, B. Gub and Y. Zhou: "A way for enhancing second harmonic generation in one-dimensional nonlinear photonic crystals ", *Optics Communication* **281**, 2954 (2008)

[76] Y. Nakayama, P. J. Pauzauskie, A. Radenovic, R. M. Onorato, R. J. Saykally, J. Liphardt and P. Yang: "Tunable nanowire nonlinear optical probe",*Nature* **447**, 1098, (2007)

[77] C. L. Hsieh, R. Grange, Y. Pu and D. Psaltis: "Three-dimensional harmonic holographic microcopy using nanoparticles as probes for cell imaging", *Optics Express* **17**, 2880, (2009)

[78] W. Fan, S. Zhang, N.-C. Panoiu, A. Abdenour, S. Krishna, R. M. Osgood Jr., K. J. Malloy and S. R. J. Brueck: "Second harmonic generation from a nanopatterned isotropic nonlinear material ", *Nano Letters* **6**, 1027, (2006)

[79] A. Lesuffleur, L. K. Kumar and R. Gordon: "Enhanced second harmonic generation from nanoscale double-hole arrays in a gold film", *Applied Physics Letters* **88**, 261104, (2006)

[80] M. Kang, Y. Li, K. Lou, S.-M. Li, Q. Bai, J. Chen and H.-T. Wang: "Second-harmonic generation in one-dimensional metal gratings with dual extraordinary transmissions", *Journal of Applied Physics* **107**, 053108, (2010)

[81] P. Schon, N. Bonod, E. Devaux, J. Wenger, H. Rigneault, T. W. Ebbesen and S. Brasselet: "Enhanced second-harmonic generation from individual metallic nanoapertures", *Optics Letters* **35**, 4063, (2010)

[82] S. J. Oldenburg, R. D. Averitt, S. L. Westcott and N. J. Halas: "Nanoengineering of optical resonances", *Chemical Phisics Letters* **288**, 243, (1998)

[83] Y. Pu, R. Grange, C.-L. Hsieh and D. Psaltis: "Nonlinear optical properties of core-shell nanocavities for enhanced second-harmonic generation", *Phisical Review Letters* **104**, 207402, (2010)

[84] R. Liu, Q. Cheng, T. Hand, J. J. Mock, T. J. Cui, S. A. Cummer and David R. Smith: "Experimental demonstration of electromagnetic tunneling through an epsilon-near-zero metamaterial at microwave frequencies", *Physical Review Letters* **100**, 023903, (2008)

[85] B. Edwards, A. Alu, M. E. Young, M. Silveirinha and N. Engheta: "Experimental verification of epsilon-near-zero metamaterial coupling and energy squeezing using a microwave waveguide", *Physical Reviwe Letters* **100**, 033903, (2008)

[86] V. C. Nguyen, L. Chen and K. Halterman: "Total transmission and total reflection by zero index metamaterials with defects", *Physical Review Letters* **105**, 233908, (2010)

[87] D. A. Powell, A. Alu, B. Edwards, A. Vakil, Y. S. Kivshar and N. Engheta: "Nonlinear control of tunneling through an epsilon-near-zero channel" *Physical Review B* **79**, 245135, (2009)

[88] A. Ciattoni, C. Rizza and E. Palange: "Transverse power flow reversing of guided waves in extreme nonlinear metamaterials", *Optics Express* **18**, 11911, (2010)

[89] A. Ciattoni, C. Rizza and E. Palange: "Transmissivity directional hysteresis of a nonlinear metamaterial slab with very small linear permittivity", *Optics Letters* **35**, 2130, (2010)

[90] A. Ciattoni, C. Rizza and E. Palange: "Multistability at arbitrary low optical intensities in a metal-dielectric layered structure", *Optics Express* **19**, 283, (2011)

[91] E. Spinozzi and A. Ciattoni: "Ultrathin optical switch based on a liquid crystal/silver nanoparticles mixture as a tunable indefinite medium", *Optical Material Express* **1**, 732, (2011)

[92] R. L. Sutherland, D. G. McLean and S. Kirkpatrick, *Handbook of Nonlinear Optics*, Second Edition, Marcel Dekker, (2003)

[93] M. A. Vincenti, D. de Ceglia, A. Ciattoni and M. Scalora: "Singularity-driven second- and third-harmonic generation at ε-near-zero crossing points", *Physical Review A* **84**, 063826, (2011)

[94] I. C. Pintre, J. L. Serrano, B. Ros, J. Martinez-Perdiguero, I. Alonso, J. Ortega, C. L. Folcia, J. Etxebarria, R. Alicantee and B. Villacampa: "Bent-core liquid crystals in a route to efficient organic nonlinear optical materials", *Jpurnal of Material Chemistry* **20**, 2965, (2010)

[95] C. Rizza, A. Di Falco and A. Ciattoni: "Gain assisted nanocomposite multilayers with near zero permittivity modulus at visible frequencies", *Applied Physics Letters* **99**, 221107, (2011)

[96] S. Campione, M. Albani and F. Capolino: "Complex modes and near-zero permittivity in 3D arrays of plasmonic nanoshells: loss compensation using gain", *Optical Material Express* **1**, 1077, (2011)

[97] A. E. Siegman: *Lasers*, First Edition, University Science Books, (1986)

[98] M. Okuda, K. Iwahori, I. Yamashita and H. Yoshimura: "Fabrication of nickel and chromium nanoparticles using the protein cage of apoferritin", *Biotechnolo and Bioengineering* **84**, 187, (2003)

[99] A. D. Rakic, A. B. Djurisic, J. M. Elazar and M. L. Majewski: "Optical properties of metallic films for vertical-cavity optoelectronic devices ", *Applied Optics* **37**, 5271, (1998)

[100] T. Teranishi and M. Miyake: "Size control of palladium nanoparticles and their crystal structures", *Chemical Material* **10**, 594, (1998)

[101] W. J. Padilla, A. J. Taylor, C. Highstrete, M. Lee and D. Averitt: "Dynamical electric and magnetic metamaterial response at terahertz frequencies", *Physical Review Letters* 96, 107401, (2006)

[102] T. Driscoll, G. O. Andreev, D. N. Basov, S. Palit, S. Y. Cho, N. M. Jokerst and D. R. Smith: "Tuned permeability in terahertz split-ring resonators for devices and sensors", *Applied Physics Letters* 91, 062511, (2007)

[103] W. L. Chan, H. Chen, A. J. Taylor, I. Brener, M. J. Cich and D. M. Mittleman: "A spatial light modulator for terahertz beams", *Applied Physics Letters* 94, 213511, (2009)

[104] N. Shen, M. Massaouti, M. Gokkavas, J. Manceau, E. Ozbay, M. Kafesaki, T. Koschny, S. Tzortzakis and C. M. Soukoulis, *Physical Review Letters* **106**, 037403, (2011)

[105] H. Chen, W. J. Padilla, J. M. O. Zide, A. C. Gossard, A. J. Taylor and R. D. Averitt: "Active terahertz metamaterial devices"**Nature** 444, 597, (2006)

[106] D. R. Smith, D. Schurig, J. J. Mock, P. Kolinko and P. Rye: "Partial focusing of radiation by a slab of indefinite media", *Applied Physics Letters* **84**, 2244, (2004)

[107] D. Schurig and D. R. Smith: "Spatial filtering using media with indefinite permittivity and permeability tensors", *Applied Physics Letters* **82**, 2215, (2003)

[108] E. Garmire and A. Kost, *Nonlinear Optics in Semiconductors I*, Academic, (1999)

[109] J. Elser, V. A. Podolskiya, I. Salakhutdinov and I. Avrutsky: "Non-local effects in effective medium response of nano-layered meta-materials", *Applied Physics Letters* **90**, 191109, (2007)

[110] A. Ciattoni and E. Spinozzi: "Efficient second-harmonic generation in micrometer-thick slabs with indefinite permittivity", *Physical Review A* **85**, 043806 (2012).

[111] P. A. Franken, A. E. Hill, C. W. Peters and G. Weinreich: "Generation of optical armonics", *Physical Review Letters* **7**, 118, (1961)